AFRL-RX-WP-TR-2010-4028

DURABLE HYBRID COATINGS
Annual Performance Report (2009)

Vsevolod Balbyshev, Bret J. Chisholm, Douglas L. Schulz, Gregory J. McCarthy, Larry R. Pederson, Dante Battocchi, Kerry Allahar, and Gordon P. Bierwagen

North Dakota State University

OCTOBER 2009
Interim Report

STINFO COPY

AIR FORCE RESEARCH LABORATORY
MATERIALS AND MANUFACTURING DIRECTORATE
WRIGHT-PATTERSON AIR FORCE BASE, OH 45433-7750
AIR FORCE MATERIEL COMMAND
UNITED STATES AIR FORCE

NOTICE AND SIGNATURE PAGE

*//Signature//

AARON VEYDT, Program Manager
Thermal Sciences and Materials Branch
Nonmetallic Materials Division

//Signature//

NADER HENDIZADEH, Chief
Thermal Sciences and Materials Branch
Nonmetallic Materials Division

//Signature//

SHASHI K. SHARMA, Deputy Chief
Nonmetallic Materials Division
Materials and Manufacturing Directorate

REPORT DOCUMENTATION PAGE

1. REPORT DATE *(DD-MM-YY)*	2. REPORT TYPE	3. DATES COVERED *(From - To)*
October 2009	Interim	01 October 2008 – 01 September 2009

4. TITLE AND SUBTITLE
DURABLE HYBRID COATINGS
Annual Performance Report (2009)

5a. CONTRACT NUMBER
FA8650-04-1-5045

5b. GRANT NUMBER

5c. PROGRAM ELEMENT NUMBER
61202F

6. AUTHOR(S)
Vsevolod Balbyshev, Bret J. Chisholm, Douglas L. Schulz, Gregory J. McCarthy, and Larry R. Pederson (Center for Nanoscale Science and Engineering)
Dante Battocchi, Kerry Allahar, and Gordon P. Bierwagen (Department of Coatings and Polymeric Materials)

5d. PROJECT NUMBER
4347

5e. TASK NUMBER
60

5f. WORK UNIT NUMBER
65100002

7. PERFORMING ORGANIZATION NAME(S) AND ADDRESS(ES)

Center for Nanoscale Science and Engineering
1805 NDSU Research Park Drive N.
North Dakota State University
Fargo, ND 58102

Department of Coatings and Polymeric Materials
1735 NDSU Research Park Drive N.
North Dakota State University
Fargo, ND 58105

8. PERFORMING ORGANIZATION REPORT NUMBER

9. SPONSORING/MONITORING AGENCY NAME(S) AND ADDRESS(ES)
Air Force Research Laboratory
Materials and Manufacturing Directorate
Wright-Patterson Air Force Base, OH 45433-7750
Air Force Materiel Command
United States Air Force

10. SPONSORING/MONITORING AGENCY ACRONYM(S)
AFRL/RXBT

11. SPONSORING/MONITORING AGENCY REPORT NUMBER(S)
AFRL-RX-WP-TR-2010-4028

12. DISTRIBUTION/AVAILABILITY STATEMENT
Approved for public release; distribution unlimited.

13. SUPPLEMENTARY NOTES
PAO Case Number: 88ABW-2010-0509; Clearance Date: 08 Feb 2010. Report contains color.

14. ABSTRACT
The overall goal of this program is to contribute to the development of the next-generation anti-corrosion and other protective coating systems for USAF aircraft. During the past year, NDSU's promising Mg-based primer was further optimized. Five different Mg alloy pigments were evaluated, and the optimal pigment volume ratio was established. Flexible binders were identified that substantially improved mechanical properties of the Mg-based primer without sacrificing corrosion properties. Research continued to implement high-throughput methods for coatings formulation and optimization, including development of a technique that enables high-throughput screening of the abrasion resistance of cured coatings. A hybrid organic-inorganic binder for Mg-based primers was developed that includes silica nanoparticles, which has been shown to provide excellent corrosion resistance to important aluminum alloys. Research continued to develop a rapid-cure Mg-rich primer system that would minimize out-of-service time when an aircraft is repainted. These "dual-cure" binder systems combine ambient-cured siloxane networks with a UV-curable cross-linked network. Progress was made in developing in-field methods to deposit transparent conducting oxide coatings on aircraft canopies by atmospheric pressure plasma methods. Such coatings are needed to dissipate static charge buildup on canopies when in service. Finally, NDSU has investigated the use of electrochemical sensors embedded between the Mg-rich primer and the topcoat, to monitor the degree of corrosion protection provided by the primer. A principal advantage of this approach is that the topcoat protects the sensor from the environment, which reduces electrochemical noise, improves measurement accuracy, and extends the sensor lifetime.

15. SUBJECT TERMS
Mg-rich primer, high-throughput (HT), plasma deposition, hybrid organic-inorganic binders, dual-cure polymerization mechanism, indium and tin oxides, inorganic coatings, embedded sensors, in situ monitoring

16. SECURITY CLASSIFICATION OF:

a. REPORT	b. ABSTRACT	c. THIS PAGE
Unclassified	Unclassified	Unclassified

17. LIMITATION OF ABSTRACT:
SAR

18. NUMBER OF PAGES
136

19a. NAME OF RESPONSIBLE PERSON (Monitor)
Aaron Veydt

19b. TELEPHONE NUMBER *(Include Area Code)*
N/A

Acknowledgements

Distribution List

Air Force Research Laboratory

AFRL/MLBT: Aaron R. Veydt, 2Lt, USAF — 1 e-mail copy: Aaron.Veydt@wpafb.af.mil
    Copy to: Dr. Stephen L. Szaruga — 1 e-mail copy; Steve.Szaruga@wpafb.af.mil
2941 P. Street, Rm 136
Wright-Patterson Air Force Base, Ohio 45433-7750

AFR/PKMM:L: Michael A. Cramer — 1 e-mail copy: Michael.Cramer@wpafb.af.mil
    Copy to: Rebecca Powers — 1 e-mail copy: Rebecca.Powers@wpafb.af.mil

Office of Naval Research – Administrative Grants Officer

Sandra Thomson — 1 e-mail copy: Sandra.Thomson@navy.mil
ONR Seattle Regional Office
1107 NE45th Street, Suite 350
Seattle WA 98105-4631

North Dakota State University

Dr. Gordon Bierwagen — 1 e-mail copy: Gordon.Bierwagen@ndsu.edu
Dr. Bret Chisholm — 1 e-mail copy: Bret.Chisholm@ndsu.edu
Dr. Séva Balbyshev — 1 e-mail copy: Seva.Balbyshev@ndsu.edu
DrEng. Dante Battocchi — 1 e-mail copy: Dante.Battocci@ndsu.edu
Dr. Kerry Allahar — 1 e-mail copy: Kerry.Allahar@ndsu.edu
Dr. Douglas Schulz — 1 e-mail copy: Doug.Schulz@ndsu.edu
Mr. Aaron Reinholz — 1 e-mail copy: Aaron.Reinholz@ndsu.edu
Dr. Philip Boudjouk — 1 e-mail copy: Philip.Boudjouk@ndsu.edu

Contact information for inquiries

Programmatic:
  Larry Pederson, Director CNSE
  1805 NDSU Research Park Dr. N.
  Fargo, ND 58102
    (701) 231-5284 (voice)
    (701) 231-7916 (fax)
    Larry.Pederson@ndsu.edu

Technical:
  Gordon Bierwagen, Professor
  Department of Coatings & Polymeric
    Materials
  1735 NDSU Research Park Dr. N.
  Fargo, ND 58102
    (701) 231-8294 (voice)
    (701) 231-8439 (fax)
    Gordon.Bierwagen@ndsu.edu

Financial:
  Mark Lande, Asst. Dir. CNSE
  Admin. and Financial Services
  1805 NDSU Research Park Dr.
  Fargo, ND 58102
    (701) 231-5882 (voice)
    (701) 231-7916 (fax)
    Mark.Lande@ndsu.edu

Summary

The overall goal of this program is to contribute to the development of the next-generation anti-corrosion and other protective coating systems for USAF aircraft. During the past year, NDSU's promising Mg-based primer was further optimized. Five different Mg alloy pigments were evaluated, and the optimal pigment volume ratio was established. Flexible binders were identified that substantially improved mechanical properties of the Mg-based primer without sacrificing corrosion properties. Research continued to implement high-throughput methods for coatings formulation and optimization, including development of a technique that enables high-throughput screening of the abrasion resistance of cured coatings. A hybrid organic-inorganic binder for Mg-based primers was developed that includes silica nanoparticles, which has been shown to provide excellent corrosion resistance to important aluminum alloys. Research continued to develop a rapid-cure Mg-rich primer system that would minimize out-of-service time when an aircraft is repainted. These "dual-cure" binder systems combine ambient-cured siloxane networks with a UV-curable cross-linked network. Progress was made in developing in-field methods to deposit transparent conducting oxide coatings on aircraft canopies by atmospheric pressure plasma methods. Such coatings are needed to dissipate static charge buildup on canopies when in service. Finally, NDSU has investigated the use of electrochemical sensors embedded between the Mg-rich primer and the topcoat, to monitor the degree of corrosion protection provided by the primer. A principal advantage of this approach is that the topcoat protects the sensor from the environment, which reduces electrochemical noise, improves measurement accuracy, and extends the sensor lifetime.

1.0 Introduction

The overall goal of this program conducted at North Dakota State University (NDSU) is to contribute to the development of the next-generation anti-corrosion and other protective coating systems for USAF aircraft. Technical progress had been made during the past year with respect to optimization of NDSU's promising Mg-based primer, application of high throughput methods to evaluate corrosion behavior of coated specimens, development of methods to deposit transparent conductive oxide coatings for in-field canopy repair, and development of prognostic measurement techniques to evaluate coatings performance.

This report consists of the following sections:
- **Section 2: Mg-Rich Primer Development** describes efforts to further enhance NDSU's Mg-based primer and to evaluate corrosion performance of the coating. This research was coordinated by Dr. Dante Battocchi, with Prof. Gordon Bierwagen as senior scientific advisor, and was performed in the Department of Coatings and Polymeric Materials (CPM) as Task 1.
- **Section 3: High-Throughput Experimentation for Coatings Formulation and Optimization** describes primer formulation optimization activities and the development of high-throughput electrochemical methods to evaluate corrosion of coatings. This work was led by Dr. Bret Chisholm, and performed in the NDSU Center for Nanoscale Science and Engineering (CNSE) as Task 3.
- **Section 4: Plasma Deposition of Inorganic Coatings** describes the development of methods to deposit indium tin oxide coatings for in-field canopy repair. This work was led by Dr. Doug Schulz, and performed at CNSE as Task 4.
- **Section 5: Coatings Prognostics** describes the application of embedded electrochemical sensors to evaluate the effectiveness of the magnesium-based primers previously developed. This research was led by Dr. Vsevolod Balbyshev at CNSE as Task 5.
- **Section 6: Program Management** lists key program contributors and their roles.
- **Section 7: Financial Summary** provides a summary of program expenditures for the reporting period.
- **Appendices** provide manuscripts submitted or published based on research and development performed on behalf of this program.

2.0 Mg-Rich Primer Development

The objective of Task 1 is to further optimize NDSU's magnesium-rich aircraft coating primer technology. This primer was designed as an alternative to chromate-based treatments corrosion control of Al alloys, particularly the aircraft alloy 2024-T3, and was developed with support from several U.S. Air Force grants. The anti-corrosive properties of the Mg-rich primer are based on two different mechanisms: firstly, the coating acts as a barrier; secondly, the coating acts as a cathodic protector with the pigment undergoing corrosion preferentially versus the Al substrate. During the past year, this work focused on the evaluation of different magnesium alloy pigment composition as well as development of flexible binders.

The suitability of five different magnesium alloys were evaluated as pigments in the Mg-rich primer and their characterization is almost complete. A manuscript on this subject has been published in the NACE Corrosion journal[1]. In recent months the work was focused on optimizing pigment volume concentrations (PVC), which is highly influenced by particle size and aspect ratio.

The use of flexible binders for the Mg-rich primers has been addressed during the past year. In this work, a number of testing methods were applied to measure the electrochemical and mechanical properties of the newly developed Mg-rich primer which is based on polysulfide binders. To investigate if the Mg-rich flexible primer has better or equal corrosion protection property as well as improved flexibility, a commercialized epoxy-based Mg-rich primer was used as comparison control.

2.1 Electrochemical Measurements

AA 2024-T3 panels were pretreated by bath pretreatment and coated with Mg-rich primers with different PVCs. Then the samples were topcoated before being sent to the weathering chambers. Two accelerated weathering protocols are carried out: ASTM B-117 and ASTM D 5849. Electrochemical data: impedance, open circuit potential, and noise resistance, were collected after each week exposure as well as at the beginning of the exposure. According to the data presented in Figures 2.1, 2.2, 2.3, and 2.4, the following conclusions were drawn:

- the open cell potential (OCP) decreased within 2 weeks to a value that typically should not be able to provide cathodic protection;

- corrosion rates, directly related to noise resistance, decreased suddenly after a 6-week exposure;

- coatings from B117 have more negative OCP and lower impedance after weathering compared to those from Prohesion/QUV; and

- coatings prepared with non-flexible primers have more positive OCPs than flexible ones, while flexible primer has lower impedance than the non-flexible peer.

2.2 Mechanical Measurement

Conical mandrel bending tests and reverse impact resistance tests are two typical methods to evaluate coatings' mechanical property. The results are shown in Table 2.1 and Figure 2.5.

Reduced modulus and hardness obtained by nano-indentation technique refer to local mechanical properties of primers, for which typical test results are given in Figure 2.6. Both dynamic and static modulus can be measured by dynamic mechanical analysis (DMA). Bending tests and impact tests demonstrated the flexibility of Mg-rich polysulfide primer. At the same pigment volume concentration,

primers formulated with flexible binders showed better performance with regard to mechanical properties at room temperature.
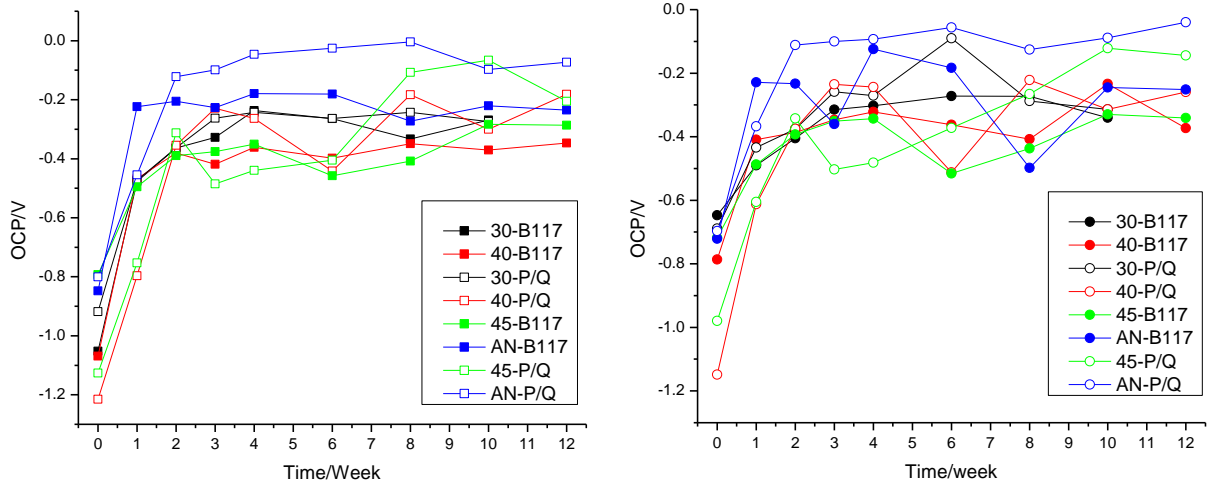
Figure 2.1. (left): Open cell potential (OCP) obtained by electrochemical impedance spectroscopy (EIS) vs. accelerated weathering exposure time; (right) OCP obtained electrochemical noise measurement (ENM vs. accelerated weathering exposure time.)
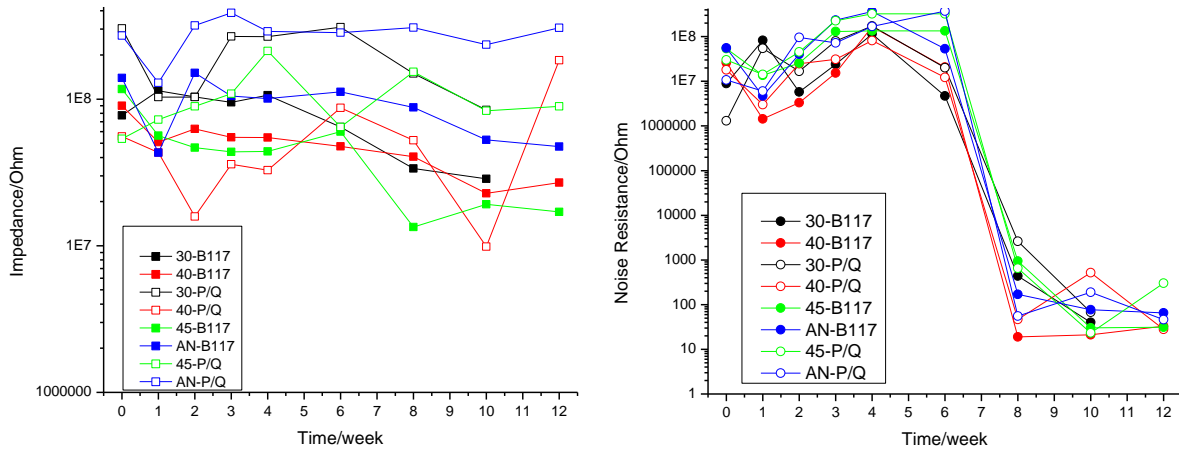
Figure 2.2. (left): Impedance obtained by EIS vs. accelerated weathering exposure time; (right) noise resistance obtained by ENM vs. accelerated weathering exposure time.

Table 2.1. Reverse impact resistance test results based on different PVC primers

Primer Pigment Volume Concentration	Impact Resistance (in×lb)
30%	22
40%	26.8
45%	17.6
50%	6
AN	12

Conical Mandrel Bending Tests

■ 30% PVC Flexible Primer ■ 40% PVC Flexible Primer □ 50% PVC Flexible Primer □ 45% PVC No-flexible Primer
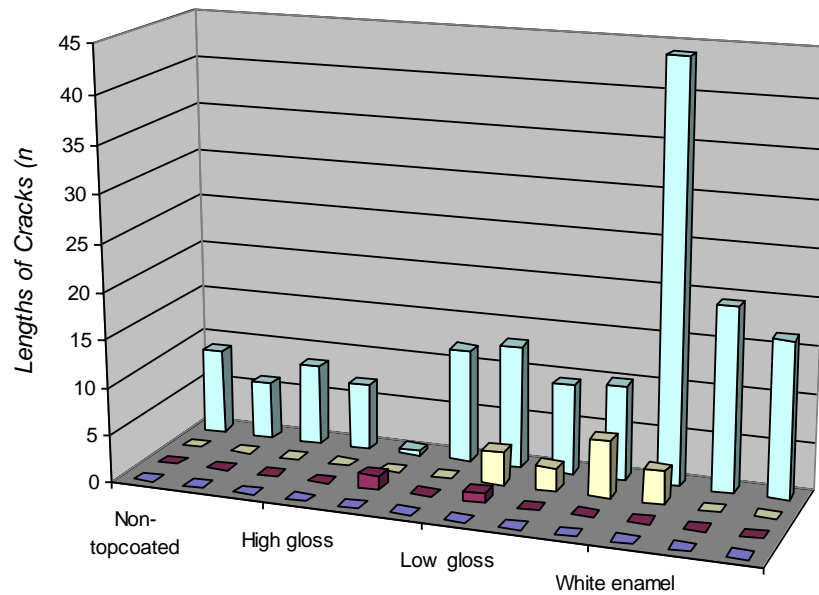
Figure 2.3. Bending test results based on lengths of cracks on different topcoat/primer combinations.
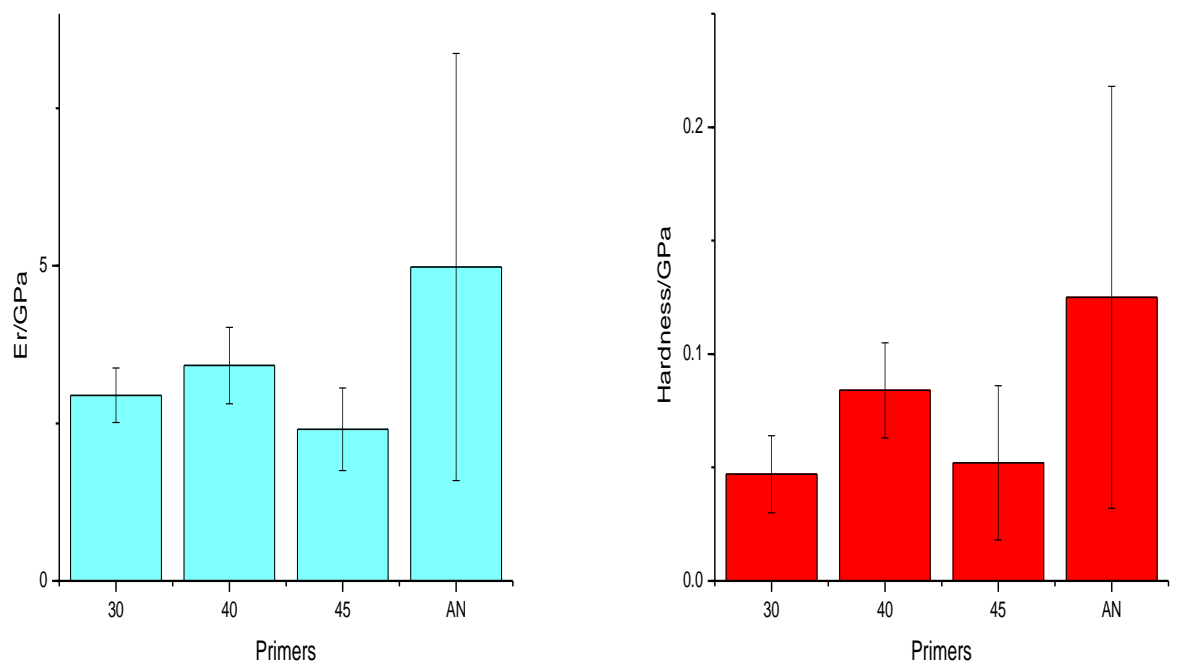
Figure 2.4. Comparisons between flexible and non-flexible primers on reduced modulus (left) and hardness (right). Primers with 30, 40, and 45% PVC contain flexible binders.

Sample: Comp45%-Instron
Size: 29.6487 x 5.0000 x 0.0650 mm
Method: Stress/Strain

DMA

File: C:...\DMA\2009\ini-static\25-AN.002
Operator: Tiantian
Run Date: 09-Apr-2008 15:31
Instrument: DMA Q800 V7.4 Build 126
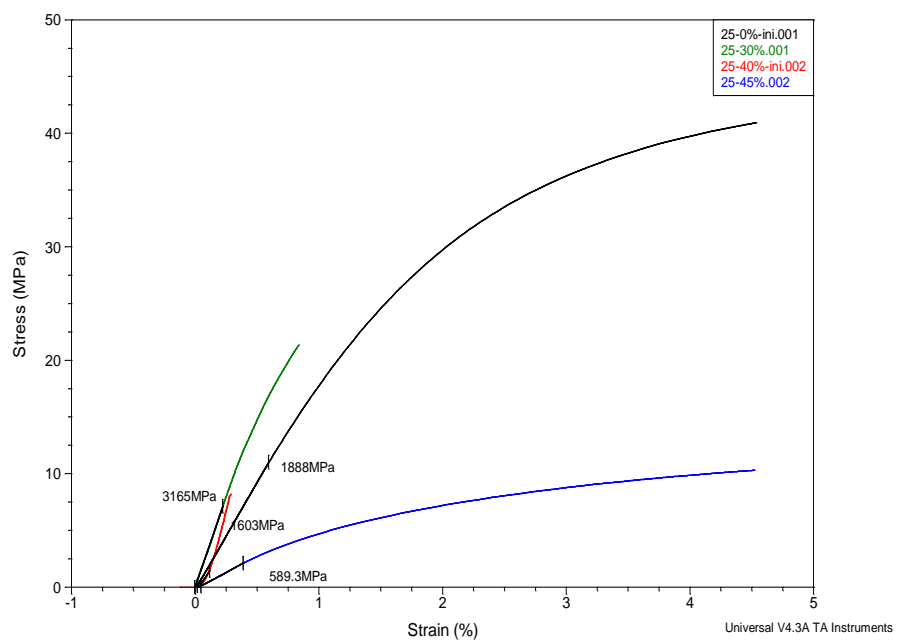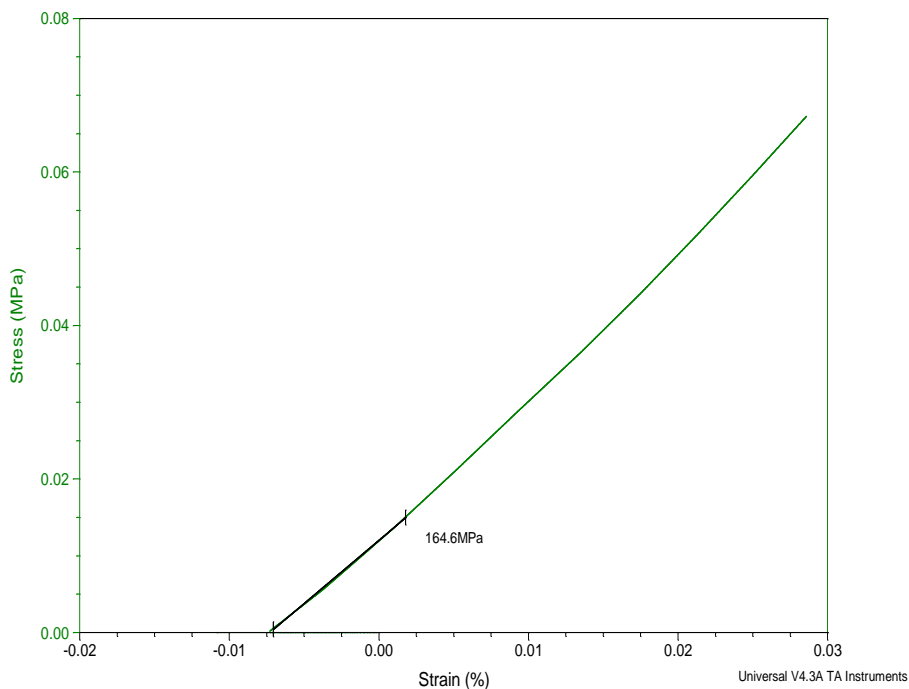
Figure 2.5. Stress-strain curves at room temperature: (top) 45% PVC flexible and (bottom) non-flexible primer films were measured at the load ramp 0.05N/min; while 0, 30% & 40% PVC primer films were measured at 0.4N/min.
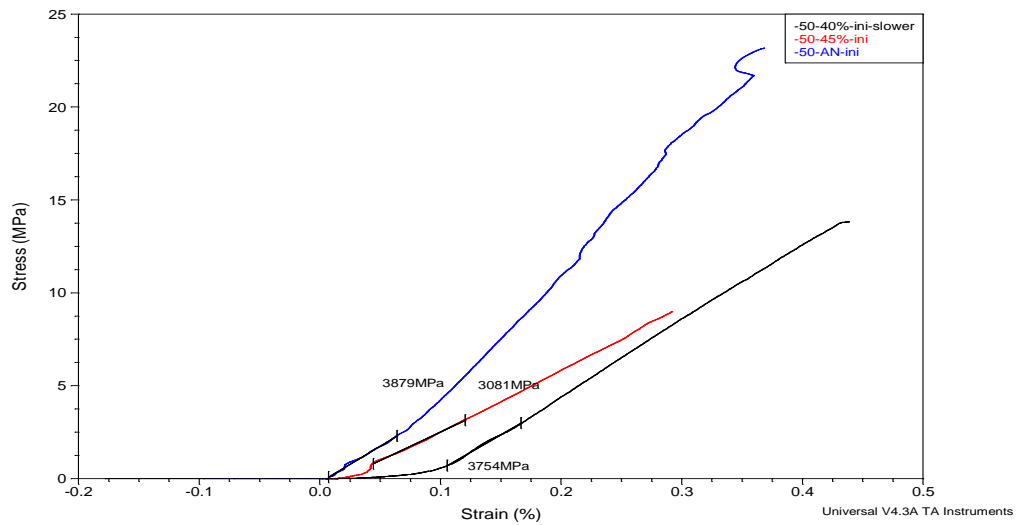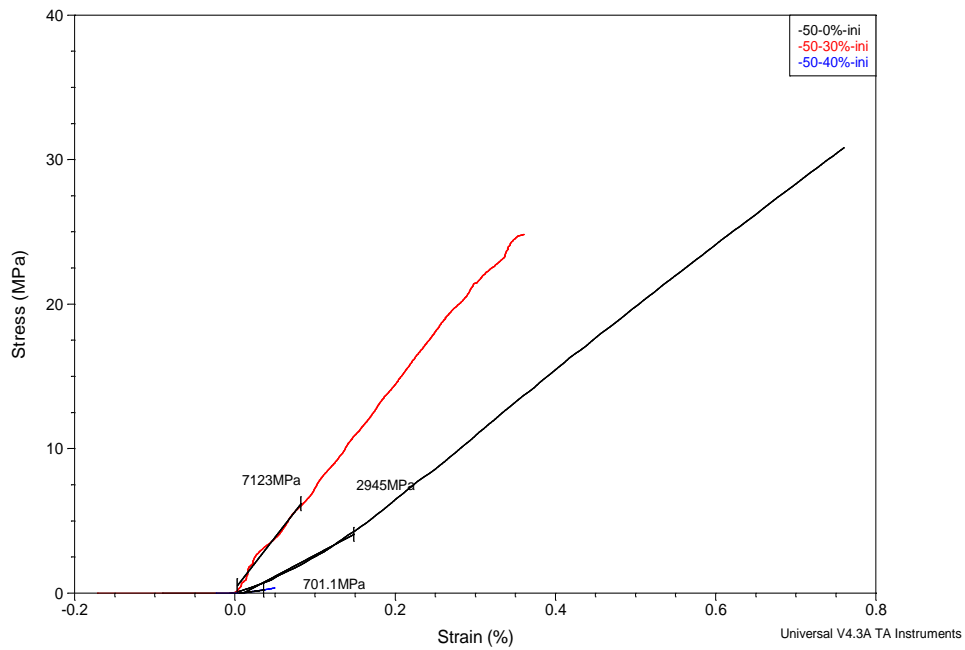
Figure 2.6 Stress-strain curves at -50°C. For the flexible primer, data were collected at a load ramp of 0.4N/min (top) and at a load ramp of 0.05N/min (bottom). For the non-flexible primer film, data were collected at a load ramp of 0.025N/min.

References for Section 2

1.   H. Xu, D. Battocchi,* D. Tallman and G. Bierwagen, "The use of Magnesium alloys as pigments in Mg-rich primers for protecting Al Alloys" *Corrosion*, **65** [5] May 2009.

3.0 High-Throughput Experimentation for Coatings Formulation and Optimization

3.1 Development of New High-Throughput Methods.

A simple apparatus was developed that allows for the high throughput screening of cured coatings based on their relative abrasion resistance. The system functions by loading arrays of coating samples onto the modified deck of an oscillating shaker table to provide the correct amount of movement for our 1x1.5 inch rectangular coating patches. The oscillating table rotates around a 0.75 inch diameter circle with an adjustable rpm and duration. The optimal abrading times and rpm are a function of coating scratch resistance and abrasive hardness and are fully adjustable. The down force of the 32 individual abrasive pads is controlled by 32 pneumatic cylinders (Figure 3.1) all connected to a single precision pressure regulator and test gauge. We chose this method over springs or other mechanical systems because it provides for a highly uniform down force to each sample regardless of sample thickness or deck location. They also allow for each of the four substrate locations to be turned on or off depending on how many of the deck positions are filled, resulting in the non-used pads to automatically retract out of the way.
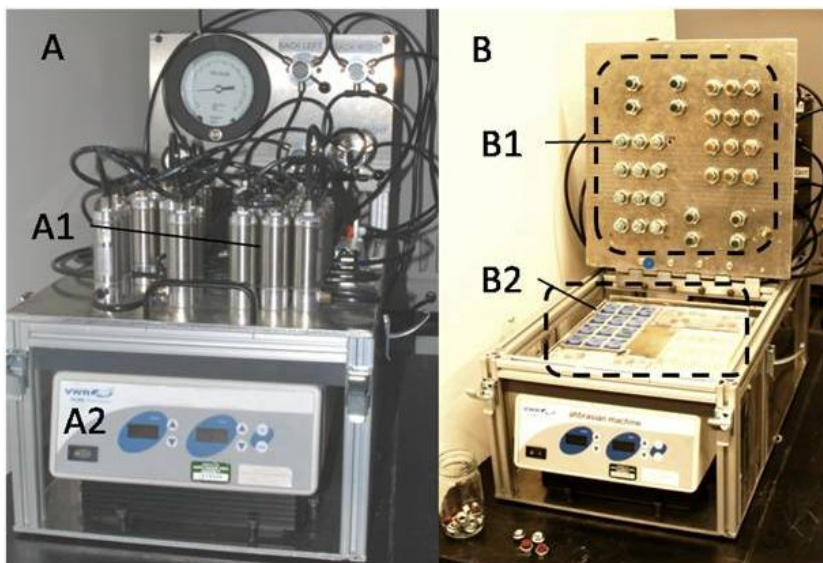
Figure 3.1. High Throughput Abrasion Testing Machine; A1-32 individual pneumatic cylinders, A2-rotary shaking table, B1-32 interchangeable abrasive pads, B2-polymer array plate deck.

The abrasive pads are glued to a flanged stainless steel nut that is simply threaded onto the end of each air cylinder shaft allowing for easy removal and replacement of the abrasive pads. The pads can be made from commercially available cleaning pads such as Scotchbrite™ by simply punching disks out of the pads and gluing them to the flange nuts. The nylon mesh cleaning pads are available in a range of grit size and hardness and are cheap and easy to use. Less aggressive abrasion pads can be cut from wool or cotton felt and used dry or in conjunction with a slurry paste made from fine powdered abrasive and water. Figure 3.2 shows a single 12 sample array panel coated with a UV cured epoxy coating that has been subjected to the following abrasion conditions; 82 rpm, 2 psi down force, for 2.75 minutes (approx. 225 rotations) with dry medium abrasive nylon mesh pads.

Figure 3.2. Close-up view of the high-throughput abrasion testing machine showing a twelve sample array panel loaded in one of four deck positions. *Note the circular abrasion marks on each of the UV-cured epoxy coating samples.*

The example shown in Figure 3.2 would be considered a very aggressive abrasion challenge and was performed to provide a photograph with the most contrast. Less aggressive, longer term abrasion runs are more representative and the resulting abrasion marks are more subtle. These plates can then be assessed for abrasion resistance by measuring the changes in the coating gloss before and after the exposure to abrasion. The change in coating gloss is measured on the automated color and gloss station that was built by our engineering staff a few years ago.

The high throughput electrochemical Impedance spectroscopy (EIS) apparatus that was built a year ago received the upgraded addition of the automated fluid delivery and extraction system to improve its ease of use. Essentially, the new system allows for the automated filling and extraction of fluids from the individual wells of the existing 12 well EIS apparatus. Fluid delivery is controlled by valves and powered by gravity while fluid removal is facilitated by vacuum suction and valving. To save money, no liquid pumps were used. Figure 3 shows the fluid reservoirs (A1) above the valve control box (A2) connected to the previously built 12-well EIS array chamber. Currently, three solutions are plumbed to the system and will normally consist of dilute Harrison's solution, sodium chloride solution, and water. The sodium chloride solution could easily be changed out for a challenge solution such as an acid or base to allow for *in-situ* coating exposure followed by further measurements of changes in the coatings barrier properties.

The valve control box (A2 above) contains a number of timing relays and switches to provide the proper sequence of valve opening and closing to automatically empty, fill, or rinse a set row of wells. Each EIS electrode assembly (B2 above) contains the reference and counter electrodes in addition to 3 separate tubings to allow the electrolyte, salt, water, or challenge solutions to be added to the appropriate depth as well as be extracted completely from each well. This semi-automated fluid delivery system allows for all 12 wells of a test substrate to be exposed to the solutions for similar amounts of time to ensure that unwanted aging of the coating samples does not occur.
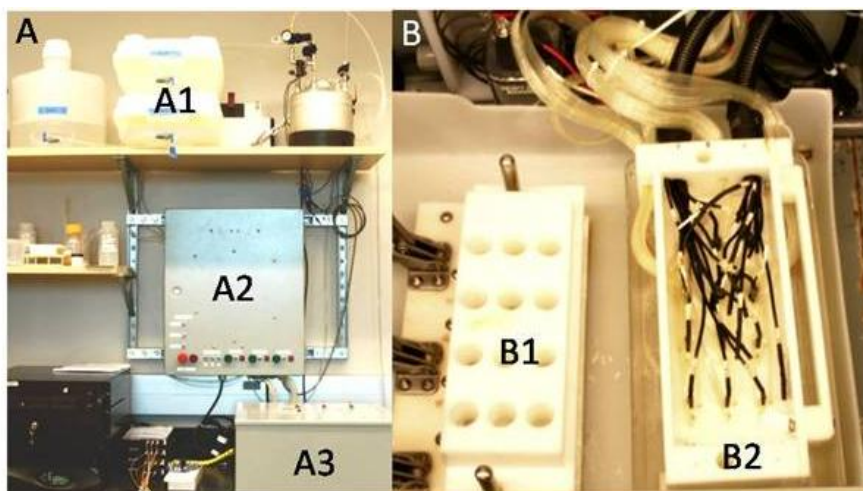
Figure 3.3. High-Throughput EIS Liquid Delivery and Extraction System; A1-liquid solution storage, A2- Valve control box, A3-EIS well array chamber, B1-12 well EIS array block, B2-12 well EIS electrode and fluid tubing assembly.

3.2 Mg-rich Primers Based on Hybrid Organic-Inorganic Binders.

As discussed in the 2008 annual report as well as in a publication in the Journal of Coatings Technology,[1] Mg-rich primers based on a hybrid organic-inorganic binder derived from silica nanoparticles (Si-nano) and phenethyltrimethoxysilane (PhETMS) gave excellent corrosion protection of Al 2024-T3. Work has continued on these coatings with particular emphasis on the synthesis of the Si nano-based binder system. Figure 4 illustrates the synthetic process used to create the Si-nano-based binder system. The extent of siloxane bond formation that can occur both during the preparation of the binder solution as well as during curing of the coating was expected to be strongly affected by the use of a catalyst that promotes silanol condensation reactions. As a result, the influence of the addition of tetrabutylammonium fluoride (TBAF), a known catalyst for promoting silanol condensation reactions, on the properties of both the binder system and cured coatings was investigated.
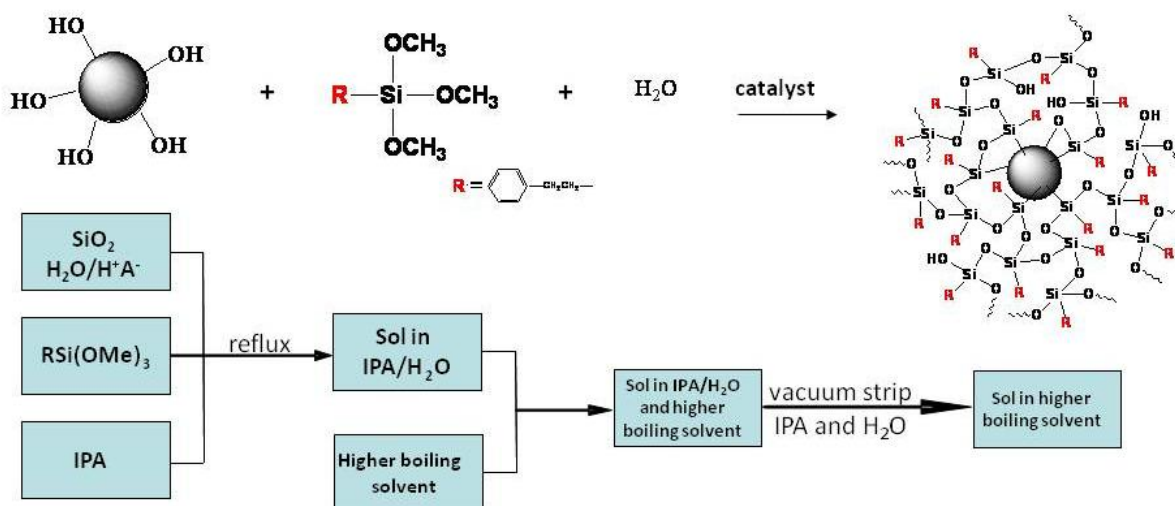
Figure 3.4. A schematic of the synthetic process used to create the Si-nano-based binder system for Mg-rich primers.

10
11

As indicated in Figure 3.4, condensation of silanols present on the surface of the Si-nano with PhETMS was expected to result in an increase in Si-nano particle size. As a result, particle size measurements of Si-nano binders produced in the absence and in the presence of TBAF were made using laser light scattering. The results shown in Figure 3.5 clearly indicate an increase in particle size of Si-nano after reaction. The higher increase in particle size as result of the use of TBAF indicates a higher degree of Si-nano surface silanol condensation. In addition to particle size measurements, silicon-29 nuclear magnetic resonance spectroscopy (^{29}Si NMR) was used to directly characterize the extent of silane and silanol condensation. The lack of a peak corresponding to T_o ($\delta = -42.5$ ppm) in Figure 3.6 showed that all of the PhETMS had undergone at least one condensation reaction. Consistent with the particle size results, the addition of TBAF to the reaction mixture resulted in a higher extent of PhETMS condensation as indicated by the higher T_3/T_1 ratio.

Number Average Particle Size/nm
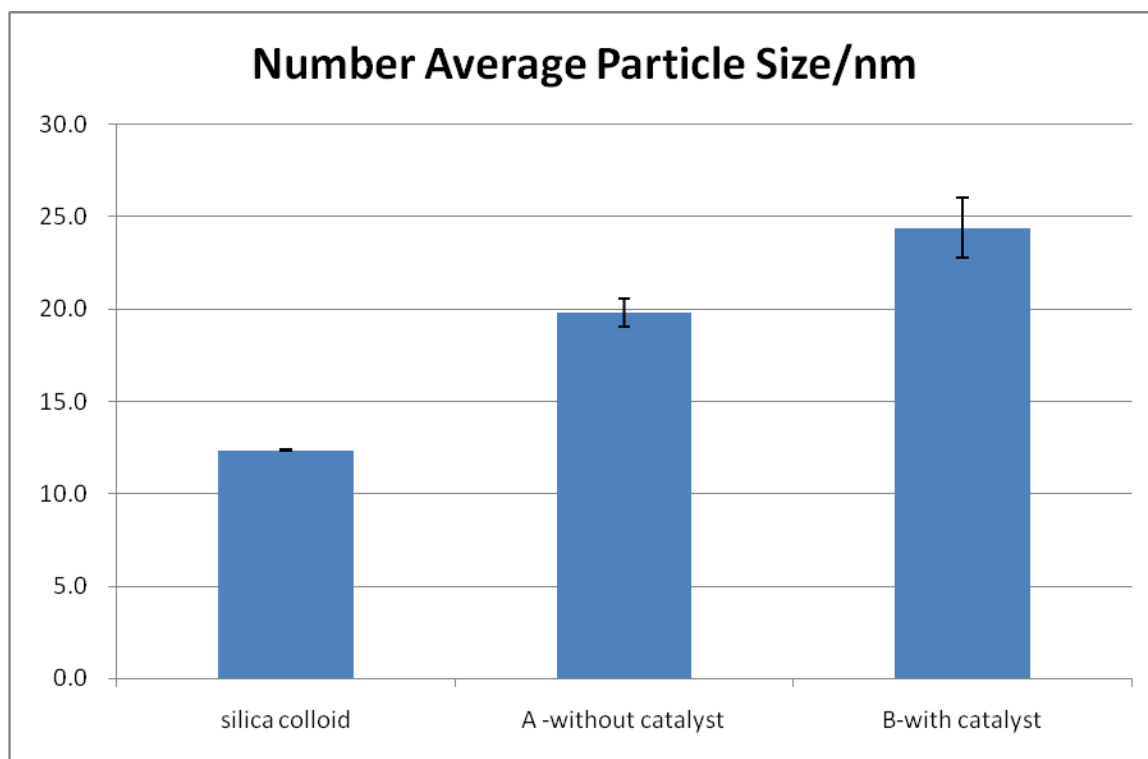
Figure 3.5. Particle size data obtained using laser light scattering.
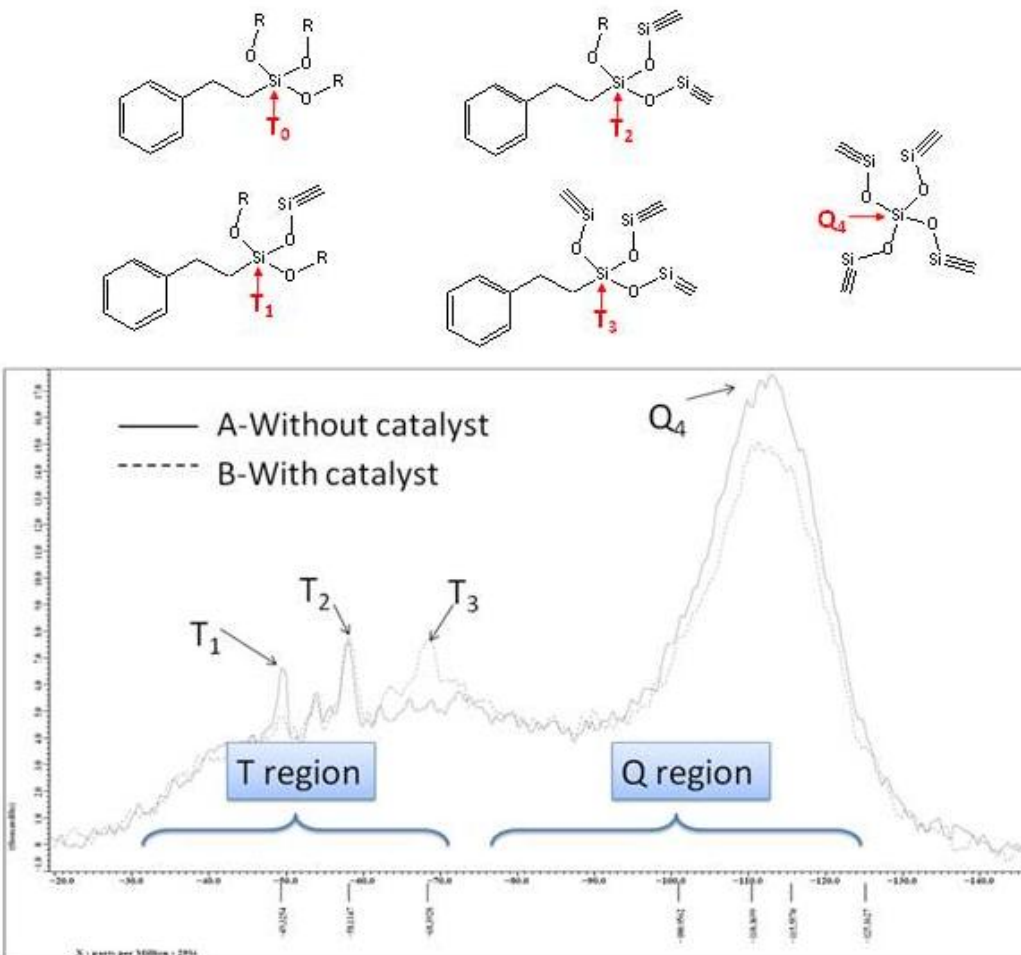
Figure 3.6. ^{29}Si NMR spectra of binder solutions produced in the absence and the in the presence of TBAF.

To determine the affect of TBAF on the properties of the cured binder system, the two binder systems (with and without TBAF) were coated on to aluminum 2024-T3 panels and the coatings cured using three different curing conditions. The three different curing conditions used were ambient conditions for 24 hours, 80 $^{\circ}$C for 1 hour, and 80 $^{\circ}$C for 24 hours. Since the barrier properties of a coating are very important for corrosion protection, electrochemical impedance spectroscopy (EIS) was used to characterize the cured coatings. As shown in Figure 3.7, cure conditions strongly affected low frequency impedance. For the coating prepared without TBAF (noTBAF), impedance increased with an increase in the thermal energy used for curing. With regard to the affect of TBAF, impedance was highest for the TBAF-containing coatings (wTBAF) cured using elevated (i.e. 80 $^{\circ}$C) temperature. As expected, these results suggest that the addition of TBAF and an increase in the thermal energy used for curing enable higher levels of silane and silanol condensation resulting in higher crosslink density and, thus, higher barrier properties. Higher silane and silanol condensation was confirmed by obtaining FT-IR spectra of the coatings using the various curing conditions. Figures 3.8 and 3.9 display FT-IR spectra obtained for the coating solution and cured coatings produced from noTBAF and wTBAF, respectively. The peak at 1496 cm^{-1} which is attributed to carbon to carbon stretching motions within the aromatic ring of PhETMS was used to normalize relative variations in the large peak centered at 1120 cm^{-1} which is attributed to vibrations associated with the SiOCH$_3$ groups. Figure 3.10 shows variations in the normalized peak intensity of the 1120 cm^{-1} band as function of curing condition. The reduction in methoxysilane

concentration resulting from condensation reactions decreased with increase thermal energy used for curing. The uncured wTBAF coating had a lower relative methoxysilane concentration as compared to the noTBAF coating solution. Likewise, coatings derived from the wTBAF coating solution possessed a lower relative methoxysilane concentration as compared to coatings derived from noTBAF and cured using the same condition.

Figure 3.7. Low frequency impedance (0.01 Hz) of coatings derived from the Si-nano binder systems and various cure conditions.
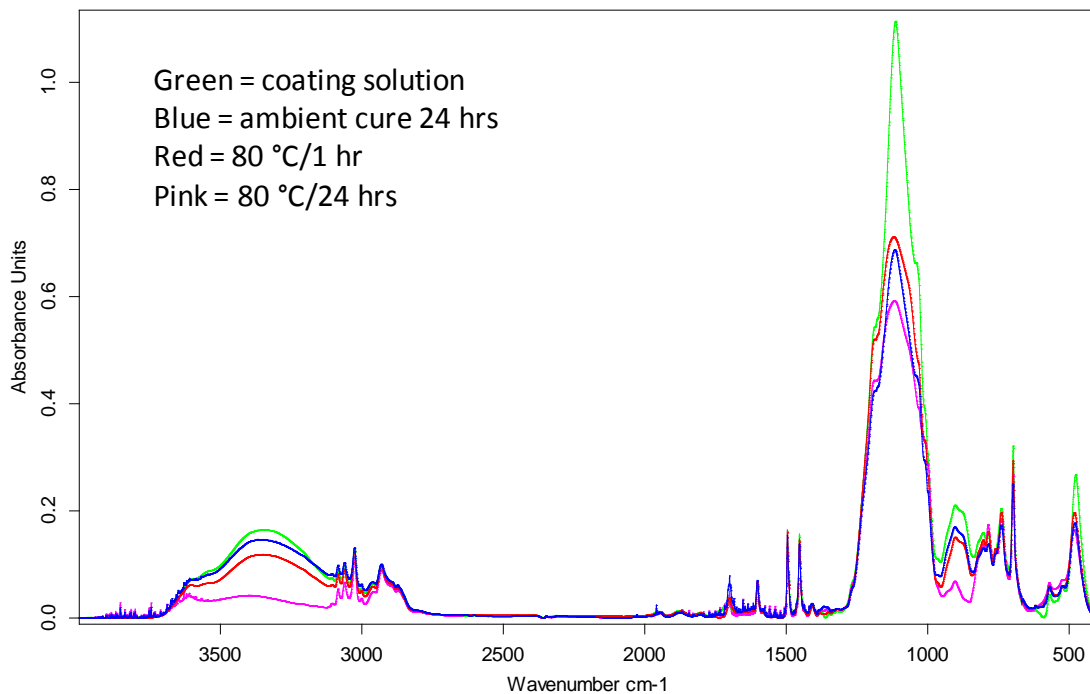
Figure 3.8. FT-IR spectra obtained for the coating solution and cured coatings produced from the Si-nano-based binder system produced without the use of TBAF as a catalyst.
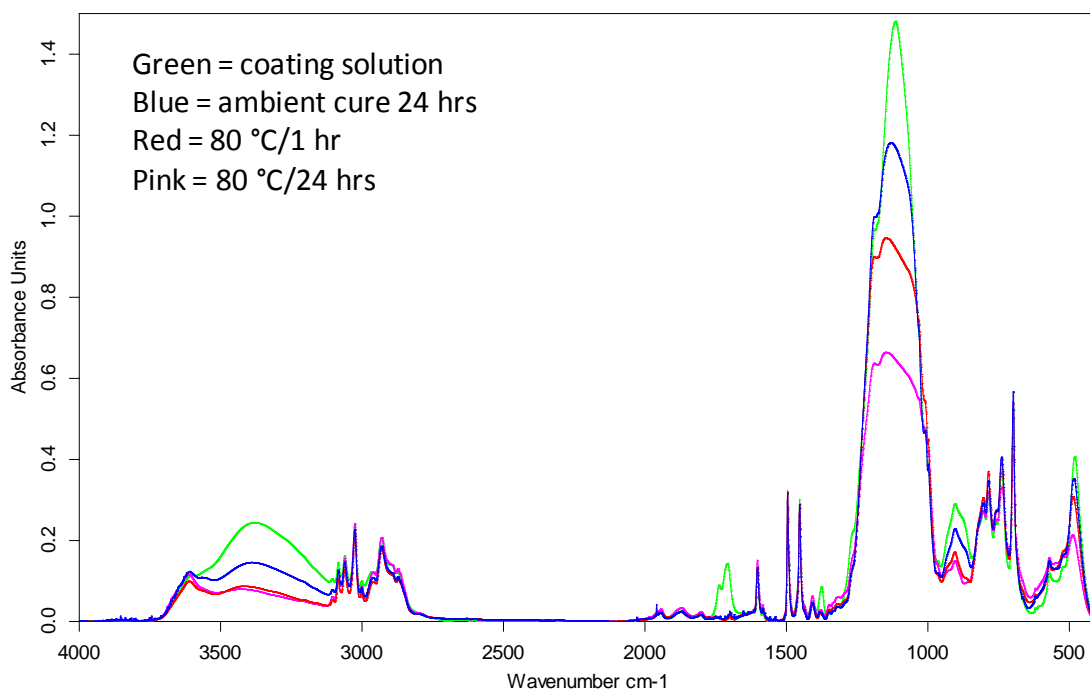
Figure 3.9. FT-IR spectra obtained for the coating solution and cured coatings produced from the Si-nano-based binder system produced with the use of TBAF as a catalyst.
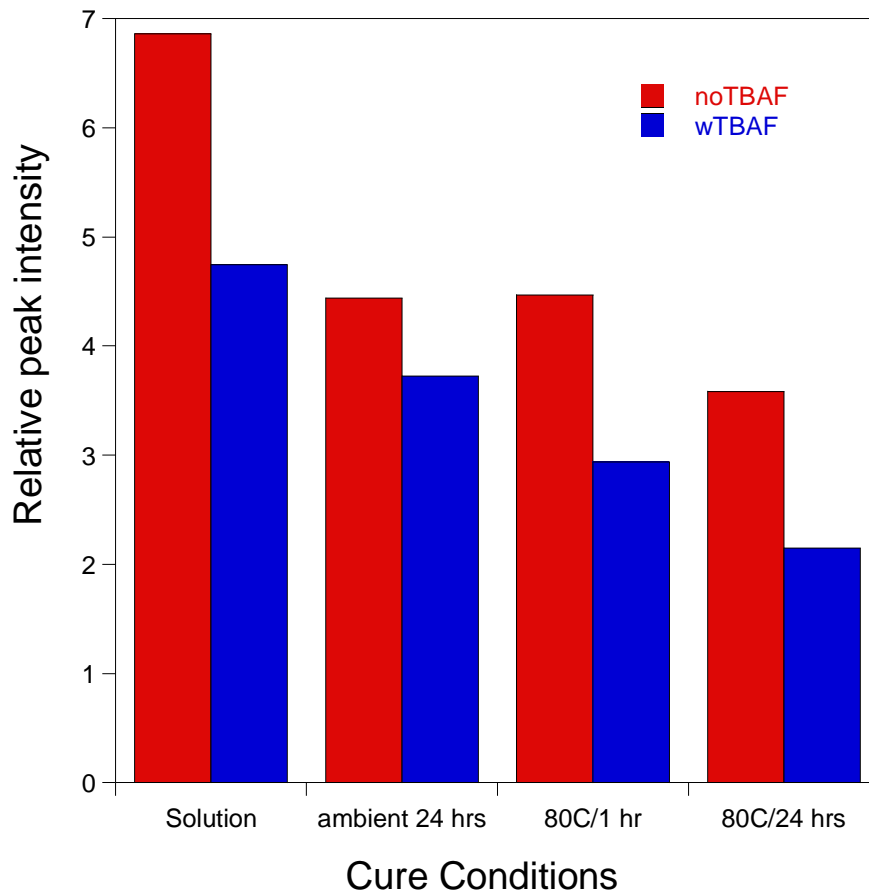
Figure 3.10. Normalized peak intensity of the 1120 cm^{-1} band as function of curing condition.

The two binder systems were used to prepare Mg-rich primers containing 80 wt. % Mg particles. This high level of Mg particles was used to ensure that physical contact between Mg particles as well as Mg particles and the aluminum substrate would occur. Physical contact is needed to enable the conductivity between Mg particles and the substrate required for galvanic corrosion protection. EIS was used to characterize the Mg-rich coatings produced. As shown in Figure 3.11, the Mg-rich coatings based on wTBAF possessed much lower low frequency impedance than coatings produced from noTBAF. For these highly Mg filled coatings, the low frequency impedance is related to the conductivity of the coatings. The much lower impedance observed for the coatings derived from wTBAF was very interesting and suggested that the presence of TBAF strongly influences conductivity of the coating. The increased conductivity could be due to enhanced Mg interparticle contact due to a higher density of the Si-nano binder stemming from a higher level of Si-O-Si bond formation and/or higher conductivity stemming from the ionic nature of TBAF.
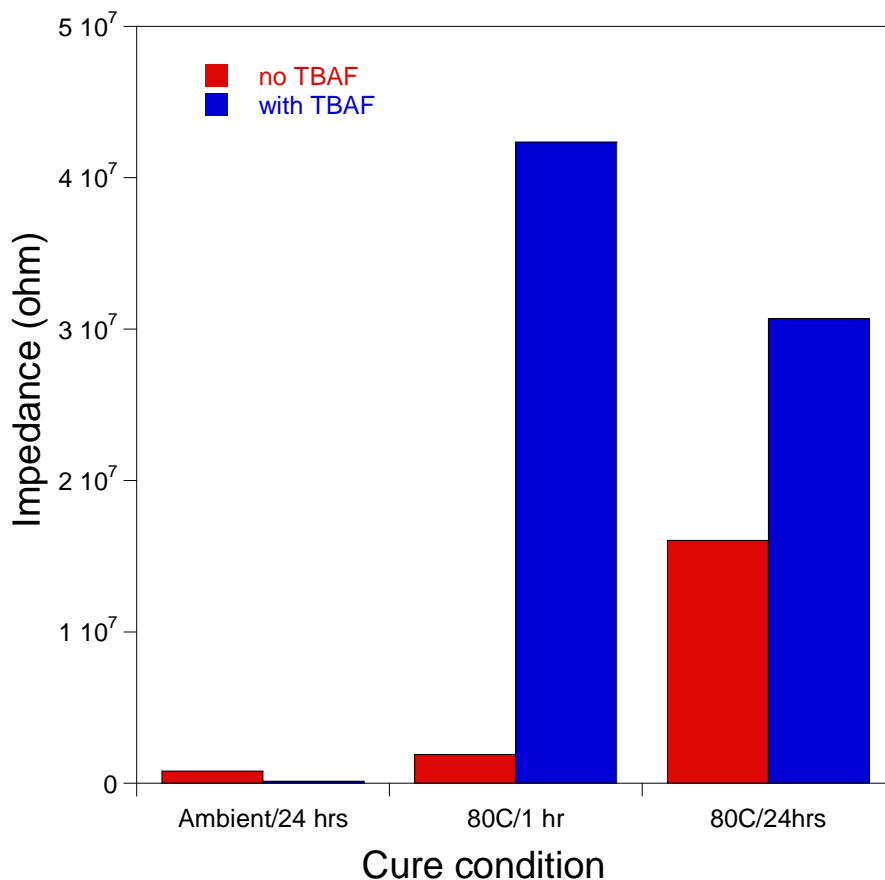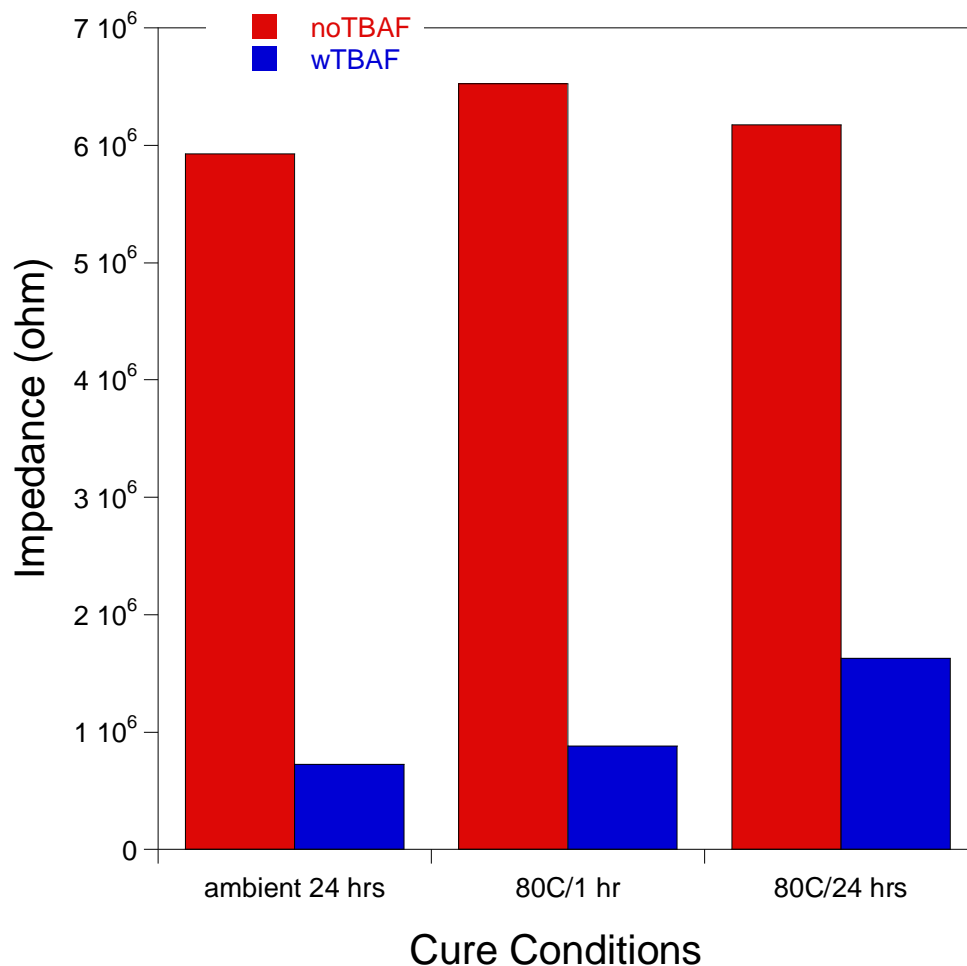
Figure 3.11. Low frequency impedance (0.01 Hz) of Mg-rich coatings derived from the Si-nano binder systems and various cure conditions.

The six Mg-rich primers produced were topcoated with a polyurethane topcoat and corrosion resistance was investigated using B117 salt spray exposure. Figures 3.12 and 3.13 display images of scribed panels subjected to B117 salt spray exposure for different durations. From Figure 3.12, it can clearly been seen that increasing the thermal energy associated with curing of the Mg-rich primer dramatically improved corrosion protection. Based on the previous work involving characterization of the Si-nano binder system and the effect of cure on binder properties, this improvement in corrosion protection can be attributed to the higher levels of silane and silanols condensation obtained with the increase in thermal energy. Coatings derived from an Mg-rich primer cured at 80 °C for 24 hours showed excellent corrosion protection. Even after 4,400 hours of B117 salt spray exposure the samples showed no blistering or delamination near the scribe. With regard to the effect of the condensation catalyst, TBAF, a comparison of Figure 3.12 to Figure 3.13 clear shows that the use of the catalyst dramatically reduced corrosion protection. All of the samples produced regardless of primer cure conditions showed some degree of blistering. By cutting the blisters with a razor blade, it was determined that cohesive failure within the primer layer was responsible for the blisters. At this point, the underlying mechanism for the generation of the blisters associated with the use of TBAF is not known. Since the ionic nature of the condensation catalyst may be contributing to the enhanced corrosion protection, work is currently being done to determine if a nonionic condensation catalyst such as dibutyltindiacetate will provide better performance.

	500 h	1000 h	1500 h	2000 h	2500 h	3000 h	4400 h
25°C/24h	A2524	A2524	A2524	A2524	A2524	A2524	A2524
80°C/1h	A8001	A8001	A8001	A8001	A8001	A8001	A8001
80°C/24h	A8024	A8024	A8024	A8024	A8024	A8024	A8024

Figure 3.12. Images of scribed panels of topcoated samples based on the noTBAF binder system after B117 salt spray exposure. Moving from left to right, salt spray exposure increased. Moving from top to bottom, the amount of thermal energy used to cure the Mg-rich primer increased.

	500 h	1000 h	1500 h	2000 h	2500 h	3000 h	4400 h
25°C/24h	B2524	B2524	B2524	B2524	B2524	B2524	B2524
80°C/1h	B8001	B8001	B8001	B8001	B8001	B8001	B8001
80°C/24h	B8024	B8024	B8024	B8024	B8024	B8024	B8024

Figure 3.13. Images of scribed panels of topcoated samples based on the wTBAF binder system after B117 salt spray exposure. Moving from left to right, salt spray exposure increased. Moving from top to bottom, the amount of thermal energy used to cure the Mg-rich primer increased.
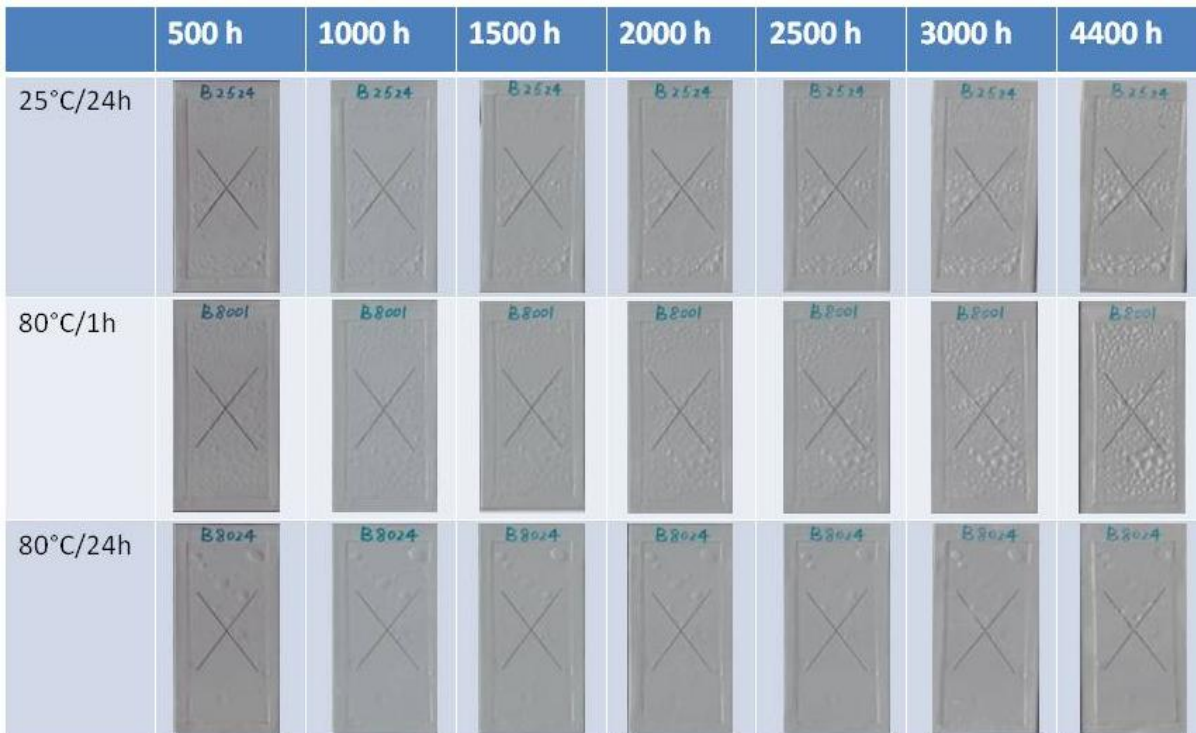
3.3 Rapid-cure Mg-rich Primers Based on a Dual-Cure Polymerization Mechanism.

Based on Air Force needs for a rapid-cure coating system for aircraft that minimizes the amount of time the aircraft is out of service for repainting, we have been working on developing a dual-cure binder system for Mg-rich primers. Details of the initial work that was performed is described in a conference proceeding for the 2008 *FutureCoat* symposium.[2] The focus of this initial work was to understand the influence of the UV-cured crosslinked network on the formation of the ambient-cured siloxane network. This initial work was done using a solvent-based binder system. Subsequent work conducted over the past year has involved solvent-free, dual-cure binder systems.

The reactive diluents that were initially investigated for potential use in conjunction with the trimethoxysilane-0functional epoxy acrylate (TMS-BAGD) that was described in last year's annual report (Figure 3.14) are shown in Table 3.1. This set of reactive diluents was chosen based on the diversity of acrylate functionality. SR-339, SR-531, and SR-285 are all monoacrylate reactive diluents while SR-306 is a diacrylate and SR-351 and SR-454 are triacrylate reactive diluents. Initial experimentation with the reactive diluents involved measurements of viscosity and cured film integrity of blends of the reactive diluents with TMS-BAGD at reactive diluents concentrations of 25, 50, and 75 wt. %. Coatings based on the monoacrylate reactive diluents, SR-339 and SR-285, showed extensive cracking and delamination upon cure and, thus, were eliminated from further investigation. Figure 3.15 shows the viscosity of blends based on the other four reactive diluents. All of the coatings possessing a TMS-BAGD concentration of 75 wt. % possessed a viscosity that was considered to be too high for use in an Mg-rich primer. As a result, only 75/25 and 50/50 reactive diluent/TMS-BAGD blends were investigated further.
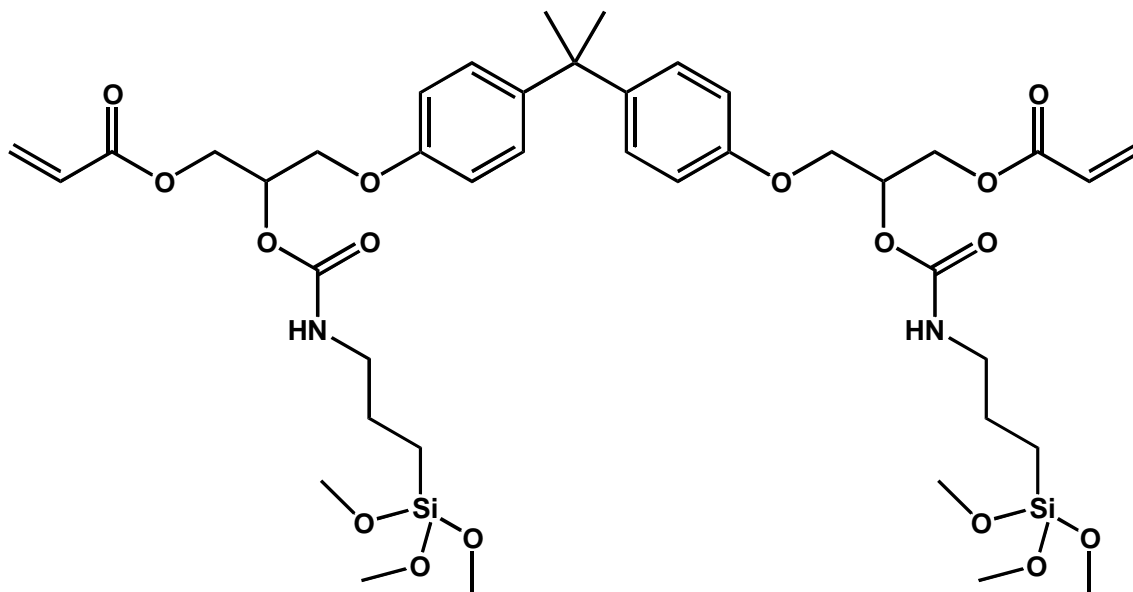
Figure 3.14. Chemical structure of TMS-BAGD.

Table 3.1. Chemical structures of the reactive diluents initially investigated.

Chemical Abbreviation and Trade Name	Structure and Description
2-phenoxyethyl acrylate (SR-339)	
Cyclic trimethyllipropane formal acrylate (SR-531)	
Tetrahydrofurfuryl Acrylate (SR-285)	
Tripropylene Glycol diacrylate (SR-306)	
Trimethylolpropane triacrylate (SR-351)	
Ethoxylated trimethylolopropane triacrylate (SR-454)	
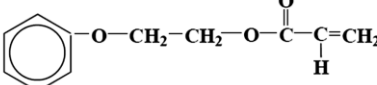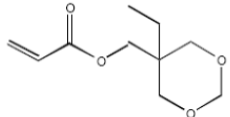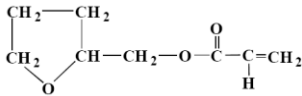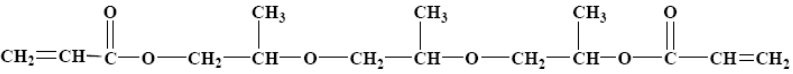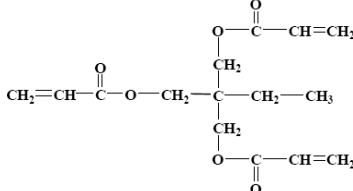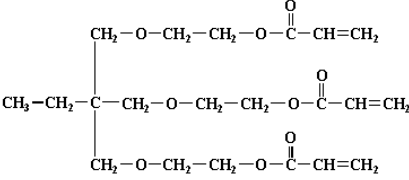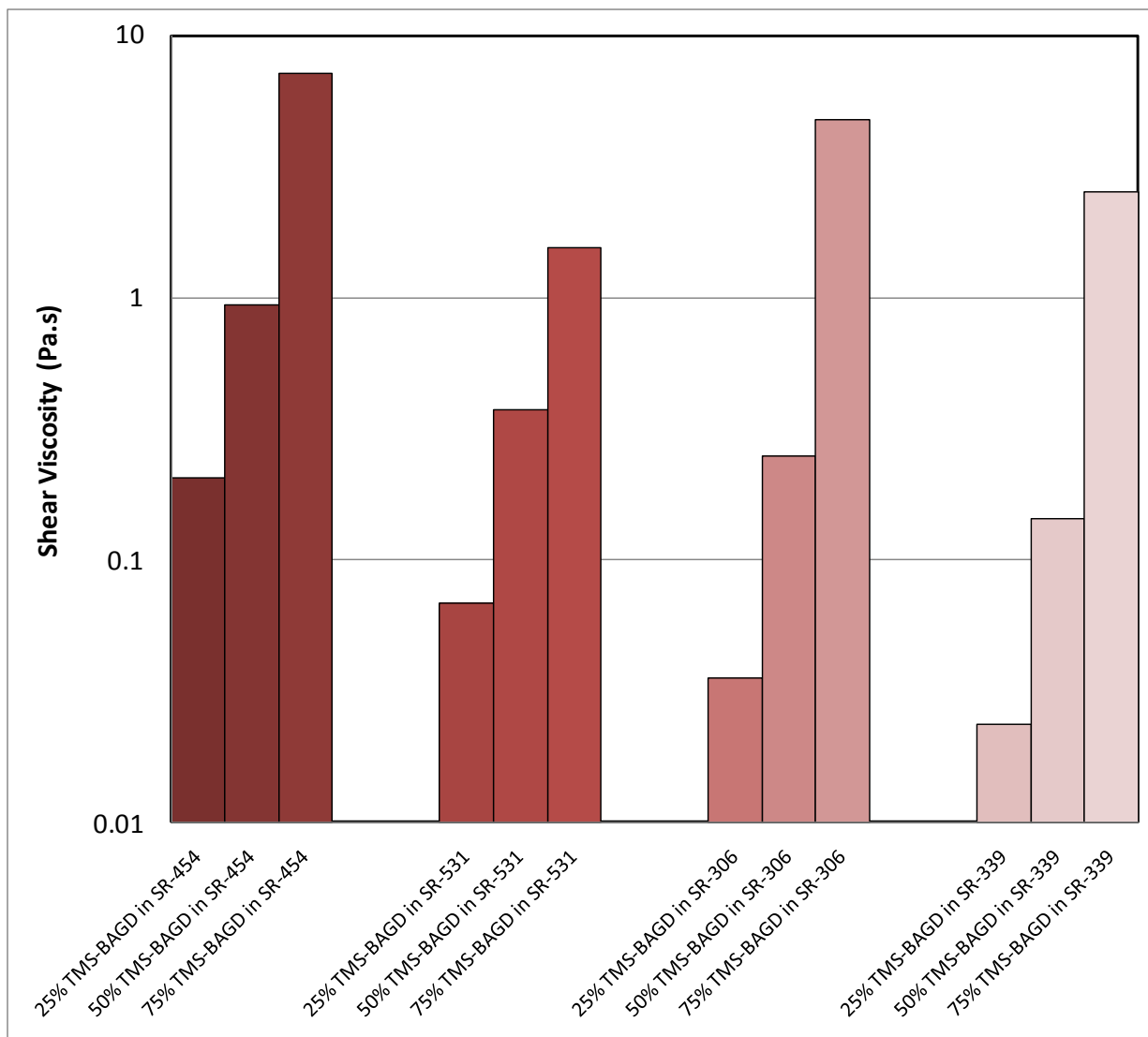
Figure 3.15. Viscosity of UV-curable coatings based on binary blends of the various reactive diluents and TMS-BAGD.

To determine the barrier properties of the cured films generated from the coatings, electrochemical methods were utilized. Figure 3.16 displays the results of potentiodynamic measurements made on coatings cast and cured over Al2024-T3. The electrochemical characteristics derived from the polarization curves are listed in Table 3.2. The coatings based on SR-454 as the reactive diluents showed the highest open circuit potential (OCP) and the lowest corrosion current indicating the highest barrier properties. In contrast, the coatings based on SR-306 as the reactive diluent showed the poorest barrier properties. Considering the fact that SR-454 was the acrylate with the highest acrylate functionality and, as a result, would produce the highest crosslink density, it was not surprising that it provided the highest barrier properties. It was, however, surprising that the two monofunctional acrylates, SR-339 and SR-531, provided better barrier properties than the difunctional acrylate, SR-306. Based on this data, further experimentation was limited to use of SR-454 and SR-531 as reactive diluents.
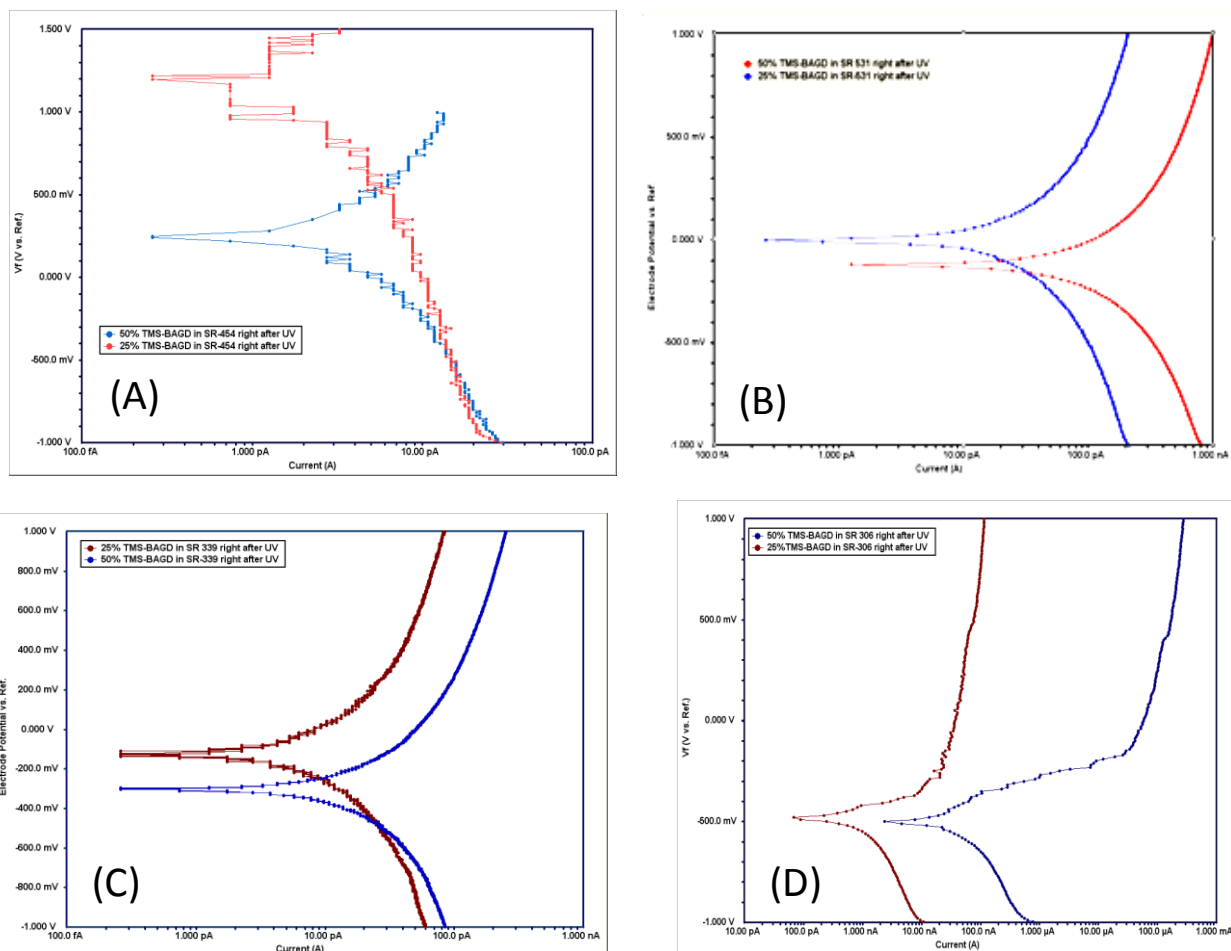
Figure 3.16. Results from potentiodynamic measurements made on coatings cast and cured over Al2024-T3. Coatings based on SR-454 (A), SR-531 (B), SR-339 (C), and SR-306 (D) as reactive diluents.

Table 3.2. Electrochemical characteristics derived from the potentiodynamic measurements.

Sample	I_{corr} (A/cm^2)	OCP (V)
25% TMS-BAGD in SR-454	1.00E-12	1.187
50% TMS-BAGD in SR-454	5.07E-12	0.266
25% TMS-BAGD in SR-531	2.15E-11	0.001
50% TMS-BAGD in SR-531	2.17E-10	-0.126
25% TMS-BAGD in SR-339	9.83E-11	0.124
50% TMS-BAGD in SR-339	3.26E-11	-0.312
25% TMS-BAGD in SR-306	1.12E-09	-0.473
50% TMS-BAGD in SR-306	1.49E-07	-0.501

The kinetics of the UV-cure process for coatings based on the two reactive diluents and TMS-BAGD were characterized using photo-DSC and confocal Raman spectroscopy. Figure 3.17 displays thermograms obtained with the photo-DSC. The thermograms displayed in Figure 17 show very rapid cure for all coatings. Upon UV-irradiation, a strong exotherm was observed and curing was complete in less than one minute. Figures 3.18 and 3.19 display Raman spectra for uncured and cured coatings. Curing was done using a conventional curing system comprised of an H-bulb and conveyor belt. The UV intensity and UV-A dose measured using a dosimeter was 1326 mW/cm^2 and 2230 mJ/cm^2, respectively. The extent of UV-cure can be seen by observing changes in bands at 1636 cm^{-1} and 1408 cm^{-1} which correspond to C=C stretching and =C-H in plane bending, respectively. As shown in Figures 18 and 19, UV exposure essentially completely consumed the acrylate double bonds. Since confocal Raman was used for the measurement, the depth-profile feature was used to determine degree of cure as a function of coating thickness. The band at 1459 cm^{-1}, which is due to methyl group vibrations, was used for normalization. The results of the depth-profile experiment are shown in Figure 3.20. For the coatings based on SR-454 as the reactive diluent, the extent of cure was quite high throughout the entire thickness of the coating. In contrast, the coatings based on SR-531 showed a significant reduction in the extent of cure from the coating-air interface to the coating-substrate interface. At present, the reduction in through-cure obtained with the use of SR-531 cannot be readily explained.
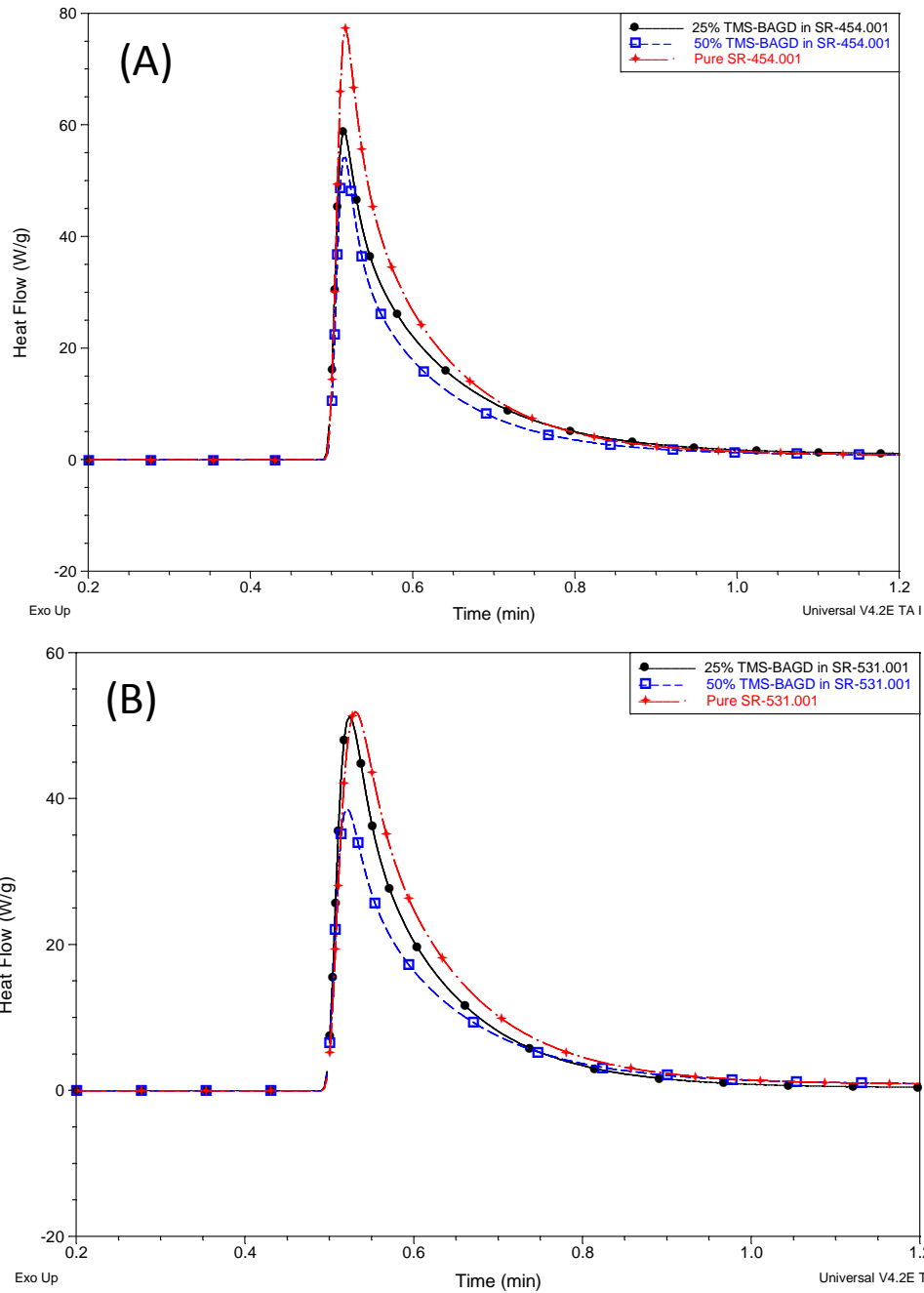
Figure 3.17. Thermograms obtained from photo-DSC. (A) Coatings based on SR-454 as the reactive diluent. (B) Coatings based on SR-531 as the reactive diluent.
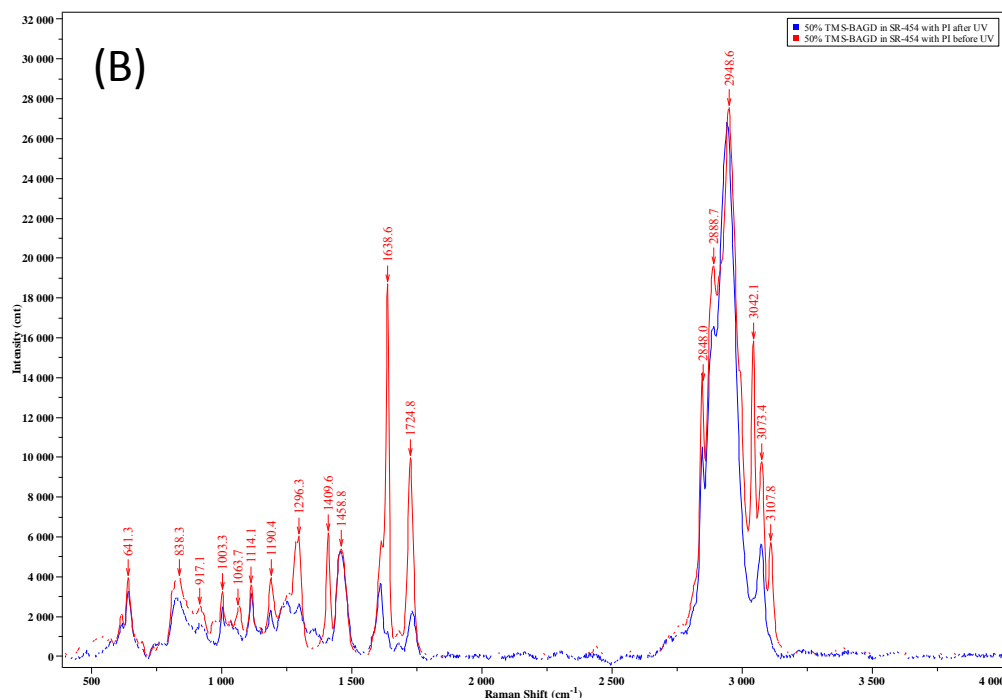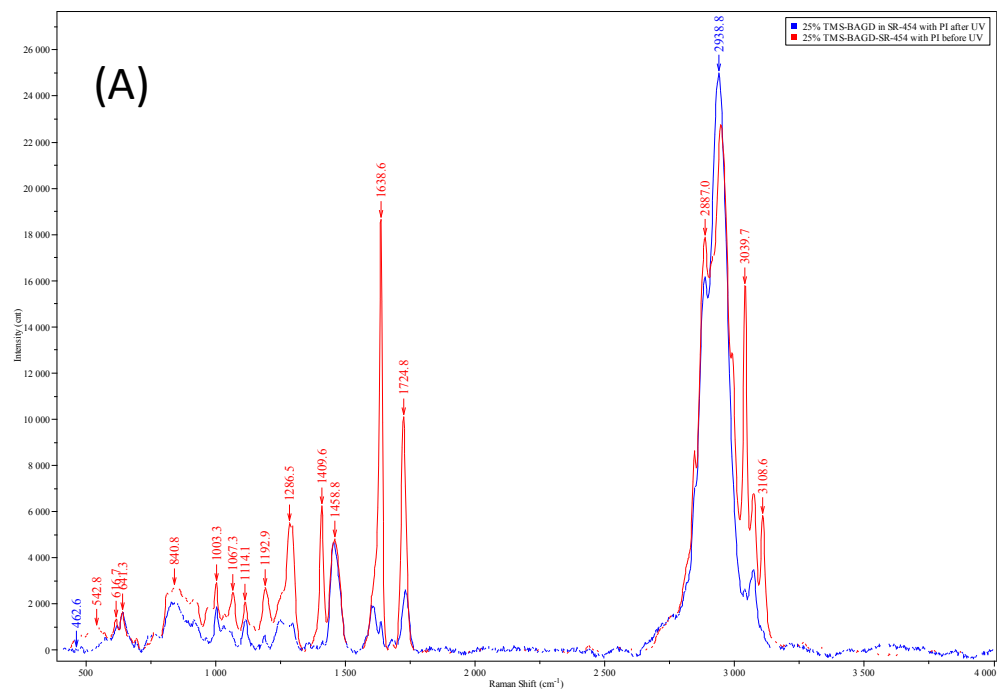
Figure 3.18. Raman spectra for uncured and cured coatings based on SR-454 as the reactive diluent. (A) Coatings based on 75 wt. % SR-454. (B) Coatings based on 50 wt. % SR-454.
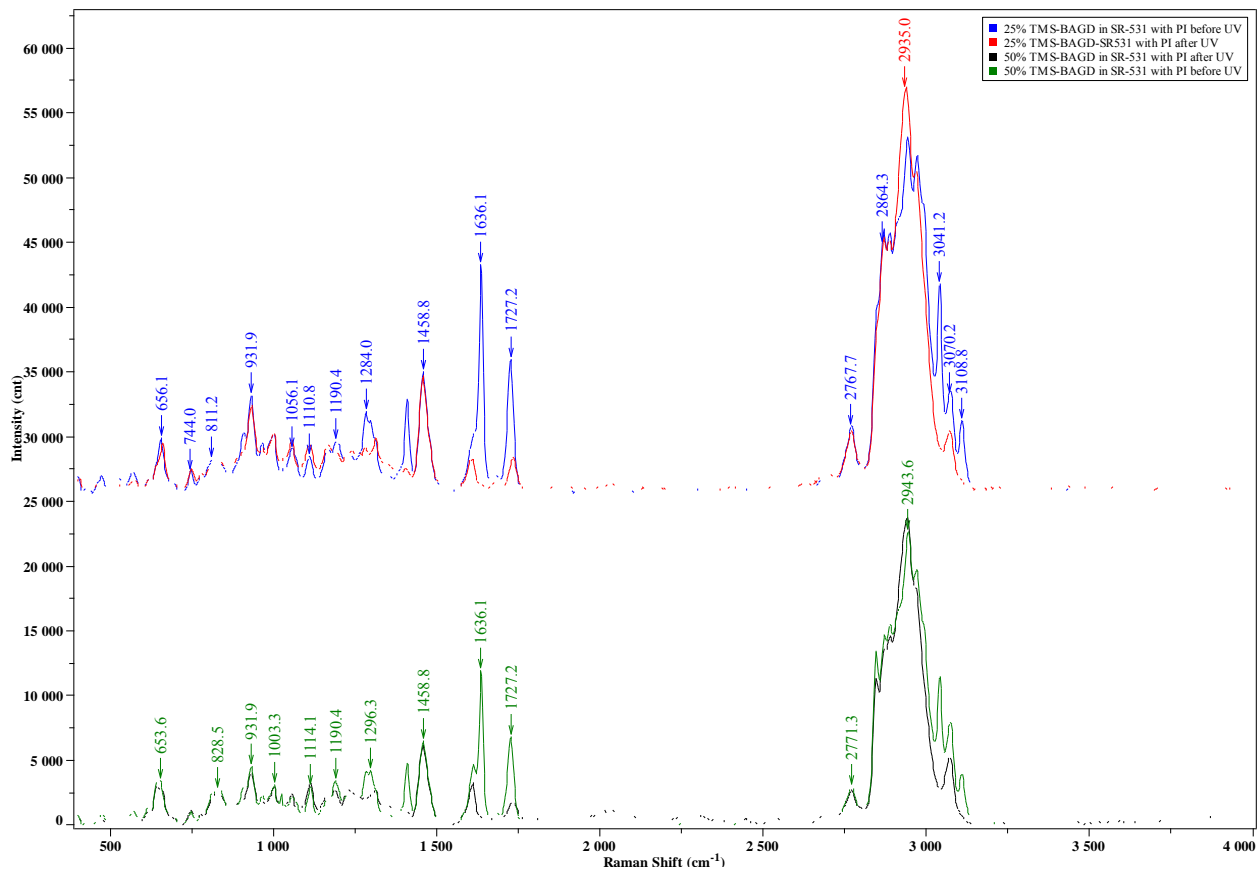
Figure 3.19. Raman spectra for uncured and cured coatings based on SR-531 as the reactive diluent.
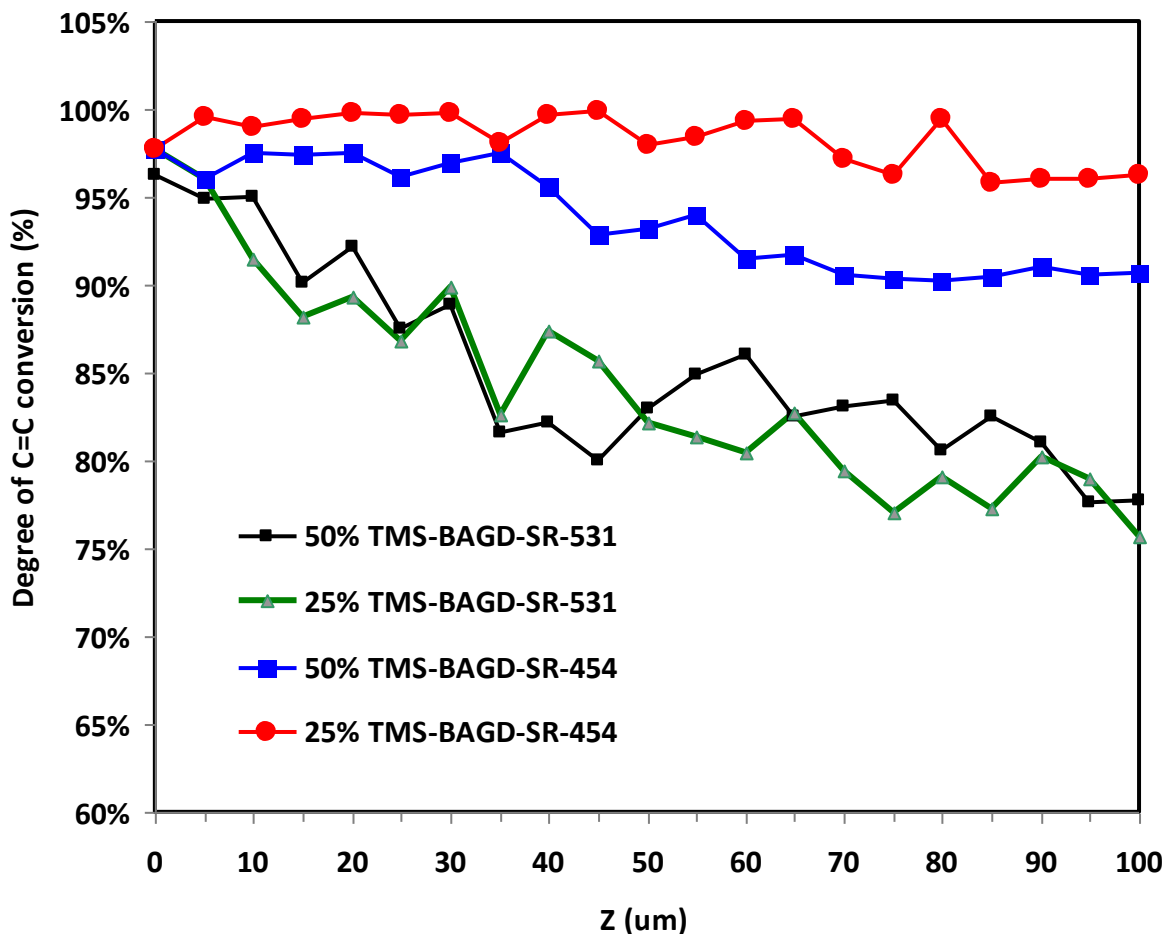
Figure 3.20. Data obtained from depth-profiling experiments conducted with confocal Raman spectroscopy.

The glass transition temperature (Tg) of the cured coatings was measured using DSC. As shown in Figure 3.21, the Tg of the polymer produced by photopolymerization of SR-531 possessed a Tg of 19 $^{\circ}$C and the crosslinked coatings based on 25 and 50 wt. % TMS-BAGD possessed Tgs of 22 and 43 $^{\circ}$C, respectively. In contrast, photopolymerization of the triacrylate, SR-454, produced a highly crosslinked network that did not exhibit a readily observable Tg by DSC over the temperature range of -40 $^{\circ}$C to 200 $^{\circ}$C. This result indicates that the high crosslink density associated with the high acrylate functionality produces a polymer network with a Tg above 200 $^{\circ}$C or perhaps even above the decomposition temperature. Similarly, the SR-454-based coatings containing TMS-BAGD also lacked a readily observable Tg over the temperature range probed.
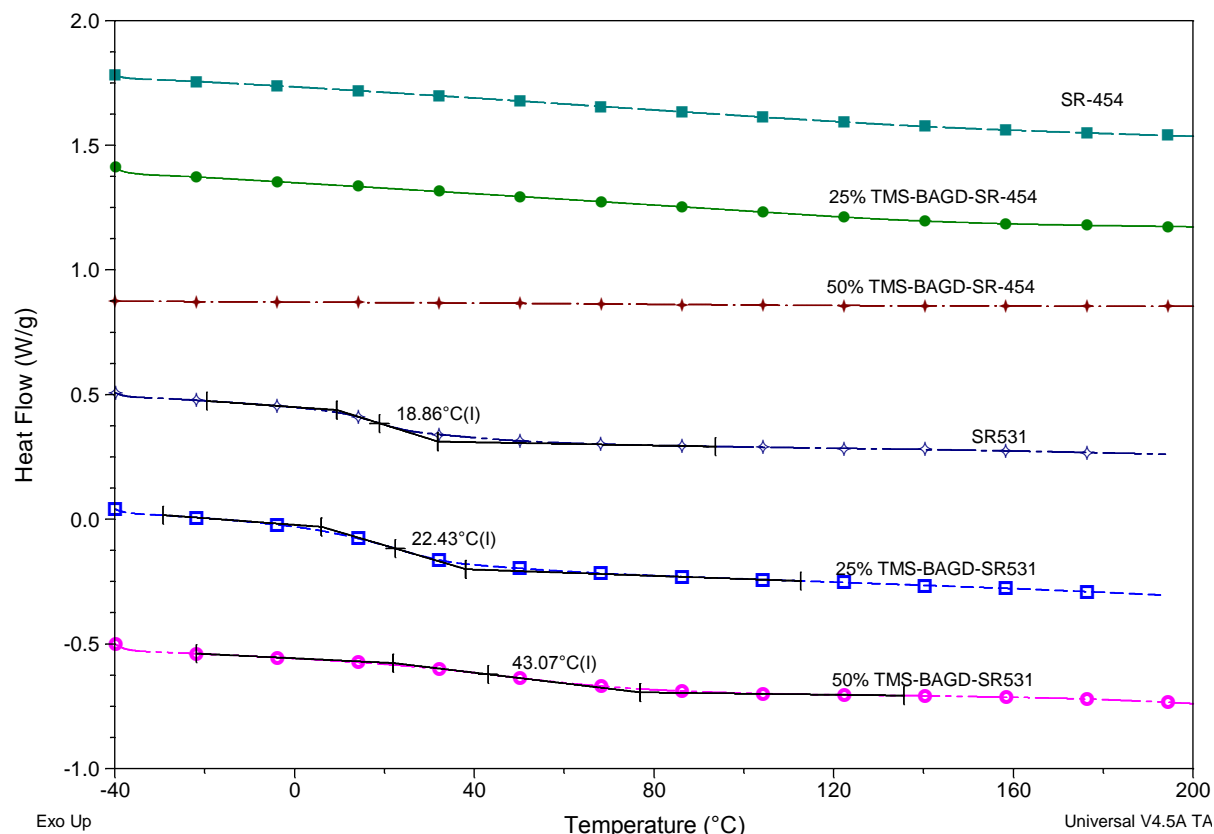
Figure 3.21. DSC thermograms obtained for cured coatings based on TMS-BAGD and a reactive diluent.

In the work published as part of the *FutureCoat* proceeding and described in last years annual report, FT-IR was used to characterize the development of the siloxane network by monitoring the Si-O-Si band at 454 cm^{-1}. This previous research was focused on coatings comprised of pure TMS-BAGD. For the coatings currently of interest which contain a reactive diluent, the band at 454 cm^{-1} was not observed. The lack of a band at 454 cm^{-1} suggests that the concentration of Si-OCH$_3$ groups may be too low to enable enough Si-O-Si groups to be formed to be detected by FT-IR.

The barrier properties of coatings containing 50 wt. % reactive diluent were determined as a function of exposure time to an electrolyte solution using electrochemical impedance spectroscopy. As shown in Figure 3.22, the low frequency impedance (0.01 Hz) of the 50/50 TMS-BAGD/SR-531 coating increased with increasing exposure time by an order of magnitude over a 5 week period. The only plausible explanation for this behavior is that time and the egress of water into the coating resulted in the continued formation of the siloxane network resulting in an overall higher crosslink density and enhanced barrier properties. As shown in Figure 3.22, the behavior of the 50/50 TMS-BAGD/SR-454 coating was somewhat different than that of 50/50 TMS-BAGD/SR-531. In the first two weeks of electrolyte exposure, the low frequency impedance dropped more than one order of magnitude and then impedance increased with longer exposure. The difference in behavior observed with SR-454 as the reactive diluent as compared to SR-531 may be due to differences in the crosslink density of the UV-cured network. The higher acrylate functionality of SR-454 produces a higher crosslink density that reduces diffusion both of molecules such as water through the coating as well as the diffusion of reactive moieties such as SiOCH$_3$ and SiOH groups. Thus, the initial reduction in low frequency impedance followed by an increase may be due to the slower rate of the siloxane network formation resulting from lower diffusion associated with the higher crosslink density of the UV-cured network.
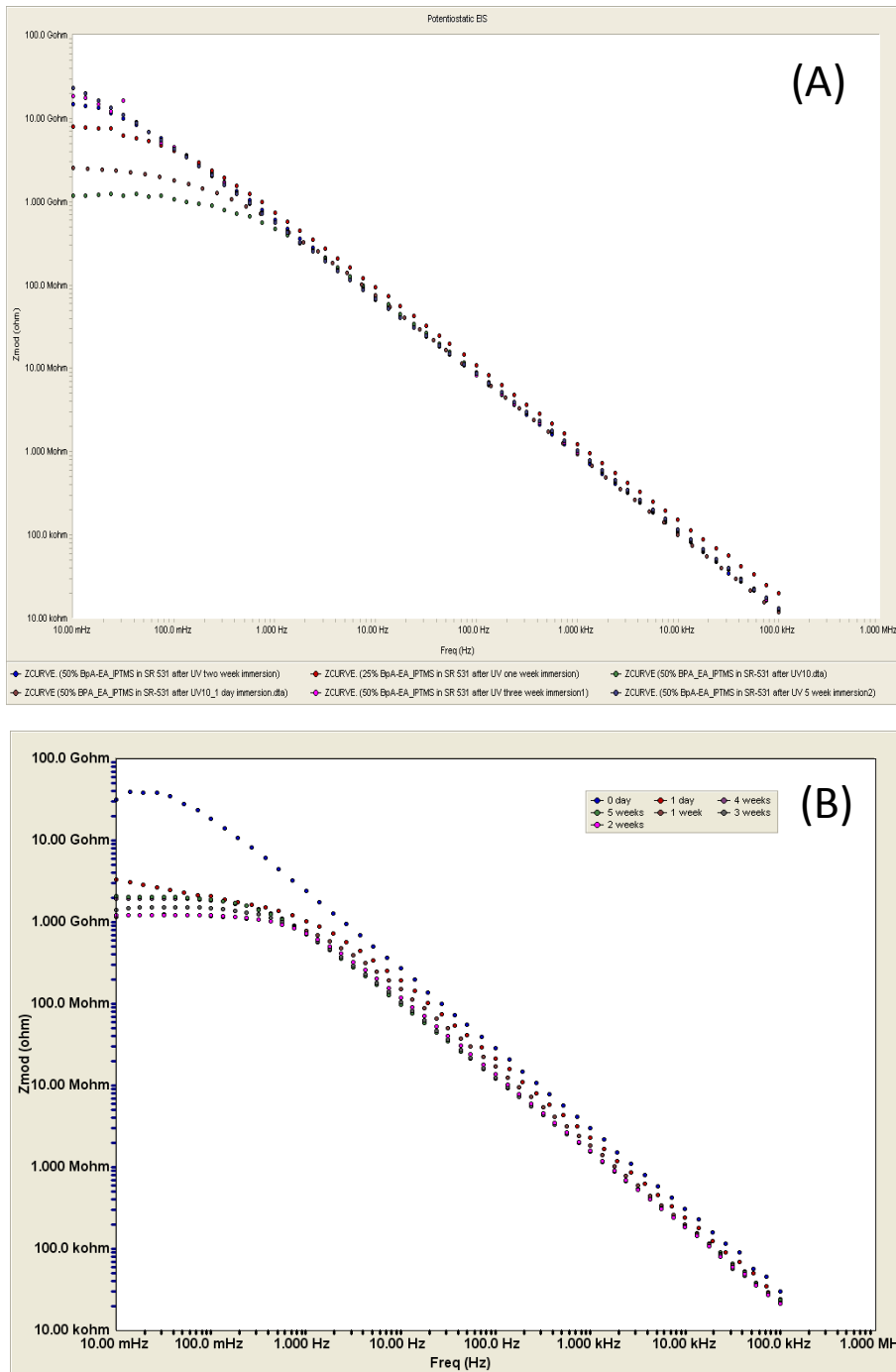
Figure 3.22. Bode plots produced as a function of electrolyte (3% NaCl) exposure time for 50/50 TMS-BAGD/SR-531 (A) and 50/50 TMS-BAGD/SR-454 (B).

To further test the hypothesis that the increase in impedance observed during electrolyte exposure was due to the development of the siloxane network, DSC was conducted on coating specimens exposed to electrolyte solution for 5 weeks. As shown in Figure 3.23, the Tg for the 50/50 TMS-BAGD/SR-531 after 5 weeks was 73 °C which is almost 30 °C higher than that obtained for coating before exposure to

electrolyte (see Figure 3.21). Similarly, the Tg for the 25/75 TMS-BAGD/SR-531 coating increased by 29 °C as a result of five weeks electrolyte exposure. Since coatings based on SR-454 did not show a Tg below the decomposition temperature, the same analysis could not be done for these coatings.
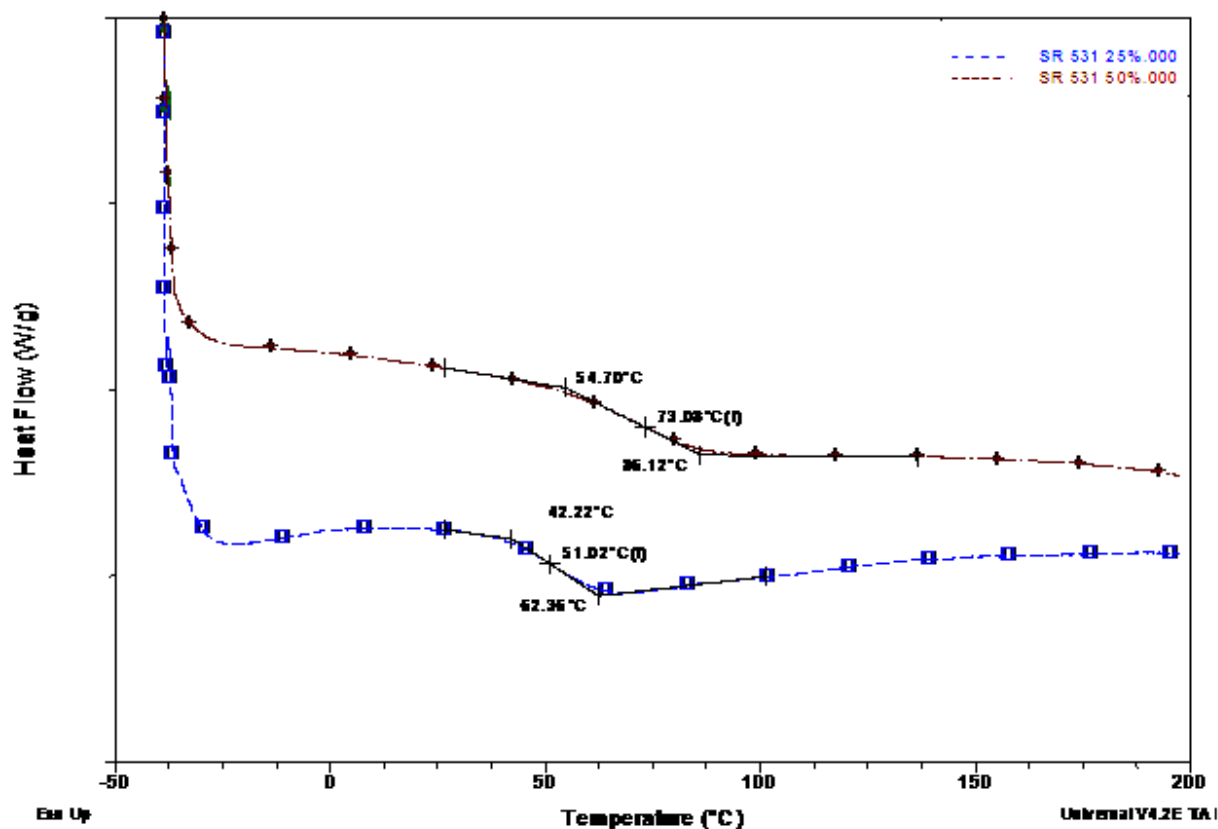
Figure 3.23. DSC thermograms obtained from coating specimens exposed to electrolyte solution for 5 weeks.

To characterize the development of the siloxane network with time at ambient conditions, nanoindentation was done as a function of time after UV-curing. As shown in Figure 3.24, just after UV-curing, the Young's modulus of the coatings based on SR-454 as the reactive diluent was higher than for the coatings based on SR-531. This result is consistent the higher crosslink density achievable with UV-curing of the trifunctional acrylate, SR-454. For all four coatings, Young's modulus increased with time at ambient conditions which can be attributed to the gradual development of the siloxane network. For a given reactive diluent, the Young's modulus at any time beyond 3 days was higher for the coating containing the higher level of TMS-BAGD. This result is consistent with the gradual development of the siloxane network with time. For the two coatings based on SR-454 as the reactive diluent, Young's modulus increased over a period of approximately 20 days then remained constant. In contrast, the two coatings based on SR-531 as the reactive diluent showed a continuous increase in Young's modulus over the entire 60 day period and the magnitude of the Young's modulus at 60 days was higher than that obtained for the analogous coatings based on SR-454. These trends can potentially be explained by considering the differences in crosslink density associated with the UV-cure process. As discussed previously, SR-454 is a triacrylate and thus produces a highly crosslinked network upon UV-curing. The high crosslink density restricts molecular mobility and diffusion. Thus, the plateau in Young's modulus

as a function of time at ambient conditions observed for SR-454-containing coatings maybe due to diffusion and molecular mobility restrictions that prevent further development of the siloxane network at ambient temperature. In contrast, the lower crosslink density and lower Tg of the UV-cured network associated with the use of the monoacrylate, SR-531, as the reactive diluent provides for higher extents of siloxane network formation and ultimately a higher overall crosslink density and Young's modulus.
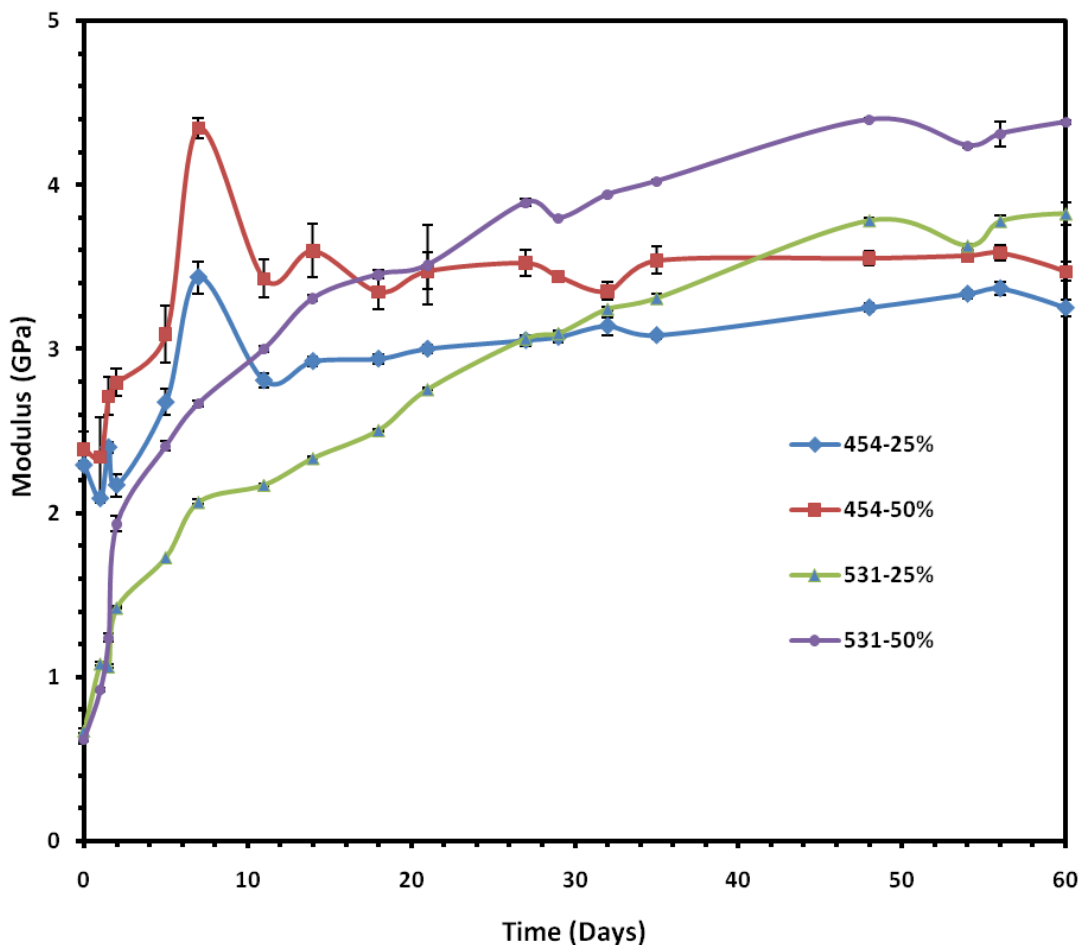
Figure 3.24. Young's modulus as a function of time at ambient conditions.

Based on the results obtained from this dual-cure binder work, the 50/50 TMS-BAGD/SR-531 and 50/50 TMS-BAGD/SR-454 systems are currently be used to produce Mg-rich primers and the properties of the coatings will be characterized.

References for Section 3

1.   Bret J. Chisholm, Missy Berry, James Bahr, Jie He, Jun Li, Seva Balbyshev, and Gordon P. Bierwagen, "Combinatorial materials research applied to the development of new surface coatings XI: a workflow for the development of hybrid organic–inorganic coatings," *J. Coat. Technol. Res.*, published on-line (DOI 10.1007/s11998-009-9163-7)2009.

2.   Jie He, Bret Chisholm, David Christianson, and Crystal Rafferty, *FutureCoat 2008 Proceedings*, 2008.

4.0 Plasma Deposition of Inorganic Coatings

The application of plasmas toward thin film growth offers advantages such as denser deposits as well as growth of targeted phases at lower temperature given the additional enthalpy introduced into the system from the activated molecules.

Two different applications were evaluated for use in AFRL-relevant systems. The first related to a permanent pretreatment for aluminum that would be compatible with the NDSU Mg-rich primer (Task 2). This work has been completed and reported in the previous annual report for this project. The second relates to a conductive and transparent coating that would serve as an in-field repair system for damaged polycarbonate aircraft canopies (Task 4; Section 4.1).

4.1 Deposition of Transparent Conductive Indium and Tin Oxides by Atmospheric Pressure Plasma Jet

Transparent conducting oxides (TCOs) are broadly applied in various field that includes, photovoltaic, flat panel displays and many other electronic applications. TCOs have conventionally been deposited using expensive vacuum-based process at moderate temperature, which imposes limits in using inexpensive polymer substrate materials (e.g., Mylar) in a roll-to-roll manufacturing process. The aim of this project is to deposit a TCO coating which possesses good conductivity and transparency using an atmospheric-pressure plasma route. Thus prepared TCO coatings can be potentially used to repair aircraft canopies where a transparent conducting surface reduces the buildup of static charge. At present, damaged canopies are repaired with conductive epoxy or replaced completely. Because epoxy repairs result in occluded pilot visibility, they are only appropriate for limited area of the canopy. Replacement of damaged canopies results in the need to maintain inventory of expensive, bulky components at airbases around the world, an expensive and logistically challenging task. The current objective was to identify suitable metal beta-diketonate complexes for indium and tin, to realize ITO coatings, and to deposit highly conductive ITC coatings.

Efforts during the past year related to screening metal beta-diketonate complexes as precursors to both indium oxide and tin oxide thin films. For InO_x films, $In(acac)_3$ was shown to yield good films using our atmospheric pressure plasma deposition (APP) system. The results of this screening study were reported at the 2008 International Conference on Metallurgical Coatings and Thin Films (ICMCTF) and are the subject of an article in Surface and Coatings Technology published in the same year.

Two tin (II) beta-diketonate complexes were screened this year and it was found that $Sn(hexafluoroacetylacetonate)_2$ ($Sn(hfa)_2$) has a very sharp temperature range, where the complex is volatized rendering this material as a non-ideal precursor with undesirable vapor pressure vs. time relations. Toward this end, very little flux was noted in the carrier gas stream until a particular critical temperature was reached. While heating to a sufficiently high temperature did result in sublimation, the temperature difference between minimial precursor flux and an overwhelming amount of precursor in the gas stream was less than 10 degrees. Thus, efforts to utilize $Sn(hfa)_2$ as a precursor were abandoned given the engineering challenges associated with maintaining such tight temperature control.

It was determined that $Sn(trifluoroacetylacetonate)_2$ ($Sn(tfa)_2$) possesses atmospheric-pressure sublimation characteristics that afford good materials transport. Details for the synthesis and deposition of $Sn(tfa)_2$ are given in a recent publication,[1] also given in Appendix A. In brief, $Sn(tfa)_2$ was synthesized in-house and was twice sublimed prior to experimentation. The results of the proof-of-concept study for $Sn(tfa)_2$ was the subject of a oral presentation in Materials Research Society Presentation at the Fall 2008 held in Boston.

The APP system was reconfigured to allow the use of two solid-source precursors simultaneously. Initially, the growth conditions for InO and SnO were separately optimized and then In-Sn-O (ITO) coatings were prepared using two solid precursor sources. Table 4.1 summarizes the results obtained from thus synthesized ITO coatings using two precursors. Microstructural studies on these coatings were carried out using XRD and all coatings were x-ray amorphous. The chemical composition of a small number of samples by X-ray fluoresence spectroscopy showed indium, tin and oxygen in addition a large amount of carbon in these films. It appears possible that the carbon might act as an impurity and limit the conductivity in these samples. These results were presented in Society of Vacuum Coaters meet held in Santa Clara, CA during 12 May 2009.

Table 4.1. Properties of ITO coatings deposited using APP system.

Sample	Thickness (nm)	Sheet resistance ($\Omega/\square$)	P (Ω cm)	Carrier concentration (cm^{-3})	Carrier mobility ($cm^2 V^{-1} sec^{-1}$)	Band gap (eV)
ITO #5	95	$1.7x\ 10^3$	$1.7x10^{-2}$	--	--	3.6
ITO #8	46	1.6×10^3	$7.6x10^{-3}$	1.2×10^{20}	7.33	3.83
ITO #9	118	9.9×10^3	$7.3x10^{-3}$	5.5×10^{19}	9.7	3.8
#11 (sputter)	38	$3.8x10^3$	$1.2x10^{-2}$	$2.12x10^{20}$	2.07	3.33
CC1*	129	$1.2x10^2$	$3.6x10^{-4}$	2.8×10^{21}	8.5	3.64

In-situ electrical resistance studies were carried during the heating and cooling of ITO coatings in oxygen and H_2/N_2 ambients. It was observed that a reducing atmosphere (i.e., H_2/N_2) gave decreased resistivities and that such thermal treatment causes the films to transform from amorphous to crystalline where (222)-textured coatings with a grain size of 18 nm were observed.

The experiments supported by AFRL have demonstrated the ability of forming transparent conducting oxide coatings with reasonable proporties using atmospheric-pressure plasma deposition. However, the current Surfx[TM] plasma source has a showerhead configuration which complicates the deposition of coatings with uniform film thickness. Although no longer supported by AFRL, future efforts in this area of research shall pursue the design of a linear plasma source that can operate at atmospheric pressure and deposit functional coatings in roll-to-roll fashion.

References for Section 4.

1. Johnson, K.W.; Jha, S.; Braun, C.; Anderson, K.; Halverson, B.; Pokhodnya, K.; Guruvenket, S.; Sailer, R.A.; Schulz, D.L. Atmospheric Pressure Plasma Deposition of Transparent Conductors – Tailoring Precursor Chemistries, *Soc. Vac. Coaters*, **2009**, 37-42.

2. Sailer, R.A.; Wagner, A.; Schmit, C.; Klaverkamp, N.; Schulz, D.L. Transparent Conductive Indium Oxide by Atmospheric-Pressure Plasma Deposition, *Surf. Coat. Tech.*, **2008**, *203*, 835-838. [Note: submitted during previous period of performance but is now published.]

Recent Presentations

Johnson, K.W; Jha, S.; Guruvenket, S.; Sailer, R.A.; Schulz, D.L. "Synthesis of TCOs at atmospheric pressure, ND EPSCoR 2009 State Conference, September 24th, at NDSU, Fargo.

Johnson, K.W; Guruvenket, S; Jha, S; Sailer, R.A.; Schulz, D.L. "Atmospheric Pressure Plasma Deposition of Transparent Conductors – Tailoring Precursor Chemistries", 52nd Annual SVC Technical Conference & Exhibit, Santa Clara, CA, May 12, 2009.

Sailer, R.A.; Jha, S.S.; Johnson, K.W.; Schulz, D.L., "Indium Tin Oxide Films by Atmospheric Pressure Plasma" talk B10.9 at the 2008 Fall Materials Research Society meeting, Dec 4, 2008, Boston, MA.

5.0 Coating Prognostics

In this task, NDSU investigated the application of embedded electrochemical sensors for magnesium-rich primers. Unlike conventional electrochemical sensors that monitor the metal substrate itself and provide no information about the coating, the NDSU *in situ* corrosion sensors are embedded between the primer and the topcoat and thus are suitable for monitoring the corrosion protection afforded by the metal-rich primer. As an added advantage, the embedded sensor electrodes are shielded from the environment by the topcoat, which prolongs the electrode life as well as reduces the noise associated with measurements. Moreover, electrochemical measurements of the primer and primer/metal interface can be carried out without being masked by high resistant topcoats.

5.1 Embedded Sensor Electrode Arrays

The newly-developed embedded sensor electrode is part of the effort aimed at development of wireless corrosion sensors for monitoring cathodic protection of metal-rich primers. Such electrode is robust and reproducible, while at the same being thin, flexible, and adaptable to various field applications. Sensor electrodes of a new design were made by the industry standard selective laser etching procedure utilized by many common printed circuit board manufacturers.The shape and size of the sensor can be easily changed by creating the appropriate shadow mask for metal deposition.

First, sensor design concept was translated into a CAD drawing using Design Capture/Expedition by Mentor Graphics (Mentor Graphics, Wilsonville, OR). Sensor design took into consideration the embedded aspect of the corrosion sensor. Instead of making a sensor into a simple (rectangular or circular) planar shape, a provision for ingress of electrolyte was made in the form of conducting 'fingers' separated by gaps of varying widths allowing for electrolyte to penetrate into the primer. Initially, the widths of the fingers and spacings between them ranged from 250 µm to 2000 µm, resulting in nine different finger/spacing configurations. Sensor design is shown in Figure 5.1 shows two sensors with different finger-spacing dimensions.

In the next step, the inverted image of the sensor generated by CAD software was used to manufacture a shadow mask (stencil) for subsequent physical vapor deposition of metallic film (conductive path of a sensor). The stencils were made from series 316 stainless steel by Great Lakes Engineering (Maple Grove, MN). Initially, nine variations of stencils with varying finger and spacing widths were manufactured. The deposition step was performed at NDSU CNSE on a CMS-18 PVD sputtering sustem (Kurt J. Lesker Company, Clairton, PA). For better adhesion, a 50 Å layer of Cr (99.95% pure, from Kurt J. Lesker Company, Clairton, PA) was first vapor deposited on a 2 mil think Kapton® film (obtained from McMaster-Carr, Robbinsville, NJ), followed by the deposition of 1500 Å layer of Pt (99.99% from Equipment Support Company USA Inc., Pensacola, FL). The sensors are not limited to the use of platinum or other expensive metals. However, selection of materials for the conductive aspect of the sensor must conform to the requirements of a particular application. The use of platinum in this design was dictated by its superior conductivity at nanometer thicknesses and by the available of experimental electrochemical data for embedded sensors for Mg-rich primers.

Figure 5.1. Sensor geometry and dimensions.

Following the deposition, the Kapton® pieces, 15 cm in diameter each, were transferred to the Optec MicroMaster laser ablation station (Z.A.E. Le Crachet, Frameries, Belgium) where the spacings between the fingers were cut out by the laser. During the laser ablation step, it was discovered that sensor arrays with closely spaced narrow fingers were difficult to ablate, and frequent laser cutting generated too much debris. In order to streamline the manufacturing process and reduce the duration of the laser ablation step, two sensor electrode geometries were selected for testing: 1 mm thick fingers spaced at 0.5 mm and 1 mm, as shown in Figure 5.1.

After the ablation step, excess Kapton® around the conductors was removed, and the arrays were cleaned by ionized oxygen in March Plasma Treatment System (March Plasma Systems, Concord, CA), rubbed in IPA, and immersed in an ultrasonic bath. ExcessThe resulting sensor arrays are shown in Figure 5.2. Each sensor array is composed of a pair of individual sensors.
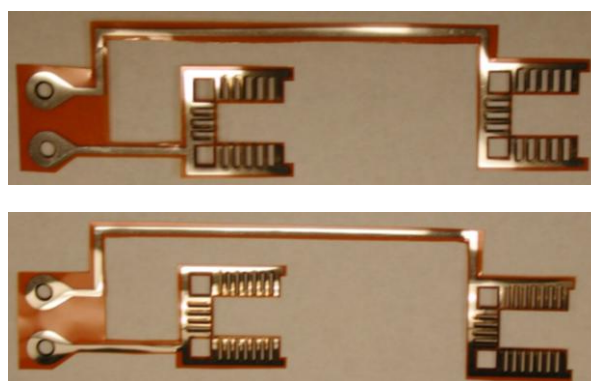
Figure 5.2. Sensor arrays before application.

In order to investigate the feasibility of the new sensor electrode array, series of electrochemical tests were performed on the embedded sensor of the previous and the new designs. The layout of the sensors in an array is shown in Figure 5.3.
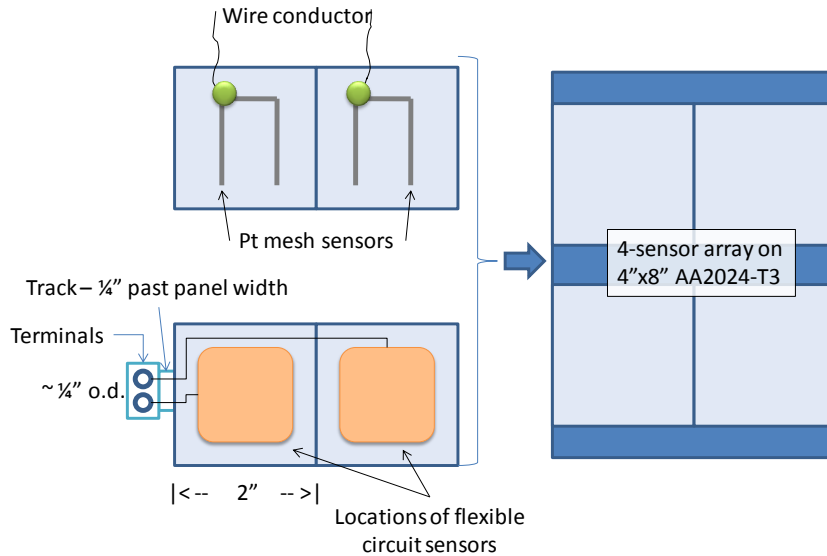
Figure 5.3. Sensor layout on a coated AA2024-T3 substrate.

Here, a metal substrate, 4" x 8" in size, accommodates four individual sensors of only one particular design. The connection to the Pt mesh sensors developed by NDSU and described further in Section 5.2 was carried out by insulated copper wire. Whereas the electrical connection to a sensor of the new design was made by clipping an instrument lead to a metal screw (post) connected to the terminal pad, as shown in Figure 5.3.

The Pt-mesh sensors were affixed to the primer by a drop of epoxy adhesive, whereas the Kapton-supported sensor were laid down flat on the primer following the initial solvent flash-off within seconds of application of Mg-rich primer. Figure 5.4 shows the 4-sensor array of the new design before the topcoat application.
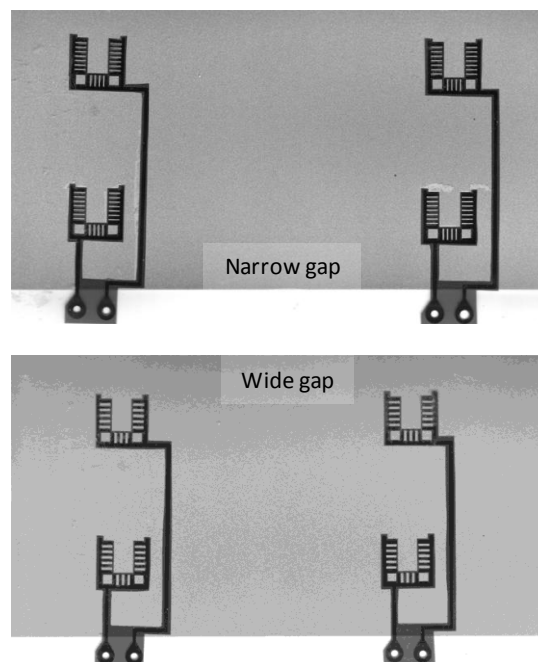
Figure 5.4. Sensors after application on top of Mg-rich primer.

After the topcoat application, two area of interested were identified on the surface of the coated specimen, as shown in Figure 5.5 (a). One area was scribed using the Gravostar Engraving Machine (Gravostar, Chillicothe, OH), while the other remain unaltered.
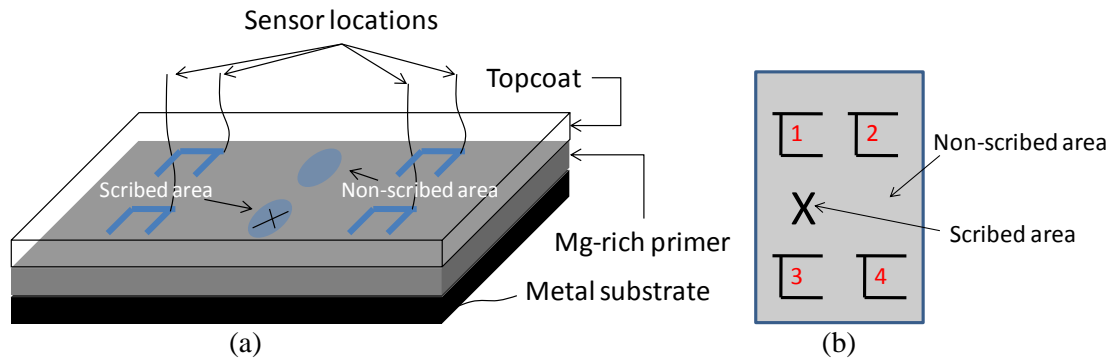
Figure 5.5. Experimental setup for EIS and ENM measurements and sensor identification.

Electrochemical impedance spectroscopy (EIS) and electrochemical noise methods (ENM) were conducted with various combinations of individual sensors in 4-electrode arrays, both in 3- and 2-electrode configurations. The scribed and unscribed areas were exposed to dilute Harrison's solution (0.35% $(NH_4)_2SO_4$, 0.05% NaCl) by virtue of clamping a glass cell with an o-ring over the corresponding spot, resulting in a total exposure area of 6.45 cm^2. Initial EIS and ENM results demonstrate that *in situ* monitoring could be performed with the embedded sensors of the new design under constant immersion conditions. The two-electrode EIS configuration is suitable for tracking changes in open circuit potential. Electrochemical signal detected by the sensors tracks the response from the entire test specimen rather than localized areas of interest. However, this appears to be a limitation inherent to electrochemical impedance spectroscopy in general.

For more details on the above experiments, refer to Appendix B "Embedded sensor electrode arrays for real time monitoring of an Air Force topcoat/Mg-rich primer systems." This paper is to be presented at the NACE Conference in San Antonio, TX in January 2010.

5.2 Wireless EIS Coating Evaluation Sensor

5.2.1 Sensor Node Design

There are two approaches to the sensor node design. One approach uses off-the-shelf impedance measurement chip (AD5933) with a microprocessor. The impedance of the coating system can be accurate measured with the AD5933. The other approach uses a simple voltage division method to track impedance change. In both approaches, the impedance variation can be measured for coating evaluation purposes. For the purposes of this report, the AD5933 design will be further referred to as SN1 (sensor node 1), while the other design will be addressed as SN2.

Sensor Node with Impedance Measurement Chip

In this approach, the SN1 consists of two main parts as shown in Figure 5.: a commercial impedance measurement chip, AD5933, and a microprocessor. The AD5933 is a two-electrode impedance measurement system, with a large impedance measurement range. According to the datasheet, AD5933 is

capable of measuring impedance ranging from 1kΩ - 1MΩ. The control circuit of the AD5933 is implemented by a microprocessor, uPD78F. The reason to choose uPD78F is the processor has a wireless interface for later function expansion to build a large wireless sensor network.
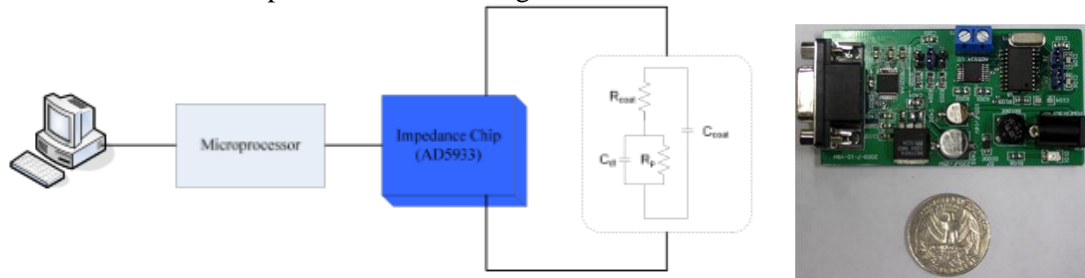
Figure 5.6. Sensor node diagram with microprocessor and impedance measurement chip.

The designed sensor node was integrated on a printed circuit board (PCB) as shown in Figure 5. on the right. The sensor node has not been fully tested at this point. However, the measurement results with fixed resistors and capacitors prove that the AD5933 can perform the stated measurement after appropriate calibration. The ongoing research is focused on addressing the calibration of the AD5933 and one interfacing the sensor node with a wireless sensor network. The board size can be further reduced by 50% when the computer interface is replaces with wireless network.

Sensor Node with Voltage Division Device

In this approach, the SN2 design uses a very simple voltage division method, as shown in Figure 5 on the left. The signal generator produces a frequency sweep. The frequency multiplier shifts the frequencies down into the hertz range, or up into the 100 kHz range. The signal is then divided between the reference resistor and the coating sample. The voltage division is converted to a digital number by using an analog-to-digital convert (ADC). The ADC results reflect the relative impedance of the coating sample to that of the reference resister. The entire measurement is overseen by a control circuit, which also controls the wireless data transmission. Part of the testing result has been prepared as a journal paper to be submitted to Journal of Coating Technology. The manuscript, entitled "A New Technique for Electrochemical Impedance Spectroscopy-based Coating Evaluation," attached as Appendix C.

Figure 5 (right) shows the size of a PCB version sensor node as part of the preliminary research. The controller of the sensor node is replaced by a microprocessor on the PCB. The prototype consumes 250 mW of power with wireless capability.
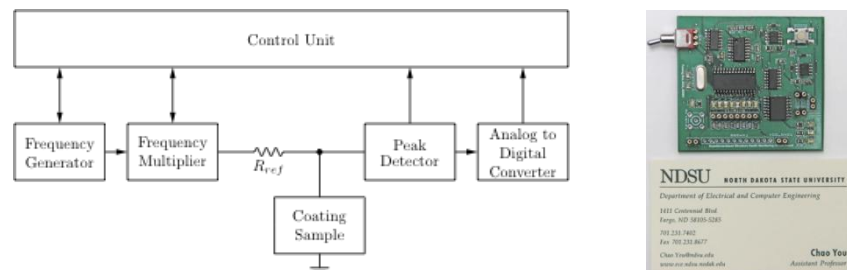
Figure 5.7. Circuit diagram and PCB version of the sensor node.

To prove the proposed circuit has the testing capability equivalent to the widely used EIS equipment, the PCB has been used in coating evaluation on three different coating samples. They are epoxy primer with an Akzo Nobel Aerospace Coating (ANAC) topcoat, Mg-rich primer, and Mg-rich primer with ANAC topcoat.

Figure 5. shows the EIS results of the PCB prototype for the epoxy primer with ANAC topcoat. The results are comparable with the EIS result of the same sample. As indicated by both testing results, 50% impedance drop of the coating is considered an indication of full degradation of the coating system. A threshold can be set to 50% for 25 kHz impedance measurements.

Figure 5. and Figure 5. show the EIS spectra comparisons for other coating systems. The selection of the frequency range is between 25 kHz to 80 kHz. That frequency can be further reduced down to the kilo-herz range if required. The current frequency range was selected for a proof of concept and for the short time required to perform coating evaluation test. The current system works extremely well producing a "good / bad" decision for a particular coating system. The time required for such evaluation is less than 10 seconds and is based on one frequency sweep.
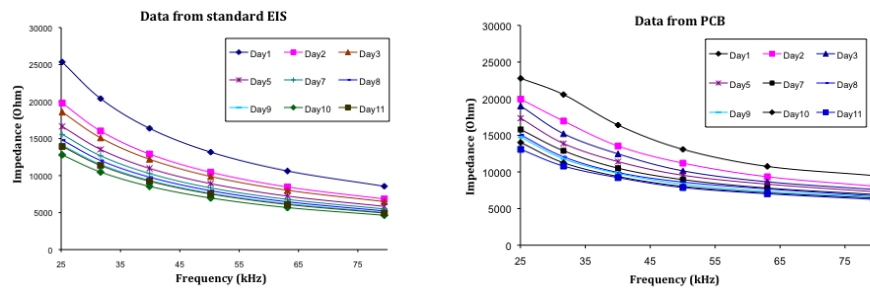
Figure 5.8. EIS and PCB prototype results for epoxy primer and topcoat.
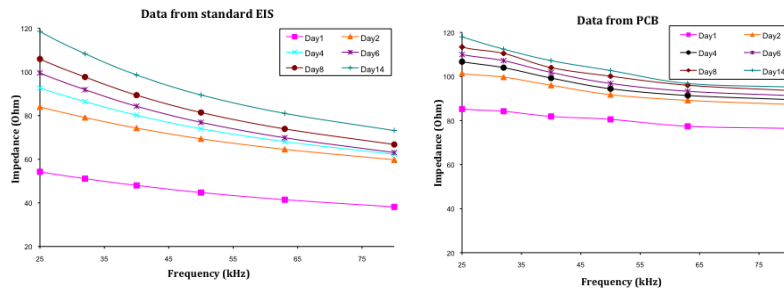
Figure 5.9. EIS and PCB prototype results for Mg-rich primer.
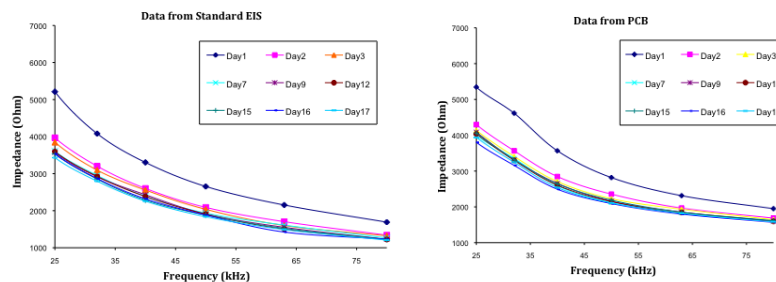
Figure 5.10. EIS and PCB prototype results for Mg-rich primer and topcoat.

5.2.2 Sensor Node Design Comparison

Both sensor node designs have the potential to be deployed widely for coating evaluation. The SN1 design costs higher due to the AD5933 chip. However, the SN1 design can provide more accurate results

if detailed impedance information is needed. The SN2 design is much simpler. The circuit can be integrated on a single silicon chip and suitable for large area coating evaluation. The SN2 design is an ideal candidate if a "good / bad" decision is desired in a coating evaluation.

5.3 Embedded Sensor Approach for Monitoring Cathodic Protections of AA2024-T3 by a Mg-Rich Primer

The magnesium pigments provide cathodic protection for the less active aluminum substrates and also provide a barrier type protection as the products from the Mg dissolution insulate the substrate from the environment. Their cathodic protection is comparable to Zn-rich primers for steel substrates. The time dependent electrochemical behavior of a Mg-rich primer and a topcoat/primer system on AA2024-T3 was monitored using EIS experimentation.

The time dependent electrochemical behavior of a Mg-rich primer and a topcoat/primer system on AA2024-T3 was monitored using EIS experimentation. The open circuit potential (E_{oc}) values monitored over time for both systems indicated the change from a mixed potential value to a value consistent with the substrate. This demonstrated the loss of the cathodic protection. The topcoat extended the time of cathodic protection of the primer. Conventional monitoring of cathodic protection for active pigment coatings is by E_{oc} monitoring, which is not a practical for field monitoring. EIS data associated with the primer and topcoat/primer systems were analyzed using a 12-element Voigt model. The resistance value associated with the largest time constant tracked the loss of cathodic protection of both systems better than the low frequency modulus parameter. The approach of using an embedded sensor for tracking cathodic protection presented here is being developed for the field monitoring of Mg-rich primers beneath topcoats.

For more detailed explanation of the above experiment, refer to the paper published in *Proceedings of 7th International Corrosion Congress, October 6-10, 2008, Las Vegas, NV*. It is included as Appendix D, "Cathodic Protection of AA 2024-T3 by a Mg-Rich Primer."

5.4 *In Situ* Monitoring of A Mg-Rich Primer Beneath a Topcoat Exposed to Prohesion Conditions

Mg-rich primers have been proven to be an adequate alternative for chromate-based coatings [Nanna, 2004] for the protection of aluminum alloys from corrosion. Its protection behavior was attributed to a combination of cathodic and barrier protection [Battocchi 2006 (1 and 2)], similar to the protection behavior associate with Zn-rich primers on steel substrates.

The performance of a Mg-rich primer on aluminum 2024-T3 under Prohesion® exposure (ASTM G85) has been monitored using an embedded sensor placed at the surface of the primer and below the topcoat. This accelerated weathering cycle is an alternative of wet and dry cycles to simulate outdoor weather exposure.

Electrochemical impedance spectroscopy (EIS) and electrochemical noise methods (ENM) experiments were conducted to monitor the performances and the electrochemical properties of the system beneath the topcoat. The data analysis demonstrates that the sensor is able to detect change in the barrier property of the topcoat in response to the exposure conditions and the activation of the active pigments in the primer in presence of the electrolyte.

The Mg-rich primer and polyurethane clear topcoat system were applied onto the AA2024-T3 substrate and the platinum sensor was embedded between the primer and the topcoat. Afterwards, the coated substrate was put into the standardized Prohesion® chamber to simulate weathering conditions in an aggressive manner to induce accelerated coating failure. The acquisition of EIS and ENM data from embedded sensor in-situ monitoring during the Prohesion® dry and wet steps demonstrated the coating behavior evolution. In this study, it was found that both EIS and ENM in-situ monitoring could be conducted under either dry or wet Prohesion® steps with the embedded sensors. Under the dry step, the coatings were sensitive to temperature changing, while in the wet step, the resistance values were more scattered due to the moisture accumulation on the coating surface. Both the temperature and humidity variation related coating property changes in Prohesion® chamber were *in situ* monitored by the embedded sensors. It was found that the coating degraded continuously with Prohesion exposure time shown by a continuous decrease both in low frequency impedance $|Z|_{0.05\,Hz}$ and noise resistance R_n.

For detailed description of this experiment, refer to Appendix E, "In Situ Monitoring of a Mg-Rich Primer Beneath a Topcoat Exposed to Prohesion Conditions." This manuscript has been submitted to *Corrosion Science*.

5.5 Structural Analysis: Incorporation of dynamic strain into testing

In June of 2008, NDSU acquired a dual-column Series 800 High Performance Static and Fatigue Test System (Test Resources, Shakopee, MN). The machine is capable of performing series of static, dynamic, and fatigue tests with high performance high resolution load, strain, and position control (Figure 5.11). The dynamic strain machine was used to conduct an experiment to investigate the influence of dynamic strain on the performance of a standard Air Force coating system. The system consisted of a low-gloss polyurethane topcoat (Deft 03-GY-311) and a chromate pigmented epoxy primer (Deft 02-Y-40) applied unto panels of AA2024-T3. Two coated panels of dimensions 8 cm x 2.9 cm with a coating approximately 50 microns thick were used. One panel was designated as the control and was only subjected to immersion in 1% Harrison's Solution, but not to straining. The other was designated as the test sample and was subjected to a 2 mm sinusoidal strain by the machine under immersion in a similar electrolyte. Electrochemical impedance measurements (EIS) on the area of the sample that was under the tensile strain was made periodically after a given number of cycles.
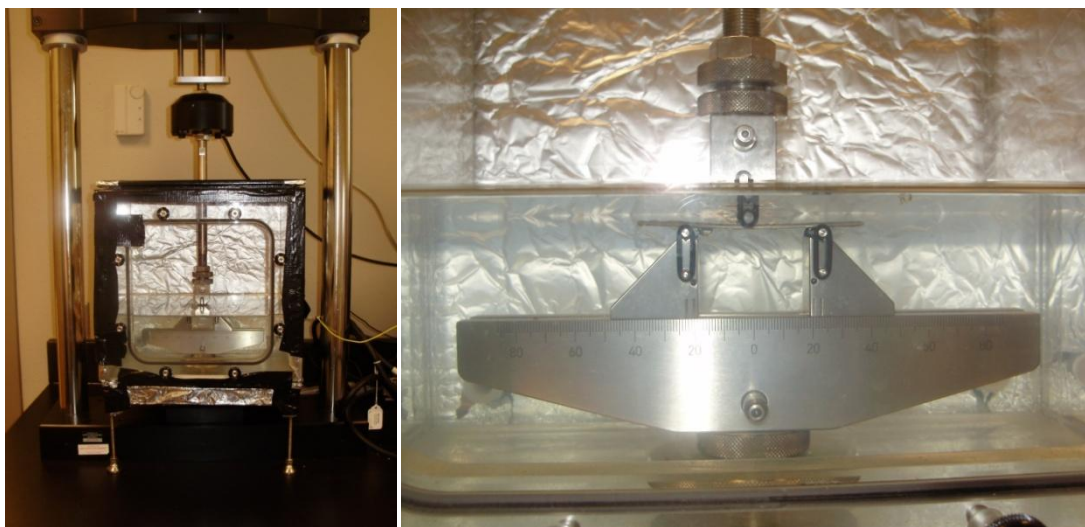
Figure 5.11. Dynamic stress apparatus (Test Resources, Shakopee, MN) at NDSU.

Whenever EIS measurements on the sample were made, EIS measurements on the control were made as well. Results associated with these measurements are shown in Figure 5.12. The low-frequency modulus, $|Z|_{0.01\,Hz}$, and the capacitance at 10 kHz, $C_{10\,kHz}$, are shown as functions of number of cycles for the sample. Although the control was not exposed to strain, included are the data associated with the control, for comparison and to eliminate the influence of immersion.
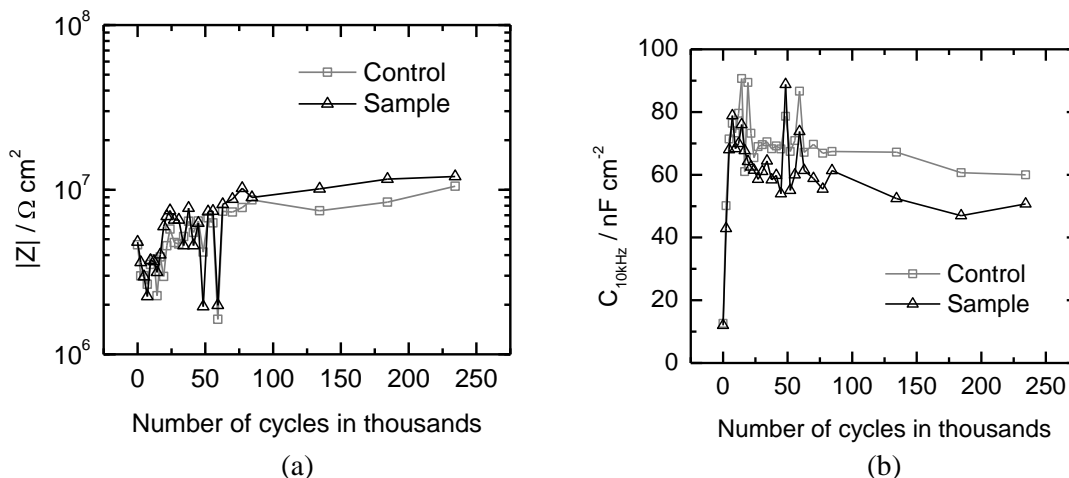
Figure 5.12. (a) Low frequency modulus and (b) capacitance as function of number of cycles for the sample exposed to cyclic strain conditions under immersion in 10% DHS. Included is a control that was not subjected to strain conditions.

The $|Z|_{0.01\,Hz}$ value is a measure of the barrier property of the coating while the $C_{10\,kHz}$ value is a measure of the increase in the dielectric response of the coating due to water ingress with time. It was observed that the barrier property and the change in dielectric property of the sample were similar to that of the control. The data are limited to 234,000 cycles. This was because the sample broke during the cyclic period after the EIS measurement at 234,000 cycles, and, therefore, no EIS data could be obtained from the broken sample. It was noted that the break in the panel was along the line of application of the force that produced the strain. This was consistent with literature, as the AA2024-T3 alloy suffers fatigue failure after cycles on the order of 200 to 400 thousand depending on the environmental conditions and level of strain. These results demonstrated that the low-gloss polyurethane topcoat and chromate epoxy primer system provided unchanged barrier protection up to 234,000 cycles of strain. Experiments are currently being conducted to explore the behavior of standard Air Force coatings during the cyclic period just before mechanical failure of the panel.

References for Section 5.0
D. Battocchi, J. He, G.P. Bierwagen, and D.E. Tallman, *Emulation and study of the corrosion behavior of Al alloy 2024-T3 using a wire beam electrode (WBE) in conjunction with scanning vibrating electrode technique (SVET),*Corrosion Science, **2005**, 47(5), 1165-1176.
C. L. Wu, X. J. Zhou, Y. J. Tan; *Progress in Organic Coatings*, **1995**, 25, 379-389.
M. E. Nanna and G. P. Bierwagen, J. Coating technol. Res. 2004, 1, 69.
D. Battocchi, A. M. Simoes, D. E. Tallman and G. P. Bierwagen, Corr. Sci. 2006, 48, 1292.
D. Battocchi, A. M. Simoes, D. E. Tallman and G. P. Bierwagen, Corr. Sci. 2006, 48, 2226.

6.0 Program Management

The Durable Hybrid Coatings program has the following management structure:
- Technical Manager for Department of Coatings and Polymeric Materials activities: Dante Battocchi, Research Assistant Professor, Department of Coatings and Polymeric Materials.
- Technical Manager for Center for Nanoscale Science and Engineering activities: Dr. Bret J. Chisholm, Senior Research Scientist, Center for Nanoscale Science and Engineering.
- Technical Manager for inorganic hard coatings Studies: Dr. Douglas L. Schulz, Senior Research Scientist, Center for Nanoscale Science and Engineering.
- Senior Scientific Advisor: Dr. Gordon Bierwagen, Professor, Department of Coatings and Polymeric Materials. [PI of record]
- Dr. Vsevolod "Séva" Balbyshev, Research Scientist, Center for Nanoscale Science and Engineering, coordinates new work on aircraft health prognostics.
- Program Manager and management POC for AFRL: Dr. Larry R. Pederson, Director, Center for Nanoscale Science and Engineering. Dr. Gregory J. McCarthy formerly served in this capacity until his recent retirement as Director of CNSE.

Additional senior research staff include:
- Dr. Kerry N. Allahar, Research Assistant Professor, Department of Coatings and Polymeric Materials.
- Dr. Jie "Jim" He, Research Associate, Center for Nanoscale Science and Engineering.
- Mr. James Bahr, Senior Research Engineer, Center for Nanoscale Science and Engineering.
- Mr. Robert Sailer, Research Engineer, Center for Nanoscale Science and Engineering.

Three Graduate Research Assistants and seven Undergraduate Research Assistants worked on this program during the past year.

The Durable Hybrid Coatings program at AFRL was initiated in July 2004, and with the supplement for new work added in 2008, the end date is now May 2011. An Annual Progress Report is prepared each year, with a Final Report due after the close of the program.

7.0 Financial Summary

The following table summarizes expenditures on the program through September 2009.

Durable Hybrid Coatings
Cooperative Agreement FA8650-04-1-5045
Annual Report for Period ending September 30, 2009

	July-04 through Sept-08	Oct-08 through Sept-09	Total Expenditures	Budget	Balance
Personnel	$1,393,622	$509,645	**$1,903,267**	$2,322,944	$419,677
Direct Operating Costs	$509,083	$108,882	**$617,965**	$684,357	$66,392
Subcontracts	$155,084	-$1,077	**$154,008**	$154,007	$0
Capital Equipment	$428,182	$42,265	**$470,447**	$508,182	$37,735
Indirect (F&A) Costs	$823,062	$256,606	**$1,079,667**	$1,300,309	$220,642
Total	**$3,309,033**	**$916,321**	**$4,225,354**	$4,969,800	**$744,446**

**Atmospheric Pressure Plasma Deposition of Transparent Conductors –
Tailoring Precursor Chemistries**

K.W. Johnson, S. Jha, C. Braun, K. Anderson, B. Halverson, K. Pokhodnya, S. Guruvenket,
R.A. Sailer and D.L. Schulz*

Center for Nanoscale Science and Engineering, North Dakota State University

1805 Research Park Drive, Fargo, ND 58102 USA

Abstract

Atmospheric-pressure plasma (APP) processes such as corona discharge have demonstrated utility in the cleaning steps associated with roll-to-roll manufacture. APP has more recently found applicability in the modification of surface energies given the ability to form plasma-polymerized coatings from precursors that contain an olefin functional group. The application of APP deposition to materials relevant to flexible electronics requires the use of functional precursors that maintain the following characteristics at 760 Torr: (1) a significant vapor pressure; (2) ability to be transported to the reaction zone without decomposition; and, (3) ability to form the targeted phase with byproducts that are eliminated from the growth surface. The utility of Sn(II) and In(III) β-diketonate complexes as precursors to transparent conducting In-Sn-O coatings via APP-enhanced chemical vapor deposition (APPECVD) was investigated. Thin films 50 to 100 nm in thickness were obtained using He and O_2 as the carrier and reactant gases, respectively. Growth temperatures ranging from 150 to 300 °C gave films with transmittance in excess of 90% over the visible spectrum and resistivities on the order of 10^{-4} Ω.cm.

Corresponding author: D.L. Schulz (doug.schulz@ndsu.edu)

1. **Introduction**

Transparent conducting oxides (TCOs) are used in numerous technologies that range from photovoltaics to flat-panel displays to anti-static coatings on polycarbonate canopies used in military aircraft [1,2,3]. Among the various materials systems, indium tin oxide (ITO) is perhaps the most widely adopted and well characterized with films exhibiting optical transparency >80% in the visible region while maintaining resistivities ~10^{-4} Ω.cm [4]. While ITO coatings are typically grown using vacuum-based processes (e.g., magnetron sputtering, chemical vapor

1

deposition [5,6]), there is presently interest in the development of atmospheric-pressure-based processes given the potential cost advantages associated with continuous manufacture on webs.

An APPECVD system equipped with a single precursor source was previously used to deposit conducting, highly transparent In-O films on glass [7]. Since that report, an additional precursor source was added to the system thereby allowing the ability to form two-component oxides such as tin-doped indium oxide (i.e., ITO). Toward that end, two In(III) and one Sn(II) β-diketonate precursors were utilized in the deposition of ITO coatings. The effects of variable precursor bubbler temperature, precursor feed-rate and He / O_2 mixtures upon film thickness, optical properties and electrical characteristics of the ITO films are the subject of this paper.

2. Experimental method

Metal-Organic Precursor Preparation and Characterization

The three precursors used in this study (i.e., indium (III) tris(acetylacetonate) = In(acac)$_3$, indium (III) tris(trifluoroacetylacetonate) = In(tfa)$_3$, and tin (II) bis(trifluoroacetylacetonate) = Sn(tfa)$_2$) are shown in Figure 1. All precursors were prepared and handled under inert conditions using standard Schlenk techniques including dual (vacuum/N_2) manifolds and N_2-filled gloveboxes. In(acac)$_3$ was purchased from Sigma-Aldrich and sublimed twice prior to use in the APPECVD system. In(tfa)$_3$ and Sn(tfa)$_2$ were prepared in-house according to a slight variation of a report by Hampden-Smith et al. [8].

Figure 1.

Proton ^{1}H spectra were obtained using a JEOL ECA 400MHz NMR spectrometer at CNSE. Thermal properties of the precursors were measured using a TA Q-Series SDT thermogravimetric analyzer / differential scanning calorimeter (TGA/DSC) installed inside a glove box. The analyses were performed from room temperature to 350 ^{o}C at a rate of 10 ^{o}C/min. Samples of 2-6 mg were used for this analysis and the N_2 carrier gas was fixed at 200 sccm.

In(tfa)$_3$. A suspension prepared by adding 1.72g (71.7 mmol) NaH to 60mL dry tetrahydrofuran (THF) was cooled with an ice bath. To the stirring suspension was slowly added 9.40g (61.0 mmol) 1,1,1-trifluoro-2,4-pentanedione (Htfa) with controlled evolution of H_2 gas. After addition, the reaction mixture was allowed to warm to room temperature (RT) over the course of

30 min and then stirred for an additional 2 h. Subsequently, 4.00g (18.1 mmol) of $InCl_3$ was added under a positive pressure of N_2 with the Na(tfa), $InCl_3$, NaCl mixture stirred for 12 h. The THF solvent was removed *in vacuo* and the remaining crude solid was twice sublimed to obtain pure In(tfa)$_3$. Characterization using ^{1}H nmr (CDCl$_3$) showed the anticipated singlet peaks at 5.89 ppm (methine proton) and 2.26 ppm (methyl protons). The sealed capillary melting point of the purified In(tfa)$_3$ was 123 °C and total purified yield was 7.66 g (74 %).

Sn(tfa)$_2$. The crude tin complex was prepared in analogy to In(tfa)$_3$ described above using the following quantities of reagents: NaH = 3.89 g (162 mmol); THF solvent = 225 mL; Htfa = 24.96 g (162 mmol); and, $SnCl_2$ = 15.36 g (81 mmol). After THF solvent removal *in vacuo*, Sn(tfa)$_2$ was extracted from the crude solid with dry pentane and separated from the NaCl byproduct by filtration. The solid residue remaining after *in vacuo* removal of pentane was sublimed twice giving 18.14g of Sn(tfa)$_2$ with a melting point of 53 °C (54 % yield). ^{1}H NMR (CDCl$_3$) spectra showed singlets at 5.83 ppm (methine proton) and 2.19 ppm (methyl protons).

<u>In-Sn-O Film Growth and Characterization</u>

In-O and In-Sn-O coating were deposited using a previously described Surfx Atomflow[TM] 250D atmospheric plasma system [9, 10]. Plasma power was maintained at 110W while the plasma head was heated to 165 °C to prevent condensation. The standoff distance between the substrate and the plasma head was fixed at 2 mm and film uniformity was optimized by rastering the plasma source across the substrate in a serpentine pattern. The variables in this study were precursor gas flow rate, precursor temperature and substrate temperature. It is important to note that care must be made to avoid the condensation of the precursor within the precursor feed lines and these modifications have been previously described [7]. The substrates used in this study were 38 x 78 mm^2 microscope glass slides (VWR) and 2 x 2 cm^2 single-crystal Si wafers (University Wafers). All substrates were treated with piranha etch (H_2SO_4:H_2O_2), rinsed with DI water and stored in isopropanol. Immediately prior to film growth studies, the substrates were removed from isopropanol and blown dry under a stream of N_2.

A schematic of the NDSU APPECVD (Fig. 2) shows the gas delivery system, plasma head and substrate arrangement for these experiments. The solid precursor "bubblers" were located in two separate ovens allowing independent temperature control. Helium carrier gas flowed over the

3

metal-organics and this precursor-containing stream was mixed into the O_2/He plasma gas stream as shown in Figure 2. The flow of carrier gas to the bubblers and to the bypass were controlled individually using mass flow controllers. Good quality ITO coatings were observed when the precursor vapors were introduced into the plasma afterglow region.

Figure 2.

The chemical composition of the ITO films deposited on Si wafers was measured using x-ray fluorescence (XRF) spectroscopy using a ZSX Primus model equipped with a rhodium x-ray source (4 kW). The XRF analyses utilized a 20 mm spot size while the L_α lines of In and Sn were scanned with a 40 kV / 75 mA x-ray beam using no additional filters. Scans were performed at 0.4 second per step, with a step being 0.05 degrees.

Film thicknesses were determined via contact profilometry using a KLA-Tencor P-15 stylus profiler. UV-Vis spectroscopy was performed using a Varian Cary 5000 UV-Vis-NIR spectrometer in transmission mode with a scan range from 250 to 2000 nm at 60 nm/min scan velocity. Transmission signal from the bare glass sample was used as a background signal and was subtracted from the experimental signal. Sample resistances were determined by using a cascade Microtech C4S44/S four-probe point with a Keithly 2400 multimeter. Multiple measurements were on each sample and the values reported are the average of typically six spots. Hall probe data was collected using a Quantum Design PPMS.

3. Results and discussions

The thermal characteristics of the three metal-organic complexes are listed as follows: In(acac)$_3$, melting point (mp.) 185 °C, t_{98} (i.e., temperature when mass loss of two percent is observed) =164 °C, t_{50} (i.e., temperature when mass loss of 50 percent is observed) = 218 °C, t_5 (i.e., temperature when mass loss of 95 percent is observed) = 232 °C and residue remaining at 300 °C = 0 %; In(tfa)$_3$, mp. 123 °C, t_{98} = 114 °C, t_{50} = 185 °C, t_5 = 200 °C and residue remaining at 300 °C = 3.1 %; and, Sn(tfa)$_2$, mp. 53 °C, t_{98} = 69 °C, t_{50} = 146 °C, t_5 = 162 °C and residue remaining at 300 °C = 1.6 %. Based on the above characterizations, bubbler temperatures for In(acac)$_3$ and Sn(tfa)$_2$ were maintained at 187 ^{o}C and 67 ^{o}C, respectively with the bubbler for In(tfa)$_3$ varying from 115 to 130 ^{o}C.

4

ITO Films from In(acac)$_3$ and Sn(tfa)$_2$

Growth parameters and characterization data for ITO films deposited from In(acac)$_3$ and Sn(tfa)$_2$ are compiled in Table 1. A He plasma gas rate of 30 LPM was employed and O$_2$ reactant gas was added into this stream at a flow rate of 350 or 500 sccm. The He precursor gas flow rate over the In(acac)$_3$ was fixed at 500 sccm while the Sn(tfa)$_2$ precursor carrier gas flow rate was varied as follows: 16.8 sccm for a targeted 5 at.% Sn / 95 at.% In (on a metals basis); 35.6 sscm for 10 at.% Sn; and, 56.4 sccm for 15 at.% Sn. A deposition temperature of 250 °C and growth period of 35 min gave ITO films that ranged in thickness from 33 to 376 nm. The shorter standoff distance of 2 mm gave much thicker films. The XPS data indicates that the %Sn in the films was always less than the target (i.e., 5%, 10% or 15%). While it appears these films suffer from a significant C contamination, the XPS system employed in this study (Asemblon Inc., Redmond, WA) did not have the ability to sputter clean adsorbed CO$_2$ and so the carbon being incorporated into the APPECVD films from the precursors remains unquantified. The Hall probe carrier concentration in these ITO films ranged from 2.5×10^{19} to 1.1×10^{20} cm^{-3} as compared to 2.1×10^{21} for a commercial sample. In addition, drift mobilities of the APPECVD films were lower (i.e., 0.50 to 6.5 cm^2/V·s) than the commercial sample (i.e., 35 cm^2/V·s). In spite of the inferior carrier properties, several APPECVD ITO films exhibited sheet resistance in the range of 300 to 400 Ω/□; a value that is only about 10 times that observed for the ITO film from Colorado Concept Coatings.

Table 1.

Figure 3 shows the surface morphology of a typical ITO film as determined via atomic force microscopy (AFM). Grain sizes of 50 to 100 nm can be seen throughout the film with consistent size distribution. Similar results were observed for all ITO films deposited on glass indicating that nucleation and grain growth does not vary significantly over the investigated parameter space. Similar morphologies have been observed in ITO films prepared by sputtering [11]. It is interesting to note that films grown at or above 200 °C are adherent and pass the tape-pull adhesion test.

Figure 3.

ITO Films from In(tfa)$_3$ and Sn(tfa)$_2$

Growth parameters and characterization data for ITO films deposited from In(tfa)$_3$ and Sn(tfa)$_2$ are compiled in Table 2. Only In(tfa)$_3$ was used during the initial runs in order to determine a

5

calibration curve that would be necessary for a target tin doping level (Table 2, samples 2-4). An increase in the coating thickness from 70 nm to 90 nm was observed when the $In(tfa)_3$ bubbler temperature was increased from 110 ^{o}C to 130 ^{o}C – an observation that is consistent with a higher flux of precursor into the boundary layer. The effect of the He/O_2 plasma gas flow on the film thickness was also carried out using only the $In(tfa)_3$ precursor (Table 2, samples 5-7). A plasma gas flow rate of 20 LPM gave the highest growth rate and this value was chosen as a fixed variable in all the following experiments.

The $Sn(tfa)_2$ precursor was added into the system by flowing 50 sccm of He through the 67 ^{o}C bubbler. [Note: data from a previous calibration test for $Sn(tfa)_2$ indicated that this temperature should allow the growth of ~10% tin-doped ITO films.] The plasma and precursor carrier gas flows were held constant while the substrate temperature was changed from 150 ^{o}C to 300 ^{o}C (Table 2, samples 8-11). The coating deposited at 150 ^{o}C was powdery and non-uniform with poor adhesion to the substrate. By way of comparison, those films deposited at or above 200 ^{o}C passed the tape pull test and were of reasonable thickness (i.e., 120 to 140 nm). The increase in the coating thickness with increasing substrate temperature is attributed to enhanced surface chemical reaction of the incoming species (from the plasma source exit) on the substrate.

Electrical properties of the ITO films were determined via four point probe. Sheet resistance was observed to decrease with increasing deposition temperature with values ranging from 1.5×10^6 $\Omega/\square$ for a film deposited at 200 ^{o}C to 5,000 $\Omega/\square$ for the film at 300 ^{o}C. These values are high when compared to the commercial ITO coating (i.e., 26 $\Omega/\square$) as well as previous reports for indium oxide coatings [10]. This suboptimal conductivity could be attributed to the residual impurities (e.g., C or F, see below) or perhaps by being off-stoichiometry when considering the target of 10% tin-doped ITO (metals basis).

Chemical composition of the ITO samples (i.e., 8 - 10) was determined using XRF spectroscopy on single crystal Si substrates in comparison with the ITO film from Colorado Concept Coatings used as a standard (Table 2). In/Sn intensity ratio in the ITO films ranged from 0.65 to 0.94 while In/Sn = 2.68 was observed for the ITO from Colorado Concept Coating. While significant fluorine and carbon were present in all samples, the fluorine was observed to decrease with increasing temperature while the carbon level remained nearly constant. While these films have much more tin than was targeted, it appears that the conditions changed from when the $Sn(tfa)_2$

6

calibration curve was obtained and the ITO films were prepared from $Sn(tfa)_2$ and $In(tfa)_3$. Causes for such a change might include clogging of the system by precursor condensation or premature nucleation of ITO powder. In addition, it is possible that the two precursors are interacting in the gas phase in such a manner that the growth of Sn-O is favored over the In-O phase given differences in sticking coefficient. Future investigations will be aimed at understanding the dynamics of gas mixing toward rendering the APPECVD process reproducible.

Figure 4 shows the optical characteristics of samples #8 - #11 as determined by UV-Vis spectroscopy. The ITO coating deposited at 150 ^{o}C showed poor transmittance while the films grown T ≥ 200 °C exhibited T > 90 %. The film grown at low temperature (i.e., 150 ^{o}C) is not well-adhered to the substrate and has a hazy/cloudy appearance that is likely a consequence of scattering at non-dense film regions. The improvement observed for films deposited at higher temperatures might be rationalized in terms of the additional energy available at the growth surface whereby APPECVD reactive species remain mobile and are able to feed into the growth surface. These results are in-line with growth models presented for sputter deposition and vacuum evaporated thin films [12]. Also, these observations are related to previous atmospheric plasma deposition studies whereby increased surface diffusion promotes film densification [13].

Figure 4.

Finally, it is important to note the marked effect of the atmospheric-pressure plasma in this process. Control experiments were performed using similar growth conditions (i.e., plasma gas flow rate, precursor gas flow rate, etc.) for the growth of ITO films but in the absence of the plasma. It is interesting to note that no coatings were observed without the plasma even when a substrate temperature of 300 ^{o}C was employed. This result teaches the importance of plasma in the thin film formation whereby the APPECVD process cannot be explained simply in terms of thermal CVD (i.e., precursor thermolysis and subsequent surface chemical reactions). Instead, plasma fragmentation of O_2 reactant gas and subsequent radical chemistry in the afterglow region appear to be an important part of the process. Future experiments may be undertaken to understand which component of the plasma (i.e., the oxygen radicals or UV light) are most important in film growth. In addition, experiments may be performed at higher deposition

7

temperatures such that the incoming radical species can acquire sufficient energy to find a minimum energy position thereby yielding continuous, dense thin films.

4. Conclusions

Highly-transparent ITO films with moderate resistivity were deposited on glass and Si via APPECVD using metal β-diketonate precursors. It is anticipated that the further optimization of the process (i.e., modeling of gas mixing) will yield improved sheet resistance by affording better control of the In to Sn ratio. In addition, the influence of F doping (i.e., from the fluorinated precursors) and C contamination will be investigated as a means of improving the electrical properties of as-deposited ITO films.

5. Acknowledgements

6. References

1. E. Fortunato, D. Ginley, H. Hosono, and D. C. Paines, "Transparent Conducting Oxides for Photovoltaics" *MRS Bull.*, 32, 242, 2007.
2. I. Hamberg and C. G. Granqvist, "Evaporated Sn-doped In2O3 films: Basic optical properties and applications to energy-efficient windows" *J. Appl. Phys.*, 60, R123, 1987.
3. J. Dai, X. Jiang, H. Waag and D. Yan, "Organic photovoltaic cells with near infrared absorption spectrum", *Appl. Phys. Lett.*, 91, 253503, 2007.
4. T. J. Coutts, D. L. Young, X. Li, W. P. Mulligan, and X. Wu, "Search for improved transparent conducting oxides: A fundamental investigation of CdO, Cd_2SnO_4, and Zn_2SnO_4" , *J. Vac. Sci. Technol. A*, 18, 2646, 2000.
5. H. Han, D. Adams, J. W. Mayer and T.L. Alfors, "Characterization of the physical and electrical properties of Indium tin oxide on polyethylene napthalate", *J. Appl. Phys.*, 98, 083705, 2005.

8

6. S. Y. Ryu, S. H. Choi, J. T. Kim, H. K. Baik and H. S. Jeong, "Highly efficient transparent organic light-emitting diodes by ion beam assisted deposition-prepared indium tin oxide cathode", *Appl. Phys. Lett.*, 90, 033513, 2007.

7. R. A. Sailer, A. Wagner, C. Schmit, N. Klaverkamp, and D.L. Schulz, "Deposition of tranparent conductive indium oxide by atmospheric pressure plasma jet", *Surf. Coat. Technol.*, 203, 835, 2008.

8. H. K. Shin, , K. M. Chi, J. Farkas, M. J. Hampden-Smith, T. T. Kodas, E. N. Duesler, "Chemistry of Copper(I) B-diketonate complexes. 2 Synthesis , Characterization, and Physical Properties of (B-Diketonato)copper(I) Trimethylphosphine and Bis(trimethylphosphine Complexes" Inorg. Chem., 31, 424, 1992.

9. M. Moravej, R.F. Hicks, "Atmospheric Plasma Deposition of Coatings Using a Capacitive Discharge Source", *Chem. Vap. Deposition,* 11, 469, 2005.

10. M. D. Barankin, E. Gonzalex, A.M. Ladwig, R.F. Hicks, "Plasma-enhanced chemical vapor deposition of zinc oxide at atmospheric pressure and low temperature", *Sol. Energy Mater. Sol. Cells*, 91, 924, 2007.

11. L. Kerkache, A. Layadi, E. Dogheche, and D. Remiens, "Physcial Properties of RF Sputtered ITO Thin Films and Annealing Effect," *J. Phys. D: Appl. Phys.*, 39, 184, 2006.

12. Materials Science of Thin Films, Deposition and Structure, edited by M. Ohring, 2nd Edition, Academic Press, New York, 2002.

13. F. Massines, N. Gherardi, A. Fornelli, S. Martin, "Atmospheric pressure plasma deposition of thin films by Townsend dielectric barrier discharge", *Surf. Coat. Technol*., 200, 1855, 2005.

9

$\text{In(acac)}_3 \quad n = 3, \quad M = \text{In}, \quad R_1 = R_2 = CH_3$

$\text{In(tfa)}_3 \quad n = 3, \quad M = \text{In}, \quad R_1 = CH_3, \ R_2 = CF_3$

$\text{Sn(tfa)}_2 \quad n = 2, \quad M = \text{Sn}, \quad R_1 = CH_3, \ R_2 = CF_3$
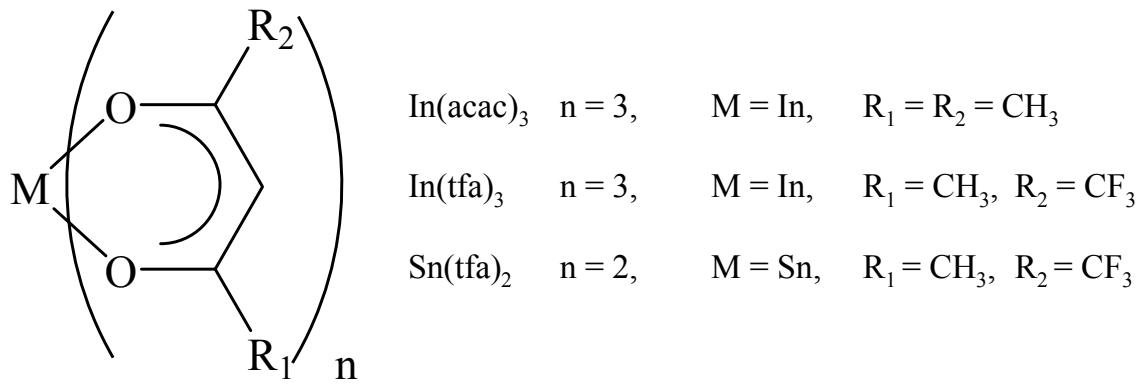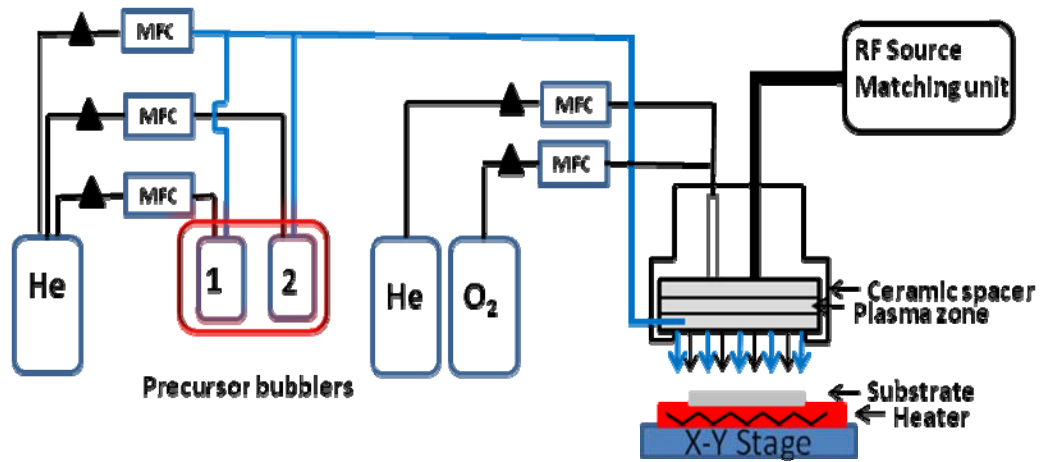
Figure 1. Schematic of Indium and Tin APPECVD Precursors.

10

54

Figure 2. Schematic of NDSU APPECVD System.
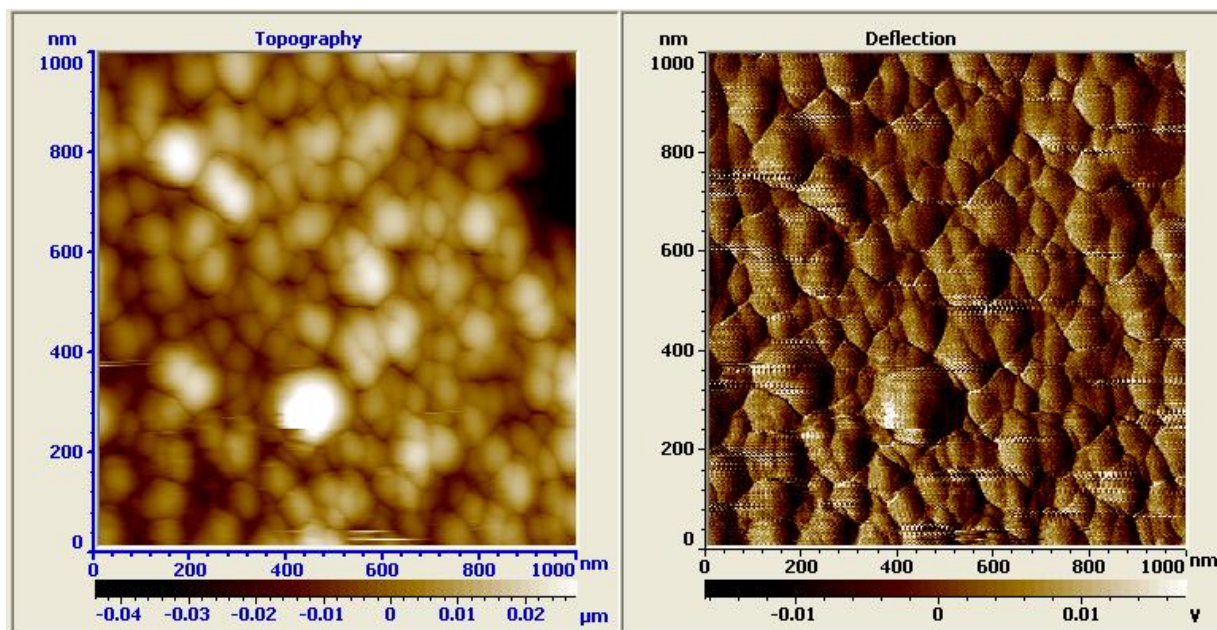
Figure 3. AFM Images of an ITO Film Prepared from In(acac)$_3$ and Sn(tfa)$_2$.

12
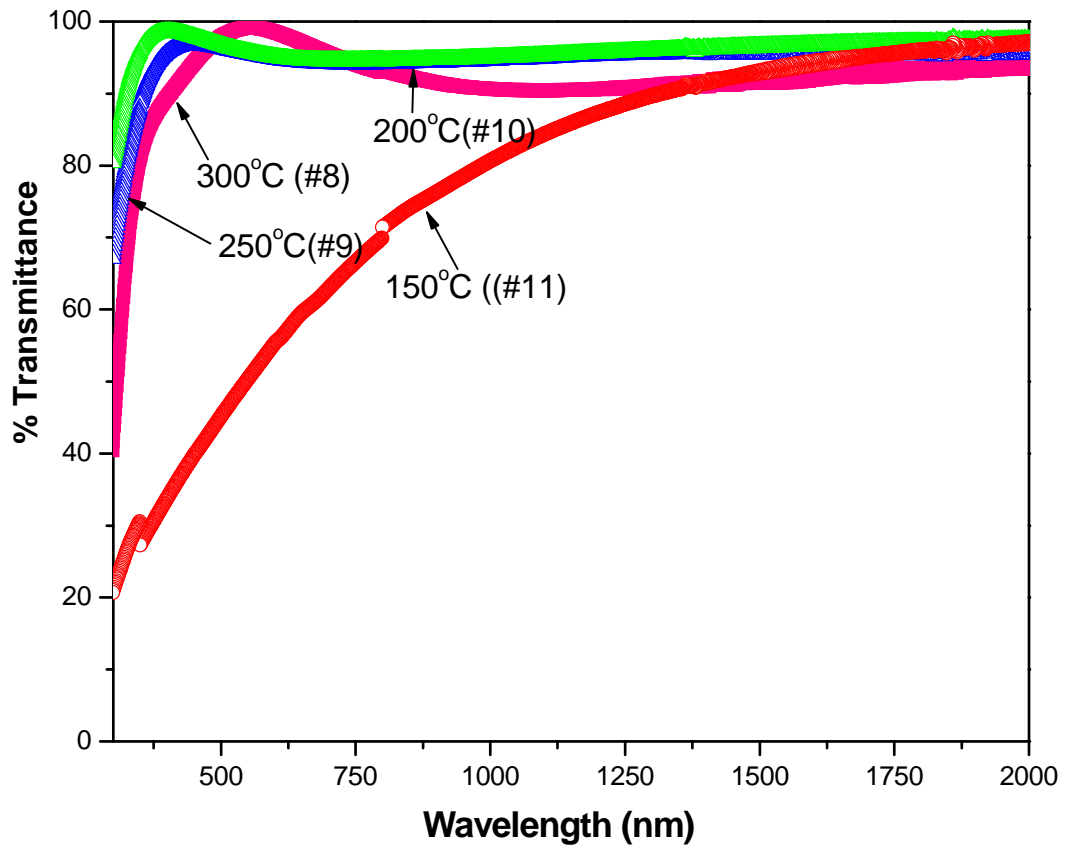
Figure 4. UV-Vis Transmission Spectra of ITO Coatings Prepared from In(tfa)$_3$ and Sn(tfa)$_2$.

13

Table 1. APPECVD Parameters and ITO Film Properties for Coatings Prepared using In(acac)$_3$ and Sn(tfa)$_2$.

Sample Conditions[a]	Thickness (nm)	Elemental Composition from XPS (Atomic %)				% Sn	Sheet Resistance ($\Omega/\square$)	ρ (Ω cm)	n (cm^{-3})	μ_{drift} (cm^2/Vs)
		In	Sn	O	C					
10%, 4mm, 350sccm O$_2$	95	19.5	0.5	41.1	38.9	2.5	630	6.0E-3	6.1E19	6.1
5%, 2mm, 500sccm O$_2$	298	10.4	0.4	28.1	61.1	3.7	420	1.3E-2	2.6E19	6.5
15%, 2mm, 500sccm O$_2$	194	14.5	1.3	37.2	47.1	8.2	335	6.5E-3	8.6E19	2.5
10%, 2mm, 350sccm O$_2$	376	18.3	0.6	37.7	43.5	3.2	368	1.4E-2	2.8E19	3.6
10%, 4mm, 500sccm O$_2$	33	15.4	0.4	34.0	41.4	2.5	8320	2.7E-2	1.1E20	0.5
CC [b]	100						26	2.6E-4	2.1E21	35.1

Legend: [a] Sample conditions are listed in terms of targeted Sn composition (e.g., 10%), the standoff distance (e.g., 4 mm) and the flow rate of the O$_2$ reactant gas; [b] CC is an ITO coating purchased from Colorado Concept Coatings.

14

Table 2. APPECVD Parameters and ITO Film Properties for Coatings Prepared using In(tfa)$_3$ and Sn(tfa)$_2$.

ID	Subst Temp (°C)	In(tfa)$_3$ Bubbler Temp. (°C)	Precursor Flow Rate (sccm)		He/O$_2$ Flow (LPM)	Film Thickness (nm)	Sheet Resistance (Ω/□)	ρ (Ω cm)	In/Sn from
			In(tfa)$_3$	Sn(tfa)$_2$					
2	300	115	4.5	0	30	70	x	x	x
3	300	120	4.5	0	30	80	x	x	x
4	300	130	4.5	0	30	90	x	x	x
5	300	130	4.5	0	30	90	x	x	x
6	300	130	4.5	0	20	104	x	x	x
7	300	130	4.5	0	14	35	x	x	x
8	300	130	4.5	50	20	148	5.0E3	7.5E-2	0.65
9	250	130	4.5	50	20	133	2.6E4	3.5E-1	0.62
10	200	130	4.5	50	20	120	1.5E6	18	0.40
11	150	130	4.5	50	20	x	x	x	0.94
CC	x	x	x	x	x	100	26	2.6E-4	2.68

[Note: x indicates data that is not applicable or not quantifiable.], CC is an ITO coating purchased from Colorado Concept Coatings.

15

EMBEDDED SENSOR ELECTRODE ARRAYS FOR REAL TIME MONITORING OF AN AIR FORCE TOPCOAT/MG-RICH PRIMER SYSTEMS

V.N. Balbyshev, K.N. Allahar,* D. Battocchi,* G. Strommen, and A. Reinholz
Center for Nanoscale Science & Engineering,
NDSU Dept 4310, Fargo, ND 58108

Department of Coatings and Polymeric Materials
North Dakota State University
NDSU Dept 2760, Fargo, ND, 58108

seva.balbyshev@ndsu.edu, kerry.allahar@ndsu.edu, dante.battocchi@ndsu.edu,
greg.strommen@ndsu.edu, aaron.reinholz@ndsu.edu

ABSTRACT

Mg-rich primers are chromate-free alternatives that are currently used by the Air Force for the protection of aluminum structures. Magnesium pigments undergo anodic dissolution thus protecting the less electrochemically active aluminum substrates. At the same time, corrosion products of Mg dissolution act as a barrier that insulates the substrate from corrosive environment. Characterization of a standard Mg-rich primer/Air Force urethane topcoat was carried out by electrochemical impedance spectroscopy (EIS) and on coated AA2024-T3 substrates subjected to exposure conditions according to a constant immersion test protocol. Sensor electrodes of a newly-developed design were made by the industry standard selective laser etching procedure utilized by many common printed circuit board manufacturers. Unlike conventional electrochemical sensors that monitor the metal substrate itself and provide no information about the coating, these corrosion sensors are embedded between the primer and the topcoat and thus are suitable for monitoring the corrosion protection afforded by the metal-rich primer. As an added advantage, the embedded sensor electrodes are shielded from the environment by the topcoat. This prolongs the electrode life, as well as reduces the noise associated with measurement. The sensor electrodes of different surface areas were embedded between the primer and the topcoat. An array of sensor electrodes was used to assess the behavior of the Mg primer underneath the topcoat. Experimental results demonstrated the feasibility of the embedded sensor electrode array approach to monitor cathodic protection of Mg-rich primers on structural aluminum alloys by *in situ* and electrochemical impedance spectroscopy (EIS) technique. The presented embedded sensor electrode array is part of the effort aimed at development of wireless corrosion sensors for monitoring cathodic protection of metal-rich primers.

Keywords: Mg-rich primer, embedded sensors, EIS

1. Introduction

Aluminum alloys, especially AA2024-T3, are widely used in the aerospace industry because of their high strength and stiffness combined with low density. However, Al alloys are very sensitive to corrosion environments due to their high copper content. Currently, chromate pre-treatment and chromate primer coatings are used to protect aluminum alloys from corrosive attacks.[1] Current coating systems for aircraft corrosion protection are based on a traditional chromate surface treatment, primer, and topcoat. To date, the corrosion protection of aluminum alloys has relied extensively on potent hexavalent-chromium compounds, which are included in both surface preparation/treatments and organic primers. However, the toxicity and carcinogenic properties of chromium has caused federal agencies, in particular the EPA, to impose severe restrictions on its use.[2] Corrosion protection of aluminum-skinned aircraft and development of improved environmentally benign surface treatments for aluminum aerospace alloys are critical needs for the aerospace industry. Recently developed metal-rich coatings for corrosion protection of aircraft aluminum alloys rely on magnesium powder dispersed in an organic binder. It has been shown that this environmentally friendly formulation of Mg-rich coatings can provide exceptional protection for aluminum-based alloys.[3,4] In these metal-rich coatings, Mg particles embedded in a polymeric matrix act as a sacrificial anode; Mg undergoes anodic dissolution and thus protects the underlying metal from corrosion. By analogy to the Zinc-rich primer coatings that keep steel from corrosion through cathodic protection, the Mg-rich primer (MRP) coatings, were designed, examined and developed by M. E. Nanna, D. Battocchi and G. P. Bierwagen at NDSU.[5,6] By using pure magnesium pigment, which is more active than aluminum alloy substrate, Mg-rich primers were formulated around the Critical Pigment Volume Concentration (CPVC) to make sure there are good electrical conductivities among pigment particles and between pigment and substrate. This work motivated by the need for chromate-free alternatives for protection of high-strength aircraft Al alloys such as AA2024-T3 and AA7075-T6. G.P. Bierwagen and the corrosion group at NDSU are leading this Mg-rich primers research and a series of articles have been published on their application and properties.[7,8]

2

Recently, there has been extensive development of several *in situ* sensing techniques that monitor the barrier properties of a coating. Most research in electrochemical sensors has been focused on sensor electrodes embedded in the substrate. Such sensors monitor corrosion of the metal substrate but provide no information about the film itself. Thus, they are unsuitable for monitoring corrosion within the metal-rich primer itself.

A new technique for *in situ* monitoring of a coating with *ac* involves the application of an embedded electrode or sensor within the coating. There are only a limited number of groups globally that are actively involved with the application of the embedded sensor technology.[9-11] The Department of Coatings and Polymeric Materials and Center for Nanoscale Science and Engineering at NDSU have been at the forefront in the development, feasibility demonstration, and application of embedded sensors, which consist of electrodes that act as the counter and reference but are placed between the layers of two-layered coating systems.[12,13] A schematic diagram of the embedded sensor is shown in Figure 1. An advantage of the embedded electrodes is that they are shielded from the environment by the topcoat, which prolongs the electrode life as well as reduces the noise associated with measurements. Another advantage is that electrochemical measurement of the primer and primer/metal interface can be made without being masked by high resistant topcoats.

Until now, the embedded sensors approach has been applied for characterization of standard Air Force and Army vehicle coatings that are evaluated by thermal cycling accelerated testing method,[14] and accelerated ac-dc-ac testing method.[15] While there have been limited studies published on the use of embedded sensors in the aforementioned coating systems, there has been no application to metal rich primers, *e.g.* Mg- or Zn-rich primers. The coupling of embedded sensors and coating systems with Mg-rich primers is a unique approach that allows *in situ* monitoring of the electrochemical behavior of protective Mg-rich primers beneath a topcoat.

3

The newly-developed embedded sensor electrode array is part of the effort aimed at development of wireless corrosion sensors for monitoring cathodic protection of metal-rich primers. Sensor electrodes of a new design were made by the industry standard selective laser etching procedure utilized by many common printed circuit board manufacturers. Sensor electrodes of different surface areas were embedded between the primer and the topcoat. An array of sensor electrodes was used to assess the behavior of the Mg primer underneath the topcoat. Sensor arrays were manufactured in a multi-stage process, involving standard industrial deposition procedures using industrial grade equipment.

Electrochemical Impedance Spectroscopy (EIS) is a fast and useful method widely applied in monitoring and evaluating the performance of organic coatings, especially the corrosion protection abilities. In this study, EIS was used to characterize the electrochemical performances of Mg pigmented primers as a function of exposure time.

2. Experimental

The protective coating system used in the experimental procedure was composed of a high solids polyurethane gloss enamel (AKZO NOBEL 646-58-7925 with AKZO NOBEL X-501 curing component) and a Mg-rich primer developed at NDSU.[16] In this primer, Mg powder with the average particle size of 25 µm (Ecka Granules of America, Orangeburg, SC) was dispersed in a two-component epoxy-polyamide resin, and the pigment volume concentration (PVC) of the primer was 45%. The primer was applied to standard panels of aluminum alloy AA2024-T3. After the application of the primer, the sensor was applied on the surface of the primer, followed by the application of the polyurethane topcoat.

2.1. Sample preparation

The aluminum alloy 2024-T3 panels, 4" x 8" in size were polished by 200 grit followed by 600 grit sanding paper, then washed with hexane and dried with a nitrogen flow. The freshly pretreated metal panels were coated within half an hour after they were polished.

Four platinum circuit sensors on Kapton® backing, manufactured at NDSE Center for Nanoscale Science and Engineering (CNSE), were placed on cleaned 4" x 8" aluminum panels.

4

A thin layer of a homemade epoxy resin (D.E.R. 331 epoxy resin/Ancamide 2353/methyl ethyl ketone at a 5/3/5 weight ratio) was applied to the Pt track connecting the sensor pad to the wire terminals. The arrangement of the sensors on the test panel is shown in Figure 2. After 10 minutes of solvent flash-off, a few drops of the epoxy were placed on the primer, and the circuit sensors were then adhered onto the primer. The primer and the glued sensors were given one day to harden at room temperature before the polyurethane topcoat was applied. The approximate neat dry film thickness of Mg-rich primer was 40 ± 5 µm, and 80 ± 10 µm for the topcoat.

2.2 Experimental Configurations

The *in situ* monitoring of the Mg-rich primer and polyurethane topcoat paint system was carried out under constant immersion conditions. Electrochemical Impedance Spectroscopy (EIS) was collected on a Gamry PCI4-300 potentiostat coupled with Corrosion Measurement System CMS100 and CMS300 software. Detailed description of this electrochemical technique can be found elsewhere.[17,18] The spectra were obtained in the frequency range from 10 mHz to 100 kHz at 10 mV RMS imposed *ac* potential (vs. E_{oc}).

Both the two-electrode (2E) cell for sensor-to-sensor measurements and three-electrode (3E) cell arrangement for sensor-to-substrate measurements were used to obtain the EIS responses in a one-panel setup, where a coated panel was assembled with four sensors placed in rows of two as shown in Figure 3 (a). Areas marked with circles are exposure areas subjected to constant immersion in dilute Harrison's solution (DHS) (0.05 wt% NaCl / 0.35% $(NH_4)_2SO_4$, pH=5.5). The scribed and un-scribed areas were exposed to DHS by virtue of clamping a glass cell with an o-ring over the corresponding spot, resulting in a total exposure area of 6.45 cm². For the sake of simplicity, the individual sensors in positions 1, 2, 3, and 4 in Figure 3 (b).will be referred to as Sensor 1, Sensor 2, etc. For the 3-electrode setup, a platinum mesh counter electrode and saturated calomel reference electrode (SCE) were utilized in a three-electrode configuration. In the 2-electrode

5

arrangement, one sensor was connected to the working electrode and the other sensor connected to the counter and reference electrodes.

3. Results and Discussion

<u>Flexible Circuit Sensor Design</u>

The feasibility of Pt-mesh embedded sensors developed at NDSU for monitoring the effectiveness of Mg-rich primers has been documented previously.[12-14] In these studies, embedded sensors were either completely immersed in corrosive electrolyte or were subjected to cyclic salt fog environment, and thus the area surrounding the sensors was corroding at approximately the same rate as the entire panel. In this case, for the sensor to accurately detect corrosion, it is important to design a sensor in such a way as to not to impede the ingress of electrolyte and allow it to reach the Mg-rich primer and trigger corrosion reactions in the system. She U-shape design of these sensors suited extremely well for this purpose. However, one of the drawbacks of Pt-mesh sensors is their delicate nature. At thicknesses of 120 nm, Pt-mesh sensor had to be handled with care, application of sensors required specially trained lab personnel. Additionally, the wires protruding from the test sample made it ideal for laboratory use, but made them impractical in the field.

Researches and engineers and NDSU CNSE have used the available technologies for circuit printing in designing a new prototype of the sensor that would address the two main drawbacks of the Pt-mesh sensor. In addition to being robust and reproducible, the new sensor would be flexible as to allow easy application to a range of geometries of structural parts.

The new "circuit sensor" was made to resemble the U-shape design of the Pt-mesh sensor in order for researchers to do similar type of experimentation with embedded sensors in application involving metal-rich primers. Instead of making a sensor into a simple (rectangular or circular) planar shape, a provision for ingress of electrolyte was made in the form of conducting 'fingers' separated by gaps of varying widths allowing for electrolyte to penetrate into the primer. Initially, the widths of the fingers and

6

spacings between them ranged from 250 µm to 2000 µm, resulting in nine different finger/spacing configurations. Sensor design is shown in Figure 4 displays two sensors with different finger-spacing dimensions. The sensor design concept shown in Figure 4 was translated into a CAD drawing using Design Capture/Expedition by Mentor Graphics (Mentor Graphics, Wilsonville, OR). Sensor design took into consideration the embedded aspect of the corrosion sensor.

In the next step, the inverted image of the sensor generated by CAD software was used to manufacture a shadow mask (stencil) for subsequent physical vapor deposition of metallic film (conductive path of a sensor). The stencils were made from series 316 stainless steel by Great Lakes Engineering (Maple Grove, MN). Initially, nine variations of stencils with varying finger and spacing widths were manufactured. The deposition step was performed at NDSU CNSE on a CMS-18 PVD sputtering sustem (Kurt J. Lesker Company, Clairton, PA). For better adhesion, a 50 Å layer of Cr (99.95% pure, from Kurt J. Lesker Company, Clairton, PA) was first vapor deposited on a 2 mil thick Kapton® film (obtained from McMaster-Carr, Robbinsville, NJ), followed by the deposition of 1500 Å layer of Pt (99.99% from Equipment Support Company USA Inc., Pensacola, FL).

Following the deposition, the Kapton® pieces, 15 cm in diameter each, were transferred to the Optec MicroMaster laser ablation station (Z.A.E. Le Crachet, Frameries, Belgium) where the spacings between the fingers were cut out by laser. During the laser ablation step, it was discovered that sensors with closely spaced narrow fingers were difficult to ablate, and frequent laser cutting generated too much debris. In order to streamline the manufacturing process and reduce the duration of the laser ablation step, two sensor electrode geometries were selected for testing: 1 mm thick fingers spaced at 0.5 mm and 1 mm, as shown in Figure 4.

After the ablation step, excess Kapton® around the conductors was removed, and the sensors were cleaned by ionized oxygen in March Plasma Treatment System (March Plasma Systems, Concord, CA), rubbed in IPA, and immersed in an ultrasonic bath. The resulting sensors are shown in Figure 5. Each sensor is composed of a pair of individual sensor electrodes. A metal substrate, 4" x 8" in size, accommodates four individual sensor electrodes of one particular design. The electrical connection to

7

sensor electrodes was made by clipping an instrument lead to a metal screw (post) connected to the terminal pad shown in Figure 2. Two pairs of sensor electrodes (4 sensor electrodes per panel) with different spacings between conductive fingers are shown in Figure 6. The width of the fingers for both Wide and Narrow sensors is 1 mm. The fingers are spaced apart by 500 µm for the Narrow sensor, and 1000 µm for the Wide. The sensing area of each sensor electrodes is 16 x 16 mm^2. After the application of the top-coat, two areas of interested (marked by circles in Figure 3) were identified on the surface of the coated specimen. The area between Sensor electrodes 1 and 3 was scribed using Gravostar engraving machine (Gravostar USA, Chillicothe, OH). This exposure area will be referred to as Scribed, while the area between Sensors 2 and 4 remained intact and will be referred to as Non-scribed. Such experimental setup differs from the earlier approach that subjects the entire panel to electrolyte attack. Incorporation of glass cylinders to carry out constant immersion exposure ensures that any degradation experienced by the sensors will come from a defect area through the coating along the plane of the substrate (longitudinal diffusion) vs. ingress of electrolyte through the top-coat directly above the sensor. The former arrangement reflects field conditions more accurately.

Electrochemical Tests

In order to investigate the feasibility of the new flexible circuit sensor electrodes, series of electrochemical tests were performed on the embedded sensors both in 2-electrode and 3-electrode cell configurations. For simplicity, the individual sensors in positions 1, 2, 3, and 4 in Figure 3 (b) will be referred to as Sensor 1, Sensor 2, etc. During off-test time, both glass cells were filled with DHS. During electrochemical tests, the solution was drained from the cell that was not being investigated. The cells were allowed at least an hour for the open circuit potential to reach steady state for the cell under test, and for the solution to dry out in the case of the other cell. The 3-electrode setup was utilized to measure the response of individual sensor, while the 2-electrode approach was used to make sensor-to-sensor measurements, as described in the Experimental section. During EIS tests, it as noted that the difference in electrochemical responses from the sensor electrodes with wide and narrow spacings were within 5-

8

7%. Given the much greater fluctuation of impedance response as function of time, only one value for each electrochemical parameter is reported. For the purposes of this discussion, both Narrow and Wide sensors will be referred to as Sensor, followed by the numeric designation based on the sensor position on the test panel.

The open circuit potential was measured before each EIS test to ascertain that the system had had adequate time to equilibrate before the measurement. In addition, open circuit potential is a very important parameter for monitoring corrosion of metal-rich primers, as it provides information about the electrochemical state of the system.

For the non-scribed panels, the decrease of E_{oc} with time is indicative of gradual progression of corrosion, as seen in Figure 7. For the specimens without a top-coat, the E_{oc} would typically reach the corrosion potential of Mg alloy over time. However, for top-coated panels, the E_{oc} is typically several hundred millivolt higher. The overall E_{oc} of the entire panel, labeled as Panel on the graph in Figure 7, decreases with immersion time. However, Sensor 4, which is located near the non-scribed area, while exhibits the same trend as E_{oc} for Panel, shows E_{oc} values 200-300 mV higher than for Panel. This is explained by the fact that E_{oc} is measured over non-exposed area across dry Mg-rich primer. The distance between the SCE reference electrode and Sensor 4 is about 2 inches, whereas E_{oc} for Panel is measured between the reference electrode in the non-exposed sell through the 40-µm layer of MRP.

In the 2-electrode setup (sensor-to-sensor, S1-S4 and S3-S4), a different trend is observed for E_{oc} as a function of immersion time. The E_{oc} decreases at first, followed by a gradual increase after one month of immersion. While the absolute values of E_{oc} are meaningless in this instance, as there is no actual reference electrode employed in this setup, the trend shown in Figure 7 can be explained by at least one electrode (Sensor 1) being in the vicinity of a scribed area which had suffered from corrosion. Therefore, the E_{oc} decrease and subsequent increase follow the expected E_{oc} behavior of MRP systems. The increase in E_{oc} is related to the accumulation of corrosion products in the area adjacent to Sensor 1. It is also possible that Sensor 1 is 'shorting' through the substrate, in which case it is electrically connected to the scribe site.

9

For the un-scribed system, the E_{oc} for Panel and sensor-to-sensor 2E pairs show a trend towards more positive values as immersion progresses, as seen in Figure 8. This behavior is characteristic of active metal corrosion and protective action of MRP. The initially low values of E_{oc} indicate that by the time the first measurement is made on the system, it is already corroding. Upon further exposure to DHS, the corrosion products formed by the dissolving Mg pigment result in a formation of a passive layer that gives rise to impedance modulus and E_{oc}. For Sensor 4, however, the observed E_{oc} trend is reverse and parallels that of the un-scribed specimen. This could be explained that Sensor 4 is not electrically connected to the site of the scribe, and thus its E_{oc} response is unaffected by this defect. For Sensor 5, E_{oc} trends for scribed and un-scribed areas are remarkably similar.

Figures 9 and 10 show the low-frequency impedance moduli measured at 10 mHz frequency. The low-frequency impedance modulus $|Z_{10\ mHz}|$ for the non-scribed site is displayed in Figure 9. For brevity, the notation $|Z_{10\ mHz}|$ will be replaced by $|Z|$ from this point on. For the entire panel, the $|Z|$ measured in a 3-electrode setup decreased with time. This observation is consistent with the shift in E_{oc} towards more negative values. The entire panel is gradually losing its barrier properties, thus $|Z|$ decreases from 2 x 10^9 Ω cm^2 to 5 x 10^8 Ω cm^2, an order of magnitude over the period of 2 months of constant immersion. For the 2-electrode arrangements, EIS response of individual sensors (3 and 4) follow the trend for the entire Panel. However, $|Z|$ values for Sensor 4 are almost an order of magnitude higher than those for Sensor 3. This is the result of the Sensor 4 being more distant from the defect on the panel.

In the case of the scribed area, $|Z|$ for the entire panel and Sensor 3 increases slightly over the 2 months immersion period (Figure 10). This observation is consistent with the E_{oc} trend. The formation of a passive layer of corrosion products results in a slight increase in the low-frequency modulus. Sensor 3 is close to the scribe area, and therefore its response is expected to parallel that of the overall panel when measured at the scribe.

10

|Z| values for Sensor-to-Sensor arrangements (S1-S4 and S3-S4) and Sensor 4 remain virtually unchanged with time, yet slight increase is observed after a 3-week mark. The observed trend is due to Sensor 4 not being affected by the corrosion processes taking place at the scribe. The values for sensor-to-sensor configurations and Sensor 4 are 3 orders of magnitude higher than those for the entire Panel and Sensor 3, which is explained by Sensor 4 not being in electrical contact with the corroding area at the scribe.

Based on the above results, it can be said that flexible circuit sensor is suitable for monitoring corrosion protective activity of Mg-rich primers. The electrochemical response detected through this sensor is influenced to the great degree by the area immediately surrounding the sensor when used in a 2-electrode, sensor-to-sensor configuration. However, this is viewed as rather the limitation of the electrochemical impedance technique than the sensor itself.

4. Conclusions

A new flexible circuit sensor electrode was designed at NDSU Center for Nanoscale Science and Engineering. Such electrode is robust and reproducible, while at the same being thin, flexible, and adaptable to various field applications. The shape and size of the sensor can be easily changed by creating the appropriate shadow mask for metal deposition. The sensors are not limited to the use of platinum or other expensive metals. However, selection of materials for the conductive aspect of the sensor must conform to the requirements of a particular application. The use of platinum in this design was dictated by its superior conductivity at nanometer thicknesses and by the available of experimental electrochemical data for embedded sensors for Mg-rich primers. The Mg-rich primer and polyurethane top-coat system was applied onto AA2024-T3 substrates, and platinum circuit sensors were embedded between the primer and the topcoat. It was found that EIS *in situ* monitoring could be conducted with embedded sensors under constant immersion conditions. The two-electrode EIS configuration is suitable for tracking changes in open circuit potential. Electrochemical signal detected by the sensors tracks

11

the response from the entire test specimen rather than localized areas of interest. However, this appears to be a limitation inherent to electrochemical impedance spectroscopy in general.
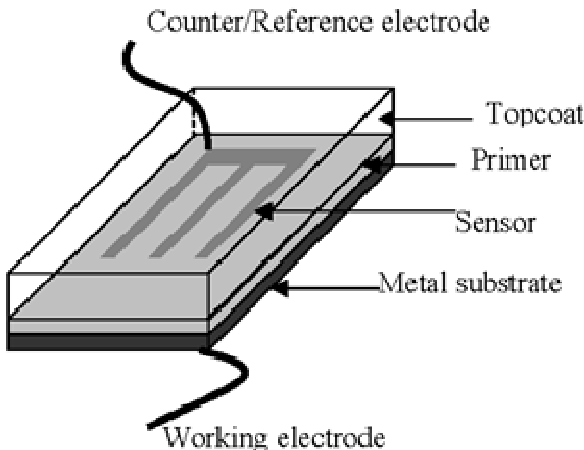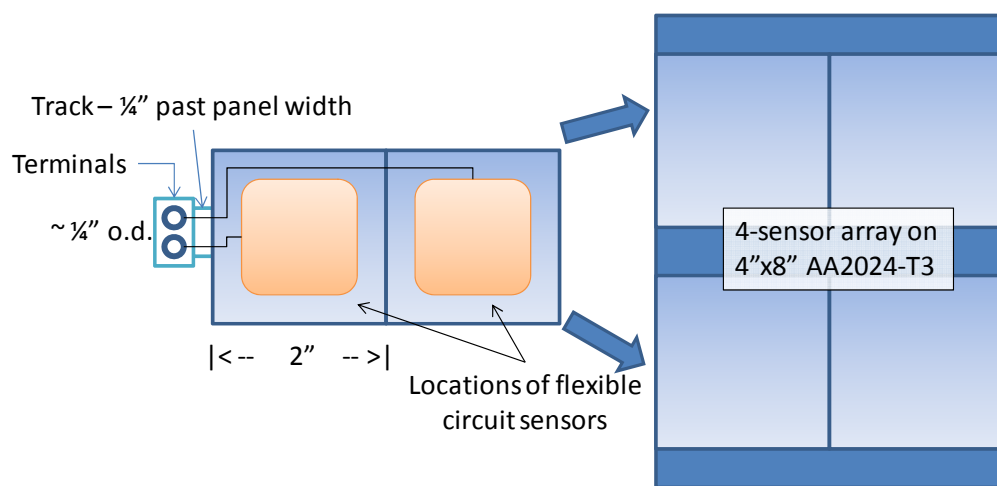
Acknowledgments

References

1. O.O. Knudsen, U. Steinsmo, and M. Bjordal, *Progress in Organic Coatings* **2005,** 54, 224-229.

2. EPA Federal Register 12.4, 60, No. 170, 1995, 45947.

3. D. Battocchi, D., Simo, A.M., Tallman, D.E. and Bierwagen, G.P., Corrosion Science 48, 2006, 1292–1306.

4. D. Battocchi, D., Simo, A.M., Tallman, D.E. and Bierwagen, G.P Corrosion Science 48 (2006) 2226–2240.

5. Nanna, M. E.; Bierwagen, G. P., *JCT Research* **2004,** 1, 69-80.

6. Bierwagen, G. P.; Nanna, M. E.; Battocchi, D. Magnesium rich coatings and coating systems. 2004-US33089, 2005051551, 20041007. 2005.

7. Bierwagen, G.; Tallman, D.; Nanna, M.; Battocchi, D.; Stamness, A.; Gelling, V. J., *Polymer Preprints (American Chemical Society, Division of Polymer Chemistry)* **2004,** 45, 144-145.

8. Bierwagen, G.; Battocchi, D.; Simoes, A.; Stamness, A.; Tallman, D., *Progress in Organic Coatings* **2007,** 59, 172-178.

9. J. Kittel, N. Celati, M. Keddam, H. Takenouti, *New methods for the study of organic coatings by EIS. New insights into attached and free films*, Prog. Org. Coat., **2001**, 41, 93.

10. J. Kittel, N. Celati, M. Keddam, H. Takenouti, *Influence of the coating-substrate interactions on the corrosion protection: characterisation by impedance spectroscopy of the inner and outer parts of a coatin*g, Prog. Org. Coat., **2003**, 46, 135.
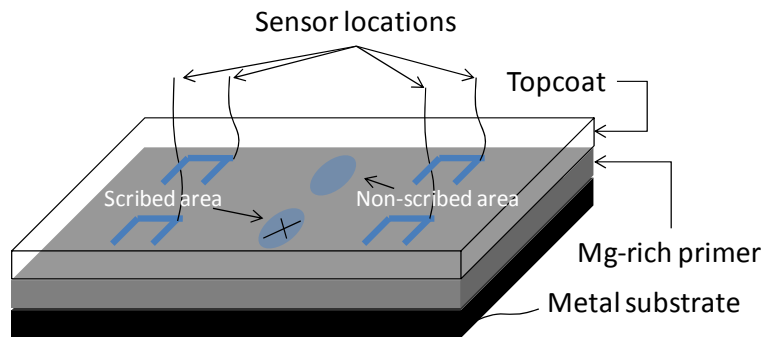
12

11. Miszcyk, T. Schauer, *Electrochemical approach to evaluate the interlayer adhesion of organic coatings*, Prog. Org. Coat., **2005**, 52, 289.

12. K. N. Allahar, Quan Su, G. P. Bierwagen, D. Battocchi, V. J. Gelling, D.E. Tallman, *Examination of the feasibility of the use of in-situ corrosion sensors in army vehicles*, submitted to Proc. 2005 Tri-services Corrosion Conference, Orlando, FL **2005**.

13. K. Allahar, Q. Su, G. Bierwagen, D. Battocchi, V. Gelling, D. Tallman, *Further Studies of Embedded Electrodes for In-Situ Measurement of Corrosion Protective Properties of Organic Coatings*, NACE Corrosion/2006 Conference, March **2006**, San Diego CA.

14. K. Allahar, Quan, Su, G. P. Bierwagen, D. Battocchi, V. J. Gelling and D. Tallman, "Examination of the Feasibility of the Use of In-situ Corrosion Sensors in Army Vehicles", **2005** Tri-service Corrosion Conference, Orlando, FL.

15. K. Allahar, Quan, Su, G. P. Bierwagen, "Monitoring of the AC-DC-AC Degradation of Organic Coatings by Embedded Sensors", NACE Corrosion **2007** Conference, Nashville, TN.

16. M. Nanna and G. P. Bierwagen. *Journal of Coatings Technology*, April, **2004**, 1, 52.

17. *Impedance Spectroscopy*, MacDonald, J.R., ed., Wiley-Interscience: New York, NY, p. 260-308, 1987.

18. *Principles and Prevention of Corrosion*, Jones, D.A., ed.; Macmillian Publ. Comp.: New York, NY, p. 122, 161, 1992.
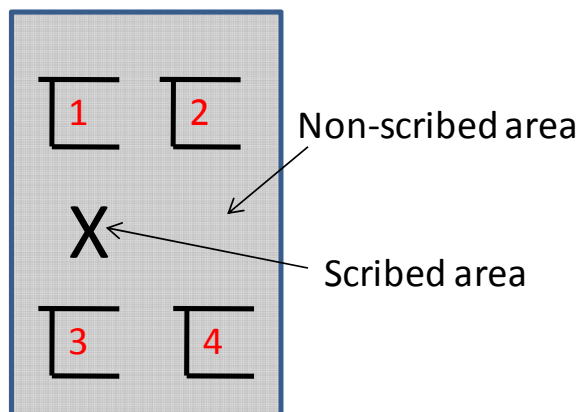
List of Figures

14

Counter/Reference electrode

Topcoat

Primer

Sensor

Metal substrate

Working electrode

15

Track – ¼" past panel width

Terminals

~ ¼" o.d.

|< --   2"   -- >|

Locations of flexible
circuit sensors

4-sensor array on
4"x8" AA2024-T3

16

(a)

(b)

17

16 mm

16 mm

x=1000 µm
y=500 µm

x=1000 µm
y=1000 µm

x y

x y

18

Narrow gap

Wide gap

20

A New Technique for Electrochemical Impedance Spectroscopy based Coating Evaluation

Yulong Shi, Duhuan Wang, and Chao You, *Member, IEEE*

Abstract—One of the traditional methods for coating evaluation is using Electrochemical Impedance Spectroscopy (EIS). This paper presents a new sensor system based on EIS evaluation. The sensor node is less than a business card in size. Evaluation time is less than 10 seconds in the operation frequency range between 20 - 90 kHz. Three coated panels were used for testing. Testing results are presented for both EIS and this new technique. Good correlations indicate this new technique is valid for impedance based measurement. The circuit is powered by batteries with l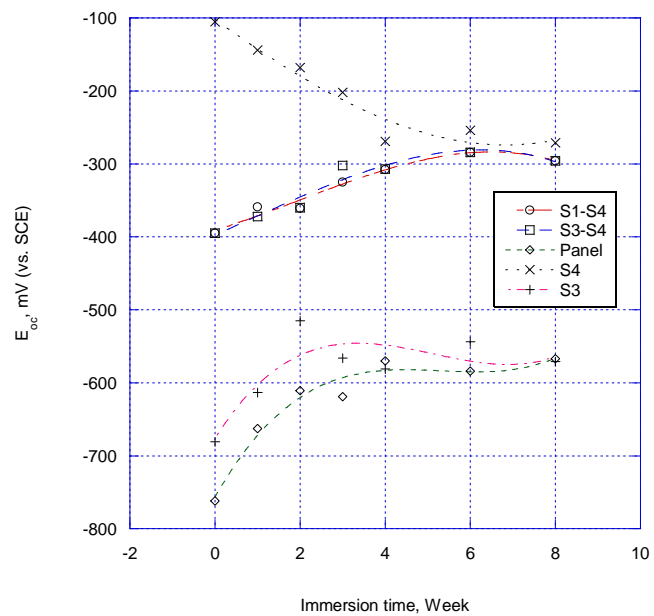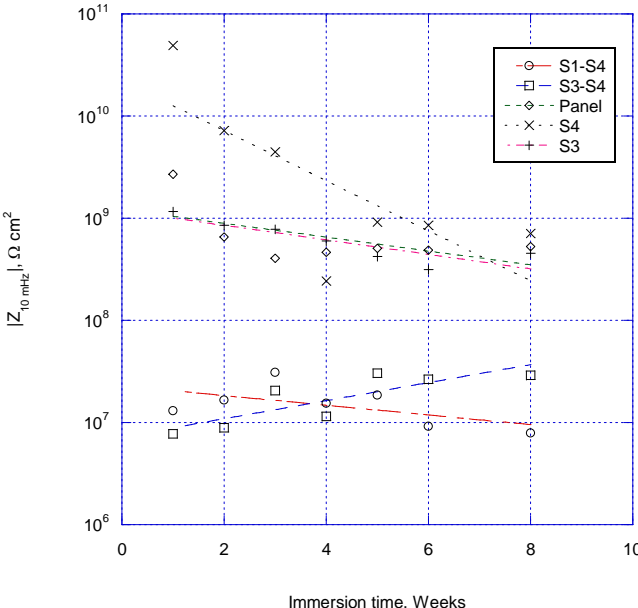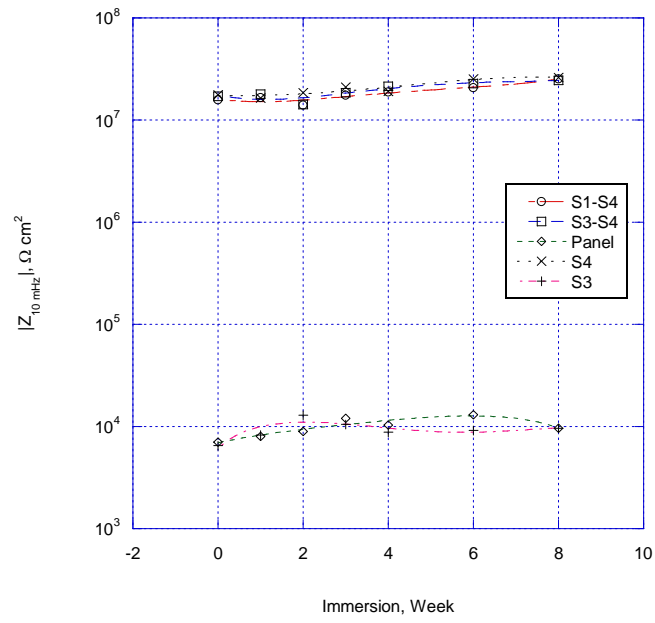ow power consumption (225 mW). A silicon-integrated version of this system will enable real-time, in field EIS coating evaluation in the near future.

Index Terms—impedance, frequency, monitoring, Microcontrollers

I. INTRODUCTION

COATINGS, as a major approach for surface protection of a structure, play an important role in our real life. Traditionally, coating has been treated as a barrier for metallic structures, reducing the transport of water, ions, and oxygen from the environment to the substrate [1]. Most of the time, corrosion begins as moisture penetrates the protective barrier of a structure, starting an electrochemical process over time which leads to surface pitting. Combined with mechanical stress, the pitted surface of a structure can cause advanced damage such as crack, fracture, deformation, etc [2]. Coating evaluation by providing feedback information about the protectiveness of coatings can ensure coatings operate at their most "healthy" status. This can greatly increase the safety of the structures under the coatings.

EIS is a technique for evaluating protective performance of the coatings. EIS analysis considers the model of the coatings consists of the combination of resistors and capacitors in serial and/or parallel. The impedance of a coating reflects coating performance. Coating evaluation can be approached by measuring coating impedance under a frequency excitation. The coating performance change results coating impedance variation [3]. Generally, the frequency range used for EIS is from 0.1 Hz to 100 kHz. A coating with the impedance greater than 10^9 Ω/cm^2 at 0.1 Hz can be considered to provide excellent corrosion protection, those possessing impedance lower than 10^6 Ω/cm^2 at 0.1 Hz are said to be a poor state in corrosion protection [4]. The selection of impedance at 0.1 Hz presents a compromise between analysis and selection of a

frequency where different coating performance can be easily distinguished. However, this selection of measuring impedance at 0.1 Hz is arbitrary and requires a long measuring time [5]. EIS requires three electrodes connected to the coating. It is not conducive to real time evaluation in the field, because the requirement of a three-probe electrochemical cell and the electrical connection to the substrate are very expensive [1]. In addition, the evaluation time for EIS lasts about 20 minutes. It is not efficient for coating evaluation.

This paper presents a new Coating Evaluation Sensor System (CESS) for coating evaluation designed by our group. The CESS is designed based on programming a microcontroller. CESS generates its own frequency excitation then apply to the coating sample through a resistor. The impedance response can be obtained and processed by the microcontroller. Then the CESS sends the data to PC through wireless communication. Advantages of the CESS includes: low cost, low power consumption. small size, fast evaluation time and long distance remote operation. With the sensor network to be realized in the future, multi-location coating evaluation can be handled simultaneously.

II. THEORETICAL BACKGROUND

Degradation of protection capability in a coating can be reflected by impedance variation in a frequency range. Therefore, the theory used in this work is to measure the equivalent impedance between the substrate and the coating in a frequency range.

Fig.1 shows a simplified model of the impedance measurement. A coating sample is immersed in an accelerated corrosive immersion environment. The frequency sweep with peak voltage V_{in} is applied to the coating through a resistor. The peak voltage and wave shape after the resistor will change due to the complex electronic model of the coating.

To measure the equivalent impedance of the coating, simple voltage division theory is used. An approximatively equivalent impedance Z_{eq} can be calculated by known peak voltage V_{in} of the frequency sweep, known resistor value R and measured output voltage V_{out}. Because of capacitive component in the coatings, different frequencies will result different Z_{eq}. Following equation shows the impendance calcualtion.

$$\frac{V_{in} - V_{out}}{R} = \frac{V_{out}}{Z_{eq}} \qquad (1)$$

Equivalent impedance of the coating Z_{eq} can be calculated from the Equation 1. The resistance R of the resistor in this work can be adjusted to meet variable impedance of different coating materials.

Y. Shi, with Dept. of Electrical & Computer Engineering, North Dakota State University, Fargo, ND 58105. Email:Yulong.Shi@ndsu.edu.

D. Wang is with Dept. of Coatings & Polymeric Materials , North Dakota State University, Fargo, ND 58105. Email:Duhua.Wang@ndsu.edu.

C.You is with Dept. of Electrical & Computer Engineering, North Dakota State University, Fargo, ND 58105. Email:Chao.You@ndsu.edu.
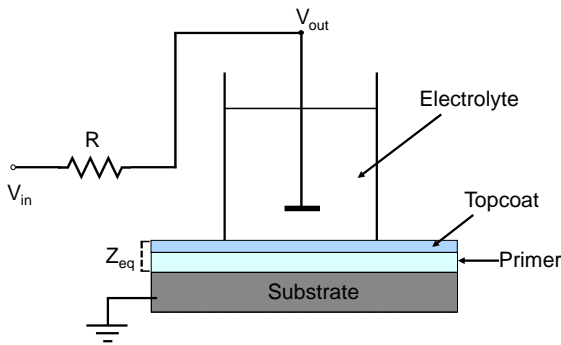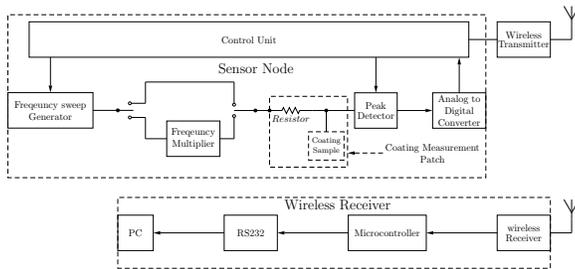
Fig. 1. Simplified model of coating measurement.

Fig. 2. Block diagram of the proposed circuit.

Fig. 3. Actual size of the sensor node.

The peak voltage V_{in} used in this work is 4.80 V. Coating failure is not accelerated by selected V_{in} since the coating evlauation process is only last few seconds [6]. EIS use frequency range from 0.1 Hz to 100 kHz. However, lower frequency requires longer evaluation time [5]. The frequency range used in this work is from 20 kHz to 90 kHz. The extent of coating degradation is proportional to the impedance variation, the relative impedance variation trend can provide enough information on tracking coating performance. Although the coating impedance at 0.1 Hz frequency excitation is popular in EIS evaluation, impedance response in high frequency also valid for coating evaluation purpose. In addition, higher frequency provides faster evaluation time which is hard to be approched in low frequency coating evaluation.

III. DESCRIPTION OF THE CESS

The CESS includes a sensor node and a wireless receiver. Fig. 2 shows a block diagram of the CESS. The sensor node consists of five parts: a frequency sweep generator (FSG), a frequency multiplier, a peak detector, an analog to digital converter (ADC), a control unit and a wireless transmitter. The wireless receiver consists of a wireless receiver chip, a microcontroller and a RS232. The proposed CESS was realized on the Printed Circuit Board (PCB). The size of the sensor node is smaller than a business card. Fig. 3 shows the actual size of the sensor node.

The idea of CESS design based on programming a microcontroller greatly reduces the CESS prototype size since a microcontroller can grealty reduce the size of CESS since a microcontroll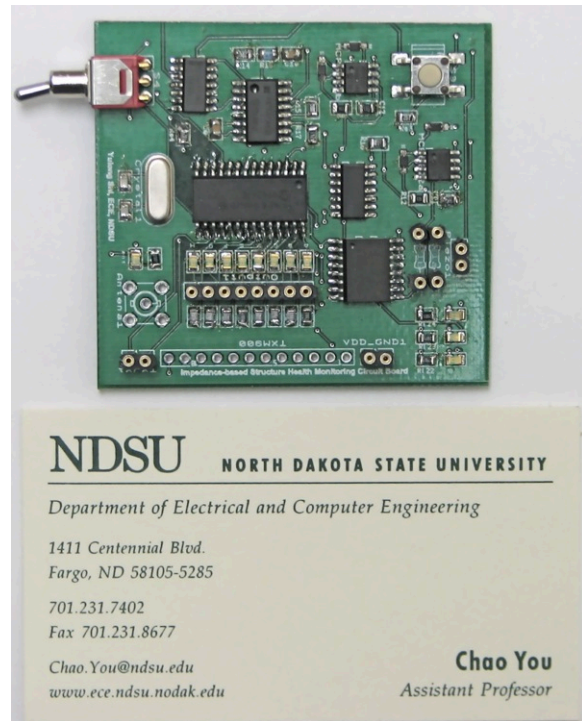er can perform fucntions such as ADC, timer controlling, data flow control and interface with other circuits and systems [7].

The FSG generates a frequency sweep. A frequency multiplier can multiply the frequency range from the FSG. Based on the internal configuration, the frequency multiplier can multiply the frequency range by $\times 2$, $\times 4$, and $\times 12$ for different measurement purposes. The frequency sweep is applied to the coating through a resistor. A peak detector tracks the peak value between resistor and the coating. An ADC reads the voltage value at the output of the peak detector and converts to binary data. Then ADC sends the binary data to the control unit. The control unit sends the data to a PC through wireless communication. After the binary data were sent to a PC, the control unit will generate a signal to reset the ADC and the peak detector, and increase the frequency of the FSG to repeat a new measurement cycle.

A. Design of Core Parts of the CESS

The FSG is designed based on programming a microcontroller (PIC16F876). The microcontroller has 3 internal timers. By programming the timer, the microcontroller can drive an I/O pin of the microcontroller high or low at a precision controlled time [8]. The frequency sweep can be generated by interrupting the program then toggling an I/O pin after the timer counts to a certain time event. According to the microcontroller datasheet, Equation 2 shows the relation between the frequency and the time events.

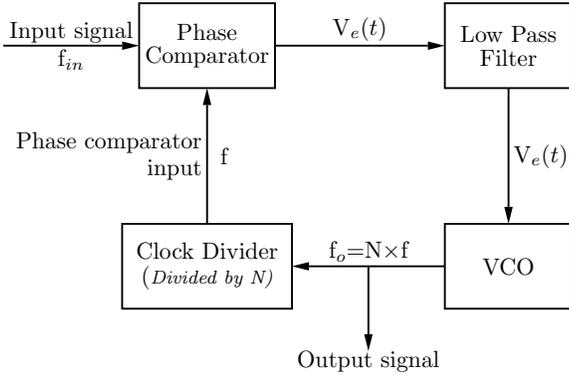$$F_q = \frac{5,000,000}{2 \times N} \qquad (2)$$

Fig. 4.   Illustration of the frequency multiplier desgin.

F_q is the output frequency. N is the time event. As an example, a 30 kHz frequency can be obtained by setting N is equal to 83. A continues changing events N can results a continues changing frequency F_q.

Commercial Intergrated Circuit (IC) chip CD4046B is a phase lock loop device. It can be functioned as a frequency multiplier by inserting a clock divider into the feed back loop [9].

Fig.4 illustrates the frequency multiplier design. The error voltage $V_{e(t)}$ generated by the difference between input signal f_{in} and phase comparator input f. $V_{e(t)}$ results a corresponding frequency through voltage controlled oscillator (VCO). The clock divider can magnify the frequency based on the division factor N. After the entire loop is in a lock state, The magnified frequency can be obtained. A buffer is needed to reduce the influence from the coating measurement patch.

A peak detector tracks the peak value between the resistor and the coating then convert the peak value to a DC signal.

A 10-bit ADC is used to convert the DC signal at the output of the peak detector to a digital number. The ADC is designed based on the internal Analog to Digital Converter Module (ADCM) of the microcontroller. The acquisition time for the ADC in PIC16F876 is 19.72 μs [8]. Therefore the sampling rate for the ADC is given by Equation3:

$$f_{sample} = \frac{1}{19.75\mu s} = 50.76kHz \qquad (3)$$

This sampling rate is fast enough since it only covert DC signal in this work.

The resolution of the ADC is:

$$\frac{5V}{2^{10}} = 4.88mV \qquad (4)$$

After converting the DC signal to digital value, ADC sends the digital value to control unit (introduced later) for further processing.

B. Data Communication

Wireless communication is realized in this work for real-time remote coating evaluation purpose. Wireless communication realizes the real-time monitoring and a data communication path between the sensor node and PC.

CS2	CS1	CS0	Channel	Frequency (MHz)
0	0	0	1	903.37
0	0	1	2	906.37
0	1	0	3	907.87
0	1	1	4	909.37
1	0	0	5	912.37
1	0	1	6	915.37
1	1	0	7	919.87
1	1	1	8	921.37

HP series transceiver (TXM-900-HP3-PPO and RXM-900-HP3-PPO) is used in this work to realize wireless communication. The reason for selecting this transceiver is that the HP series transceiver provides 8 parallel, 100 serial user-selectable channels. The usable range is up to 1,000 feet. These features make multi-location evaluation possible in the future work. The HP series transceiver also has power down feature which can be used for power saving purpose. The transceiver is controlled by the microcontroller.

CS0, CS1, and CS2 are channel selection port of the transmitter and receiver. Different combinations of the channel selection port result different transmission frequencies. One frequency represents a transmission channel. Table I shows the parallel channel selection. The radio frequency is from 903.37 to 921.37 MHz. Only in the same frequency, the transmitter and the receiver can communicate with each other. Therefore, same setting for CS0, CS1 and CS2 is required.

Once the data containing impedance and frequency information is ready in the circuit, the microcontroller will send the data the transmitter for communication. The receiver circuit receives the data and transfers the data to the microcontroller in the receiver circuit. Then the microcontroller sends the data to the PC through a standard RS 232 serial port (shown in Fig. 2) for further data processing.

C. Control Unit and Overall Operation

The control unit in the circuit is constructed by the microcontroller. The main functions of the control unit are to increase the frequency of the frequency sweep generator, to reset devices in the sensor node, to shutoff the wireless transceiver when there is no data communication needed, and to collect and process data.

When the power is on, the frequency sweep generator starts to generate the frequency sweep with the original frequency (40 Hz). User can select to multiply or not to multiply the frequency by a two way contact switch (shown in Fig. 2). Then the control unit will connect or disconnect the FSG with the frequency multiplier. The frequency will apply to the coating sample through a resistor. The peak detector reads the peak value between the resistor and the coating. The ADC reads the output of the peak detector and converts the analog value to a digital value then sends to the control unit. The control unit will process the voltage data and calculate the impedance data then send to wireless transmitter for communication. Once the receiver received data, the control unit will increase frequency of the frequency sweep generator to repeat the measurement cycle.

TABLE II
COATING SAMPLE THICKNESS

Coating System	Primer Thickness (μm)	Total Thickness(μm)
Epon + ANAC	25+50	75$\pm$5
MRP	50	50$\pm$3
MRP +ANAC	50+50	100$\pm$6

The control unit also can send a request to the wireless transceiver to active the power down feature. This ensures the circuit run in a low power consumption mode.

The cost of the circuit is approximately 80 dollars including manufacture cost. Compared to EIS (4000 dollars), the proposed circuit is very low cost. The circuit is powered by three1.5 V AAA size batteries. The power consumption is 4.5V$\times$50mA=225 mW. The circuit has a high efficiency for measurement, one complete coating measurement takes about 10 seconds.

IV. EXPERIMENTS

The experiment aims to show the impedance response of the coating sample under a frequency range in terms of the corrosion extent. Three coating systems were tested: Epoxy primer with Akzo Nobel Aerospace Coating (ANAC) topcoat, Magnesium-Rich Primer (MRP), and MRP with ANAC topcoat. These coating systems were also tested by the EIS for data comparison purpose. Since the systematic error in CESS, calibration is necessary for data processing. After calibration, similar results obtained by EIS and CESS demonstrate the feasibility of the the CESS.

A. Coating Pannels Preparation

Aluminum (Al) alloy 2024-T3 panels, supplied by Q-panel Lab Products of Cleveland OH, were first pretreated in phosphate alcohol solution (n-butyl alcohol/iso-propyl alcohol/deionized water/phosphoric acid=35/25/22/18 (Wt%)) for 4 minutes. The panels were then rinsed with tap water until a water break free surface of the panel was obtained, rinsed again with deionized water, and lastly the panel was dried with a dry nitrogen flux. The panels were used in the experiments within 3 days after they had been pretreated.

Different organic coatings were applied to the pretreated AA 2024-T3 panels using a regular air spray gun according to the standard application procedures provided by the coating manufacturer. After the fresh coating had been air dried for 7 days, their thicknesses value were measured with an Elcometer and ready for the testing.

Three different coating systems were tested in order to have a better view and comparison between the EIS and CESS values. The 2-component Epoxy-Polyamide primer (Epon) + Akzo Nobel camouflage topcoat 5000 (ANAC) system; the Magnesium-rich primer system; the magnesium-rich primer + Akzo Nobel camouflage topcoat 5000 (ANAC). Their thicknesses were shown in Table II.

B. EIS Setup for Coating Evaluation

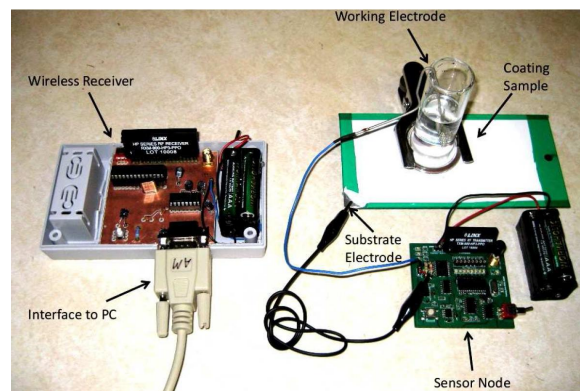EIS is used to examine the corrosion behavior of the coated Al panels by using a PC-4 instrument from Gamry.

Fig. 5.   CESS setup for coating evaluation

The samples were exposed to the Dilute Harrison's Solution (DHS), which contains 0.05% NaCl and 0.35% $(NH_4)_2SO_4$, and the exposing area was about 8 cm^2.

EIS is performed by using a three-electrode electrochemical cell, where the reference electrode was a saturated calomel electrode and the counter electrode consisted of a platinum mesh electrode and the Al panel was connected as the working electrode. The EIS instrumentation consisted of a PC4 potentiostat coupled to an eight-channel multiplexer controlled by CMS100/300 software (Gamry Instrument). Impedance measurements were carried out at in the frequency range 0.1 Hz to 100 kHz after various hours of constant immersion of samples under DHS.

C. CESS Setup for Coating Evaluation

Fig. 5 shows the experimental setup. The sensor node is connected to a coating sample. The sensor node measures the impedance of the coating sample, processes the data and sends the data to the wireless receiver. Wireless receiver receives data and sends the data to a PC through a standard RS232 serial port (Fig. 2). Both of the sensor node and wireless receiver are powered by three 1.5 V AAA batteries.

The coating sample is exposed to Dilute Harrison's Solution (DHS) for accelerated corrosion purpose. CESS has two electrodes: a substrate electrodes and a working electrode. As shown in Fig. 5, the substrate electrode is connected to the Al substrate, the working electrode is immersed in the DHS. The impedance between substrate electrode and working electrode obtained by the CESS is the approximately impedance of the coating system. Impedance of the coating in a frequency range will change depends on the corrosion extent of the coating sample. The electrodes between the DHS and the substrate can identify the impedance variation which indicates the protection performance of the coating sample.

D. Experimental Results

1) Epoxy primer + ANAC topcoat: The coating system used in this experiment comprised of an Epoxy primer beneath an ANAC topcoat. The coating system was applied to an Al plate (5$\times$5$\times$0.2 cm^3). The sample was measured by CESS and EIS. The results from the sensor node and EIS were compared.
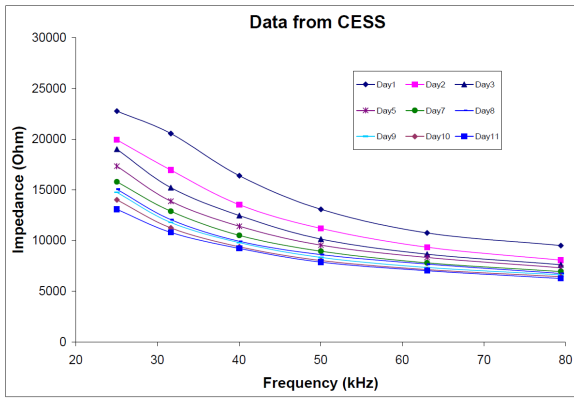
Fig. 6. Experimental result of Epoxy primer with ANAC topcoat measurement from the CESS
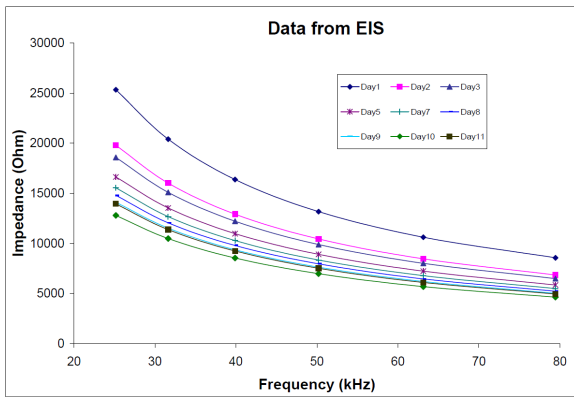

Fig. 7. Experimental result of Epoxy primer with ANAC topcoat measurement from EIS.

The frequency versus impedance plot in terms of corrosion time by CESS is show in Fig. 6. Impedance of coating sample was measured under 25 kHz, 31 kHz, 40 kHz, 50 kHz, 63 kHz, and 79 kHz. Coating sample was tested every day and the duration of the evaluation is 11 days. Same experimental condition was applied to the EIS. The result of the EIS was given in the Fig. 7.

Same impedance variation between the results from CESS and from the EIS was observed. Day 1 is the day that coating sample was immersed in the DHS. Impedance on Day1 is the original impedance for a "good" coating system. On Day 2, an obvious impedance drop in the impedance-frequency curve can be found. This means after one day immersion service in the DHS, the performance of the coating system was degraded by the DHS which results an impedance drop. In the following days, the impedance kept dropping. But the speed of the impedance decreasing is much slower compared to the first two days. In the Day 10 and Day 11, a very small impedance drop was observed. This indicates the damage of the coating system nearly to the maximum.

After calibration, the impedance variation range obtained from CESS and EIS are both from 6 kΩ to 25 kΩ approximately. Table III shows the percentage of the impedance variation from Day 1 to Day 11. The percentage of impedance
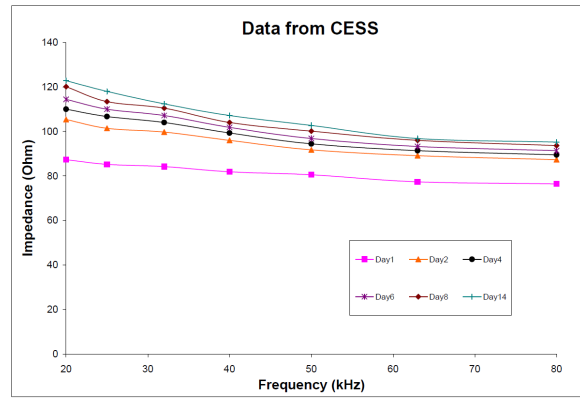

Fig. 8. Experimental result of Mg-rich primer measurement from CESS.

drop from the CESS is much closed to the results from the EIS data. The percentage of the impedance drop indicates the degradation extent of the coating system. If a threshold impedance value can be defined, a good coating system and a bad coating system can be identified from the circuit [refer to a reference].

TABLE III
COMPARISON OF IMPEDANCE VARIATION PERCENTAGE

Frequency (kHz)	Percentage from the circuit	Percentage from EIS
25	42.57	44.99
31	47.49	44.26
40	43.78	43.59
50	39.88	42.94
63	34.69	42.57
79	34.17	42.24

2) Mg-rich Primer: Mg-rich primer has been developed for the protection of the aluminum substrates. Real time monitoring of magnesium primer on an aluminum plate ($5\times5\times0.02$ cm^3) was conducted where coating was subjected to DHS exposure. Monitoring was accomplished using electrodes between substrate and primer. This sample was evaluated both by CESS and EIS.

Fig. 8 shows the impedance-frequency curve variation in terms of corrosion time plotted by CESS. Same plot obtained from the EIS is given in Fig 9. Compare with coating system consists of epoxy primer with ANAC topcoat, the impedance of the Mg-rich primer is much smaller. The reason is the Mg-rich primer has metallic particles. These particles increase the electrucal conductivity of the coating which results lower coating impedance.

To protect the Al substrate, the Mg-rich primer functions as barrier to protect the transport of water, ions, and oxygen from outside environment to substrate. In the process of protection, the magnesium particles were consumed by water, ions, and oxygen in outside evironment due to chemical reaction. This leads the impedance increment because of the reduced conductivity of the Mg-rich primer.

Compare data from CESS with data from EIS, similar impedance variation was observed. In Fig. 9, the impedance at the 48 hours is most close to the original impedance of the
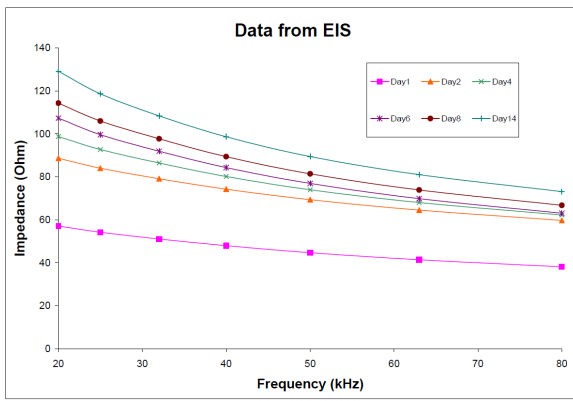
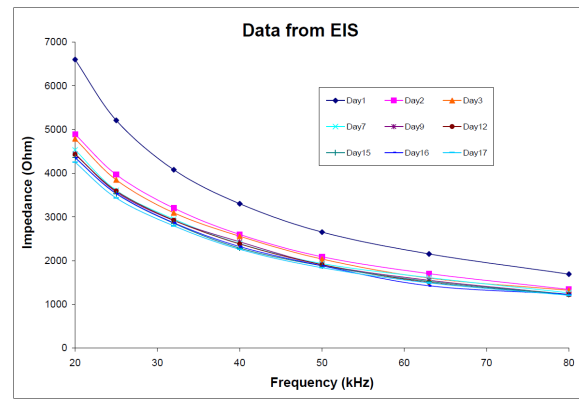Fig. 9.   Experimental result of Mg-rich primer measurement from EIS.

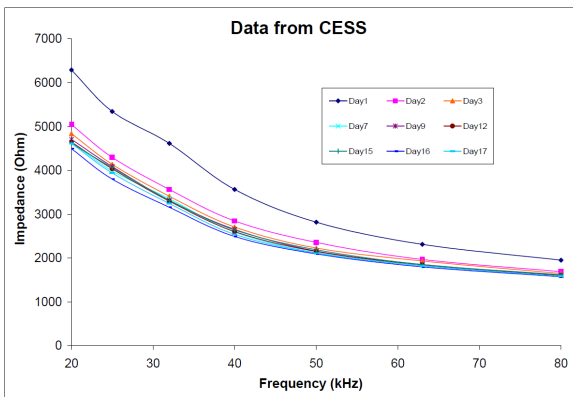Fig. 11.   Experimental result of Mg-rich primer with ANAC topcoat from EIS.

Fig. 10.   Experimental result of Mg-rich primer with ANAC topcoat from CESS.

coating (before immersed to DHS). The impedance at the 72 hours is the impedance immersed after one day. There is an obvious impedance increment between the Day 1 measurement and Day2 measurement. After Day 2, the impedance increased slowly for each measurement. After data calibration, same impedance variation and closed impedance values for EIS results and CESS results are observed.

3) Mg-rich Primer + ANAC topcoat: The third experiment in this work is testing a coating system which consists of Mg-rich primer and ANAC topcoat. The coating system applied on an aluminum plate ($10 \times 5 \times 0.02$ cm^3). The coating system was immersed in the DHS for accelerated corrosion purpose.

Fig. 10 shows the results from CESS. Fig. 11 shows the results from EIS. As the frequency increases, the impedance decreases. Same trend can be applied to all the measurement. The duration of this experiment is 17 days. The impedance trend within the frequency range of 20 kHz to 90 kHz is decreased as the immersion time increased. The impedance data at 0 hours is the original impedance before the coatings immersed into the DHS. From Day 1 to Day 2, the impedance-frequency has an obvious decrement, which means the coating was corroded critical during the first 24 hours. However, from the impedance-frequency curve from Day 2 to Day 17, only a small decrement was observed. After Day 15, the

impedance variation of the coatings almost stopped since the curve measured on Day 16 and the curver measured on on Day 17 have a obvious overlap. This can be explained as a seriously damage happened in the coating.

V. Conclusion and Future Work

A coating system is a major approach in protecting substrate corrosion in many areas. Real-time evaluation for coating performance is important in many areas, such as aircraft safety and ship safety.

In this paper, the principle of the coating evaluation, the CESS design, the coating evaluation experiment by CESS and EIS were presented. The principle of the coating evaluation in this work is measuring the impedance variation in a frequency range. Coating degradation can be indicated by coating impedance variation in a frequency range. The idea of CESS design based on programming a microcontroller allows a small size for CESS prototype. From the comparison of the experimental results from CESS and EIS, The CESS data can be used as an indication of coating system degradation. In addition, the CESS greatly reduces the evaluation cost and power consumption and provides a fast coating evaluation time as well.

In the future, the silicon-integrated version of the CESS can be realized. The size and power consumption will be further reduced. Multi-location coating evaluation can be handled simultaneously based on a wireless sensor network protocol. The CESS also can be further modified to detect damage in structures such as bridges and civil structural components with piezoelectric material [10].

References

[1] K. N. Allahar, D. Wang, D. Battocchi, G. P. Bierwagen, and S. Balbyshev, "Real-time monitoring of an air force topcoat/mg-rich primer system in b117 exposure by embedded electrode," in *Conference on Corrosion Science*, Atalanta, GA, Mar 2009.

[2] G. E. Simmers, "Impedance-based structural health monitoring to detect corrosion," Master's thesis, Virginia Polytechnic Institute and State University, May 2005.

[3] *Appliocation note: rapid electrochemical assessment of paint*, Gamry Instruments, Inc, www.gamry.com.

[4] M. O'Donoghue, R. Garrett, V. Datta, P. Roberts, and T. Aben, "Electrochemical impedance spectroscopy: testing coatings for rapid immersion service," *Materials performance*, vol. 42, no. 9, pp. 34–61, 2003.

[5] L. G. Gray and B. R. Appleman, "Eis: Electrochemical impedance spectroscopy: A tool to predict remaining coating life?" *Journal of protective coatings & linings*, vol. 20, no. 2, pp. 66–74, 2003.

[6] R. C. Bacon, J. J. Smith, and F. M. Rugg, "Electrolytic resistance in evaluating protective merit of coatings on metals," *Ind. Eng. Chem.*, vol. 40, p. 161, Jan. 1948.

[7] B. L. Grisso, L. A. Martin, and D. J. Inman, "A wireless active sensing system for impedance-based structural health monitoring," in *Proc. of 23rd inter. modal. Conf*, Orlando, FL, 2005.

[8] *PIC16F876 Datasheet*, Microchip, Inc, http://www.microchip.com/.

[9] H. L. Krauss, C. W. Bostian, and F. H. Raab, *Solid state radio engineering*. John Wiley & Sons, Mar 1980.

[10] C. P. Vera and J. Guemes, "Embedded self-sensing piezoelectric for damage detection," *Journal of Intelligent Material Systems and Structures*, vol. 9, no. 11, pp. 876–882, 1998.

Appendix D

CATHODIC PROTECTION OF AA 2024-T3 BY A MG-RICH PRIMER

Kerry N. Allahar, Dante Battocchi, Gordon P. Bierwagen
Department of Coatings and Polymeric Materials
North Dakota State University, Fargo, ND, 58105

Séva Balbyshev
Center for Nanoscale Science & Engineering,
1805 NDSU Research Park Dr., Fargo, ND 58102

ABSTRACT

Mg-rich primers are an alternate for Cr-rich primers that are currently used by the Air Force for the protection of aluminum structures. The magnesium pigments provide cathodic protection for the less active aluminum substrates and also provides a barrier type protection as the products from the Mg dissolution insulate the substrate from the environment. The cathodic protection is comparable to Zn-rich primers for steel substrates. Electrochemical impedance spectroscopic characterization of a Mg-rich primer and a standard Air Force urethane topcoat/Mg-rich primer system, both on AA 2024-T3 substrates, will be presented. The systems were exposed to constant immersion in dilute Harrison's solution. Embedded electrodes between the topcoat and primer were used to access the behavior of the Mg primer/substrate system while beneath the topcoat. Experimental results demonstrated the cathodic protection of the bare Mg-rich primer and the primer beneath a topcoat. Analysis of the EIS data by a Voigt element model was done to compare the behaviors of the bare primer and the primer beneath the topcoat. Interpretation of the data is intended to highlight the evolution of the electrochemical properties of the primer and topcoat/primer systems as the cathodic protection is reduced during the consumption of the Mg-rich pigments.

Keywords: Mg-rich primer, Cathodic protection, Embedded Sensors

INTRODUCTION

The prototype coating for the protection of aircraft structures made of aluminum alloys has been based on chromate pigments.[1,2] There are environmental implications as there is leaching of the toxic chromate due to its solubility.[3,4] Ongoing research into alternatives to the chromate based pigments is supported by Federal regulations introduced by the United States government that will curtail the use of chromate-based pigments.[5] Proposed alternative inhibitors include vanadates, phosphates, molybdates, borates and silicates[1,6-8], however the commercial non-chromate inhibitor pigments are less effective in corrosion protection than the industrial standard of $SrCrO_4$.[8]

Cathodic protection of coated aluminum alloys has been under investigation. An Al-Co-Ce metallic coating has been shown to provide cathodic protection as its open circuit potential is as much as 750 mV lower than that of AA 2024-T3 depending on the Al-Co-Ce alloy.[9,10] Release of the Co^{2+} and Ce^{3+} ions from this metallic coating provides additional inhibition of the AA 2024-T3 corrosion. A Mg-rich primer has been shown to provide cathodic protection of aluminum structures.[11-15] These primers provide cathodic protection due to the more active Mg particles compared to the Al substrate. Additionally a barrier-type protection results due to the insulation of the substrate from the environment by products of Mg hydroxide and hydroxy carbonate species that fill pores and voids.[12,16,17] The applicability of Mg-rich primers has been demonstrated by using open circuit potential evolution, potentiodynamic polarization, electrochemical impedance spectroscopy (EIS), scanning vibrating electrode technique (SVET) and scanning electrochemical microscopy (SECM).[11-15] Two and three time-constant equivalent circuit models have been used to interpret EIS data. The results were indicative of the reduction of the coating resistance and charge-transfer resistance with immersion time in 0.1% wt. NaCl.[12]

The cathodic and barrier protective modes of Mg-rich primers are similar to those that have been reported for Zn-rich primers on steel substrates.[12,13] Electrochemical methods have been used to characterize the cathodic and barrier-type protection provided by Zn-rich primers using a sophisticated transmission-line mode.[18,19] In this model parameters are attributed to the contact impedance between the particles, the impedance associated with the zinc dissolution, and the percolation resistance of the coating. The applicability of the transmission-line model for characterizing EIS data of Mg rich primers has been previously demonstrated for analyzing EIS data associated with a primer on gold and aluminum substrates under immersion in dilute Harrison's solution.[20] The consistency of the EIS data in the 1 mHz-100 kHz frequency with respect to Kramers-Kronig relationships determined by applying the measurement model technique[21-25] has been shown for the gold and aluminum substrates.

The EIS data associated with the evolution of a Mg-rich primer immersed in dilute Harrison's solution (DHS) is presented here. A Mg-rich primer would be used together with a topcoat where the topcoat would provide a barrier protection form the environment, and the primer would provide the cathodic protection. The EIS data for a topcoat/Mg-primer system (topcoat/primer) are presented here to demonstrate the influence of the topcoat. Embedded sensors were used to monitor the electrochemical behavior of the primer beneath the topcoat. These sensors have also been used to *in situ* monitor the properties of a primer beneath a topcoat during Prohesion testing using electrochemical noise method experimentation.[26] Embedded sensors in two-layer coating systems have been used for coatings subjected to thermal cycling,[27,28] for the monitoring of water uptake of a topcoat and primer simultaneously, and to determine the effect of moisture/humidity on the interlayer adhesion between a topcoat and a primer.[29-31]

EXPERIMENTAL PROCEDURE

The Mg-rich primer was applied onto an AA 2024-T3 substrate that was supplied by Q-Panel, Cleveland, OH. The primer consisted of a 10 μm average-sized Mg particulate in a two-component epoxy of Epon 828 resin and Encamide 3164 crosslinker that was supplied by Resolution Performance Products, Houston TX. The Mg particulate was supplied by Ecka-granules of America, Louisville KY. The coating was formulated at 45% pigment volume concentration that was approximately equal to the critical pigment volume concentration. The primer was applied using a compressed air spray gun to a thickness of approximately 50 μm. A drying period in excess of three days was used. A standard Air Force topcoat was used which comprised of a low gloss polyurethane topcoat (Navy MIL-C-85285B 36473, Type I). The topcoat was also applied using a compressed air spray gun to a thickness of approximately 50 μm.

The embedded electrode was made from platinum leaves that were approximately 130 nm thin. Supported by tissue paper, the platinum leaf was cut into the designed sensor shape with the surface area of the sensor being 2.56 cm^2 and the width of each side 0.4 cm. A schematic diagram of the sensor is shown in Figure 1. The sensor was adhered to the primer with an epoxy adhesive after the primer had been applied and fully cured. A copper core electrical conducting wire was soldered onto the embedded electrode after the adhesive epoxy resin had been cured. An epoxy resin was used to seal the conducting joint with this epoxy given one day at room temperature to harden. The topcoat was applied with the sensor embedded between the layers.

The experimental apparatus included a Perspex cylinder cell that exposed a 7.07 cm^2 area of the primer. The cell was clamped to the coating with an o-ring housed between the cell and the coating to prevent leakage. Three-electrode electrochemical measurements were performed with the substrate, a saturated calomel electrode and an approximate 1 cm^2 Pt mesh as the working, reference, and counter electrodes, respectively. The electrolyte was dilute Harrison's Solution (DHS) which comprised of 0.35 wt.% $(NH_4)_2SO_4$ and 0.05 wt% NaCl in distilled water. A Gamry FAS2 potentiostat was used in conjunction with EIS300 software to conduct the experiments, with both the potentiostat and the software supplied by Gamry Instruments Inc, Warminster, PA. EIS data were collected for the 100 kHz to 1 mHz frequency range with a 10 mV (rms) amplitude at 10 points per decade. The experimental procedure involved monitoring the systems under constant immersion in DHS by performing EIS experiments daily. A two-electrode configuration, as shown in Figure 2, was used for accessing the behavior of the primer beneath the topcoat where the sensor was the counter/reference electrode and the substrate was the working electrode.

RESULTS

Open Circuit Potential

The evolutions of the open circuit potential (E_{OC}) associated with the primer and topcoat/primer systems are shown in Figure 3. The E_{OC} values, as well as all the potentials reported, are relative to a standard calomel reference electrode. Values of −1.6 V and −0.6 V have been reported for the E_{OC} for the Mg particulate and the aluminum substrate, respectively.[12] An E_{OC} value between −0.6 V and −1.6 V is interpreted as a mixed potential between the Mg particulate and the substrate. The E_{OC} values for both the primer and topcoat/primer systems increased monotonically with time. Increasing values of the E_{OC} represented a decrease in the cathodic protection provided by the Mg particulate. The E_{OC} value

93

associated with the primer increased from –1.3 V to –1.0 V during the first 5 days and then from –1.0 V to –0.9 V over the next 5 days. The E_{OC} value increased from –0.9 V to –0.4 V over the next 5 days and then remained approximately at –0.4 V for the following 12 days. The E_{OC} associated with the topcoat/primer system increased from an initial value of –1.55 V to a value of –1.1 V over the first 5 days after which it increased to –0.9 V over the following 15 days. The E_{OC} value of the topcoat/primer system increased gradually from –0.9 V to –0.5 V from 20 days through 100 days after which it remained approximately at –0.5 V for the remaining immersion time.

The change in E_{OC} exhibited by the systems demonstrated the influence the topcoat has on the behavior of the Mg primer. The primer lost its cathodic protection over 15 days of immersion whereas the topcoat/primer system retained its protection until 105 days.   The changes over the initial 5 days for both systems were similar except that the E_{OC} for the topcoat/primer system started at a value of –1.5 V while the primer system started at –1.25 V after 1 day of immersion. After 5 days of immersion the E_{OC} of the primer continued to increase at a similar rate as the initial 5 days while the E_{OC} of the topcoat/primer system increased much more gradually.   There was some disparity between the E_{OC} values associated with the systems after the loss of cathodic protection with the bare Mg primer having a value of –0.4 V while the topcoat/primer system a value of –0.5 V.

EIS Results

Impedance spectra for the 0.01 Hz to 100 kHz frequency range were measured for the systems daily. Bode representations of the spectra are shown in Figure 4 with immersion time as a parameter for the primer system. The change indicated by the E_{OC} over the initial 5 days for the primer system can also be seen in this figure. The Bode magnitude plot for day 1 included a region at the high frequency end that had a slope less than –1. The slope (absolute value) decreased as the frequency was reduced in the 10 Hz to 100 Hz region. The slope in the region below 1 Hz was less than that observed for the high frequency region but there was no plateau region observable at the low frequency end. However, the trend in the data suggested that a low frequency plateau was being approached. The Bode magnitude plot for day 5 included a slope at the high frequency end also less than –1 but did not overlap the plot associated with day 1. The slope decreased as the frequency was reduced with there being an observable increase in the slope over the 1 Hz to 10 Hz region. The slope decreased at the low frequency end suggesting that a low frequency plateau was being approached. The Bode plots for days 10 through 28 overlapped. There was overlap with these days and day 5 in the high frequency end greater than 1000 Hz. In the 10 to 100 Hz region the magnitude of the data for these days was similar to that of day 5, but the trend in the data was different. In the region less than 1 Hz, the slope of the data was close to –1 and there was no observable approach to a low frequency plateau. The Bode phase angle plot for the primer highlighted the change in the EIS data with immersion time. The plot associated with day 5 was different than that of day 1 while it was similar to those associated with days 10 through 28.

Bode representations of the spectra are shown in Figure 5 with immersion time as a parameter for the topcoat/primer system. The Bode magnitude plot for day 1 included a region at the high frequency end that had a slope close to –1. The slope decreased as the frequency was reduced with the slope in the region less than 1 Hz approaching a plateau. The Bode magnitude plot for day 20 included a slope at the high frequency end also close to –1 but did not overlap the plot associated with day 1. The slope decreased as the frequency was reduced but there was no indication of a low frequency plateau being approached. The Bode plots for days 50 through 111 overlapped at the high frequency end for frequencies greater than 1000 Hz where the slope was close to -1. There was no overlap with days 1 and 20. The slopes for these data decreased as the frequency was reduced with there being no overlap in the 0.1 Hz to 200 Hz region. For frequencies less than 0.1 Hz, there was overlap among the data for these

three days with there being no approach to a low frequency plateau. The Bode phase angle plot for the topcoat/primer shown in Figure 5 highlighted the change in the EIS data with immersion time. The plot associated with day 1 was different than that of day 20 while the plots associated with days 50, 81 and 111, were similar for frequencies greater than 1000 Hz. The phase angle plot indicated that there were differences in the EIS among days 50, 81, and 111 at the low frequency end while the Bode magnitude plot suggested that the behavior was similar for these plots.

Bode representations of spectra are shown in Figure 6 with immersion time as a parameter for the topcoat/primer system measured using the embedded sensor. The Bode magnitude plot for day 1 included a region at the high frequency end that had a slope close to −1. The slope decreased as the frequency was reduced with the slope approaching a plateau, which was observable for frequencies less than 0.1 Hz. The Bode magnitude plot for days 20, 50, 81 and 111 included a slope at the high frequency end also close to −1 and overlapped. The value of the magnitude for these plots at the high frequency end was less than that for day 1 for a given frequency. The plot associated with day 20 had a slope that decreased as the frequency was reduced and a low frequency plateau was approached for frequencies less than 1 Hz. The data for days 50 and 81 were similar in the frequency range measured, with a trend suggesting that a low frequency plateau was being approached. The Bode magnitude increased with lower frequency but there was no overlap with the plots for the other days that are shown. For frequencies less than 1 kHz, a lower magnitude of |Z| was associated with a longer immersion time. The Bode phase angle plot shown in Figure 6 indicated a change in the EIS data with immersion time.

A graphical measure that is associated with EIS data of organic coatings is the low frequency modulus, which is a measure of the barrier protection provided by the coating. The frequency of 0.01 Hz was used as the low frequency modulus value with the evolution of $|Z|_{0.01Hz}$ shown as functions of immersion time and E_{OC} in Figure 7. During the first 5 days the $|Z|_{0.01Hz}$ value for the primer system increased one order of magnitude after which there was less than a factor of 2 increase over the following 23 days. The increase in one order of magnitude for the primer was associated with a change in E_{OC} from −1.2 V to −0.9 V while the small change in $|Z|_{0.01Hz}$ over the following 23 days was associated with a change from −0.9 V to −0.4 V. The $|Z|_{0.01Hz}$ value for the topcoat/primer system decreased by only a factor of 2 to approximately 10^6 Ω cm^2 over the duration of the immersion time. This change in $|Z|_{0.01Hz}$ was associated with a change in E_{OC} from −1.2 V to −0.4 V. The $|Z|_{0.01Hz}$ value for the topcoat/primer system measured from the embedded sensor increased by a factor of close to 5 to 7 x 10^6 Ω cm^2 over the first 40 days and remained close to this value for the duration of the immersion. The change over the first 40 days for $|Z|_{0.01Hz}$ was associated with a change in E_{OC} from −1.2 V to −0.8 V. The approximately constant value of $|Z|_{0.01Hz}$ after 40 days was associated with an increase in E_{OC} from −0.8 V to −0.4 V.

Equivalent circuit modeling

The measurement model technique involves using a generalized Voigt model to analyze the error associated with replicated EIS data. The model is shown in Figure 8 and consists of a series of Voigt elements comprising a parallel arrangement of a resistor R_k and capacitor C_k, in series with a resistor R_0 that represents the solution resistance. The characteristic time constant associated with a Voigt element is $\tau_k = R_k C_k$ and the impedance of the model can be expressed as[21]

$$Z = R_0 + \sum_{k=1}^{K} \frac{R_k}{1 + j\omega \tau_k} \tag{1}$$

The elements of the Voigt measurement model are consistent with Kramers-Kronig relations and the application of the technique can determine the internal consistency of the measured EIS data without need for explicit integration of the Kramers-Kronig relations.[23] The technique involves using a weighting strategy for the complex non-linear least squares regression that is based on the measured error structure associated with replicated EIS data. The technique has been described in detail for the analysis of data associated with a Mg-rich primers on gold and aluminum substrates.[20]

A 12 Voigt element model was used to fit the data associated with the primer system using a modulus weighting strategy. The resistance value of an element as a function of the time constant for the primer system is shown in Figure 9 for immersion times of day 1 and day 28. The R values for day 1 and day 28 were similar for time constants less than 0.1 s. The R values for time constants of the three largest values were significantly greater for day 28 as compared with day 1. The R values for these three time constants R_{10}, R_{11} and R_{12} are shown as functions of immersion time for the primer system in Figure 10. During the first 10 days of immersion, there were increases in R_{10} and R_{11} after which the values remained approximately constant up to day 28. The value associated with R_{12} increased during the first 15 days after which there was a small increase up to day 28.

Similar to the primer system, a 12 Voigt element model was used to fit the data associated with the EIS data obtained from the sensor embedded in the topcoat/primer system. The R values are shown as a function of time constant value for days 1 and 111 in Figure 9. There were large differences between the R values for day 1 and day 111 associated with the three largest time constants. The R values for these time constants are shown as functions of immersion time in Figure 10. The value for R_{10} and R_{11} increased up to day 40 and then remained approximately constant up to day 111. The R_{12} value increased up to day 70 after which it remained approximately constant up to day 111.

The R and τ values associated with the largest time constant were similar for both the primer system and the sensor measured topcoat/primer system. The values of R_{12} for both systems are shown as functions of E_{OC} in Figure 11. The R_{12} value for the primer increased monotonically during the increase in E_{OC} from –1.1 V to –0.85 V after which it was approximately constant until an E_{OC} of –0.55 V. For E_{OC} values from –0.55 V to –0.4 V there was an increase in the R_{12} value. The R_{12} value for the sensor measured EIS data increased monotonically during the change of E_{OC} from –1.2 V to –0.65 V after which the value remained constant up to an E_{OC} value of –0.4 V.

The cathodic protective pigmented coating systems such as Mg-rich primer and Zn-rich primer are monitored by the open circuit potential. This monitoring requires a standard reference electrode and immersion in an aqueous electrolyte and these requirements are not easily attained during field application of these primers. The feasibility of impedance measurement as a measure for the cathodic protection provided by Mg-rich primers was presented. The graphical measure of $|Z|_{0.01Hz}$ associated with the impedance at a low frequency is shown as a function of E_{OC} in Figure 7 (right) for both systems. It can be seen that the value of $|Z|_{0.01Hz}$ increased as E_{OC} increased to –0.8 V but was insensitive to the E_{OC} changing to more positive values. These results indicated that the cathodic protection provided by the Mg-rich primer was not being tracked by the $|Z|_{0.01Hz}$ parameter with the observed constant $|Z|_{0.01Hz}$ not being indicative of the loss of cathodic protection from –0.8 V to –0.4 V.

The use of the R value associated with the largest time constant that was obtained by fitting the 12 element Voigt model tracked the loss of cathodic protection, as shown in Figure 11 better than the $|Z|_{0.01Hz}$ parameter. This demonstrated the feasibility of using EIS monitoring together with embedded

sensors to monitor the protection provided by the Mg-primer beneath a topcoat. The presented results were obtained where the coating systems were under immersion. Further studies are being undertaken to determine the feasibility of sensor measured EIS to track the cathodic protection provided by the primer in non-immersion conditions.

CONCLUSIONS

The evolution of the electrochemical behavior of a Mg-rich primer and a topcoat/primer system on AA 2024-T3 was monitored using EIS experimentation. The evolution of the E_{OC} for both systems indicated the change from a mixed potential value to a value consistent with the substrate. This demonstrated the loss of the cathodic protection. The topcoat extended the time of cathodic protection of the primer. The EIS data were analyzed using a 12 element Voigt model. The results demonstrated the feasibly of monitoring the cathodic protection of a primer beneath a topcoat using EIS data acquired with an embedded sensor between the topcoat and primer. The use of the resistance value associated with the largest time constant tracked the loss of cathodic protection of both the primer and topcoat/primer systems better than the low frequency modulus parameter.

ACKNOWLEDGEMENTS

REFERENCES

1. R. Buchheit, H Guan, S. Mahajanam, F. Wong, Progress in Organic Coatings, 47(2003), p. 174.
2. C. Simpson, *Organic Coatings for Corrosion Control*, G. P. Bierwagen, Editor, ACS Symposium Series, 689(1998), p. 356.
3. Y. Suzuki, K. Fukuda, Arch. Toxicology, 64(1990), p. 169.
4. P.O. O'Brien, A. Kortenkamp, Trans. Met. Chem., 20(1995), p. 636.
5. EPA Federal Register, National Emission Standards for Hazardous Air Pollutants for Source Categories: Aerospace Manufacturing and Rework Facilities, 60(170), p. 45947, Sept. 1, 1995.
6. S. M. Cohen, Corrosion, 51(1995), p.71.
7. K.D. Ralston, S. Chrisanti, T.L. Young, R.G. Buchheit, Journal of Electrochemical Society, 155(2008), p. 350.
8. J. Sinko, Progress in Organic Coatings, 42(2001), p. 267.
9. F.J. Presuel-Moreno, M.E. Goldman, R.G. Kelly, J.R. Scully, Journal of Electrochemical Society, 152(2005), p. 302.
10. F.J. Presuel-Moreno, H. Wang, M.A. Jakab, R.G. Kelly, J.R. Scully, Journal of Electrochemical Society, 153(2006), p. 486.
11. M.E. Nanna, G.P. Bierwagen, Journal of Coating Technology Research, 1(2004), p. 69.
12. D. Battocchi, A.M. Simoes, D.E. Tallman, G.P. Bierwagen, Corrosion Science, 48(2006), p. 1292.
13. D. Battocchi, A.M. Simoes, D.E. Tallman, G.P. Bierwagen, Corrosion Science, 48(2006), p. 2226.
14. G. Bierwagen, D. Battocchi, A. Simoes, A. Stamness, D. Tallman, Progress in Organic Coatings, 59(2007), p. 172.
15. A.M. Simoes, D. Battocchi, D.E. Tallman, G.P. Bierwagen, Corrosion Science, 49(2007), p. 3838.

16. N.C. Hosking, M.A. Strom, P.H. Shipway, C.D. Rudd, Corrosion Science, 49(2007), p. 3669.
17. M. Jonsson, D. Persson, D. Thierry, Corrosion Science, 49(2007), p. 1540.
18. C.M. Abreu, M. Izquierdo, M. Keddam, X.R. Novoa, H. Takenouti, Electrochimica. Acta, 41(1996), p. 2405.
19. C.M. Abreu, M. Izquierdo, P. Merino, X.R. Novoa, C. Perez, Corrosion, 55(1999), p. 1173.
20. K. Allahar, Dante Battocchi, Gordon P. Bierwagen, Dennis E. Tallman, accepted by Journal of Electrochemical Society, 2008.
21. M.E. Orazem, Journal of Electroanalytical Chemistry, 572(2004), p. 317.
22. P. Agarwal, M.E. Orazem, L.H. Garcia-Rubio, Journal of Electrochemical Society, 139(1992), p. 1917.
23. P. Agarwal, O.D. Crisalle, M.E. Orazem, L.H. Garcia-Rubio, Journal of Electrochemical Society, 14291995), p. 4149.
24. P. Agarwal, M.E. Orazem, L.H. Garcia-Rubio, Journal of Electrochemical Society, 142(1995), p. 4159.
25. K.N. Allahar, D.P. Butt, M.E. Orazem, H.A. Chin, G. Danko, W. Ogden, R. Yungk, Electrochimica Acta, 51(2006), p. 1497.
26. G.P. Bierwagen, X. Wang, D.E. Tallman, Progress in Organic Coatings, 46(2003), p. 163.
27. G.P. Bierwagen, L. He, J. Li, L. Ellingson, D.E. Tallman, Progress in Organic Coatings, 39(2000), p. 67.
28. K. Allahar, Quan Su, G. Bierwagen, D. Battocchi, V. Johnson Gelling, D. Tallman, Tri-Services Corrosion Conference 2005, Orlando FL.
29. J. Kittel, N. Celati, M. Keddam, H. Takenouti, Progress in Organic Coatings, 41(2001), p. 93.
30. J. Kittel, N. Celati, M. Keddam, H. Takenouti, Progress in Organic Coatings, 46(2003), p. 135.
31. A. Miszcyk, T. Schauer, Progress in Organic Coatings, 52(2005), p. 298.

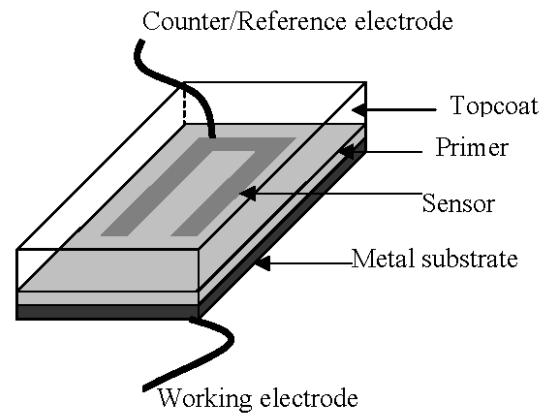**Figure 1**. Schematic diagram of embedded sensor between topcoat and primer with electrical connection.
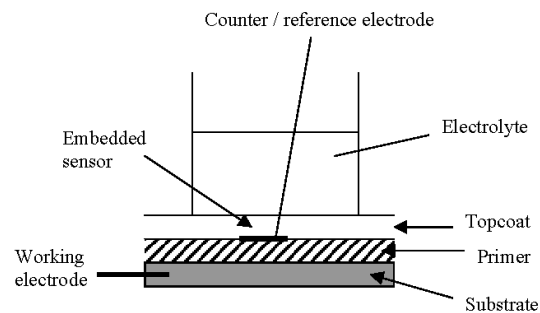

Figure 2. Schematic diagram of the experimental setup for a two-electrode EIS measurement associated with the embedded sensor. The embedded sensor was the counter/ reference electrode and the substrate was the working electrode.
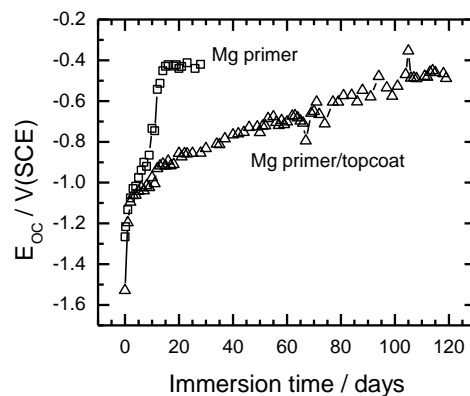

Figure 3. Open circuit potential E_{OC} associated with Mg primer and Mg primer/topcoat systems as functions of immersion time.
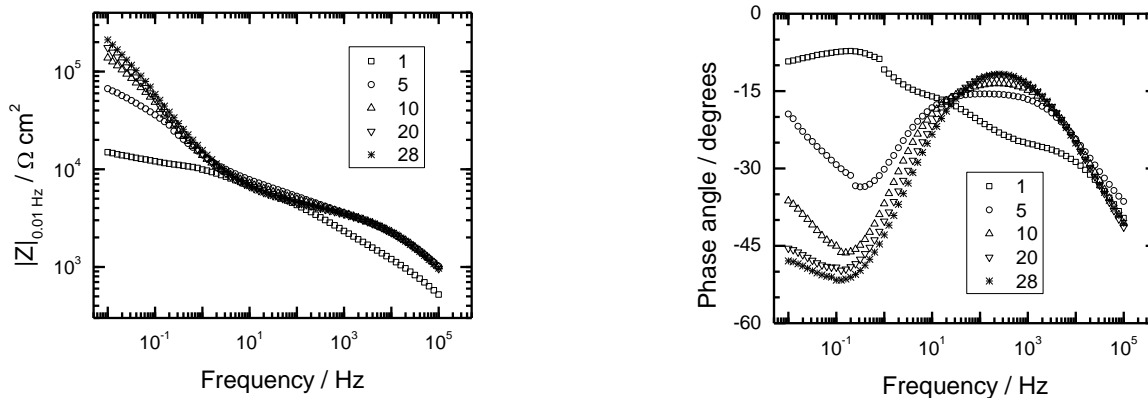
Figure 4. Bode magnitude (left) and phase angle (right) representations of EIS data associated with Mg primer immersed in DHS with immersion time as a parameter.
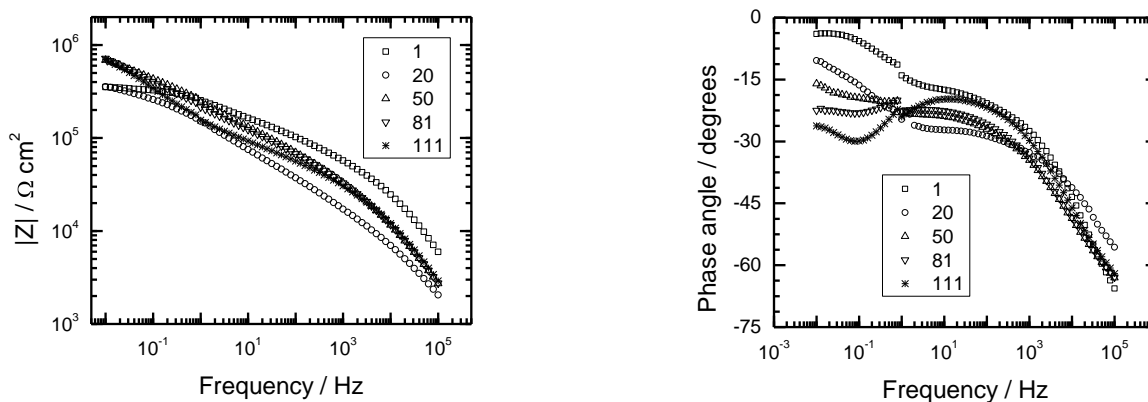

Figure 5. Bode magnitude (left) and phase angle (right) representations of EIS data associated with topcoat/primer system immersed in DHS with immersion time as a parameter.
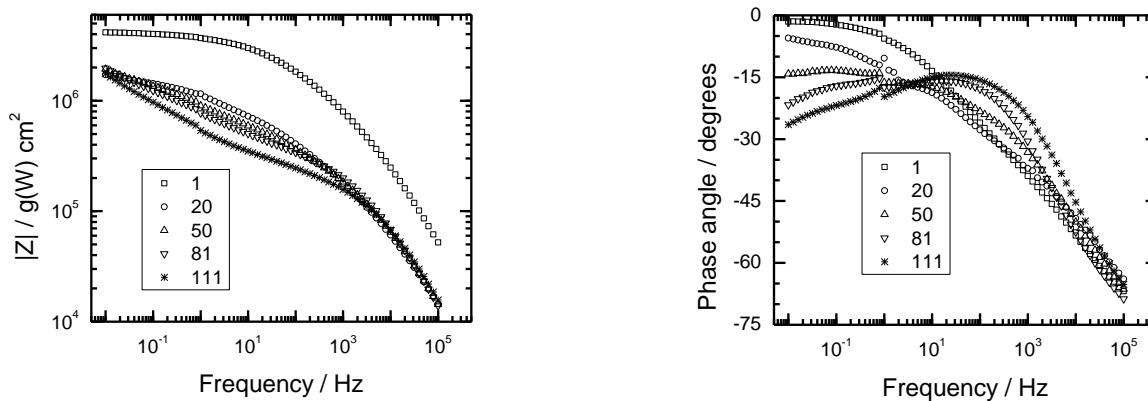
Figure 6. Bode magnitude (left) and phase angle (right) representations of EIS data associated with topcoat/primer system measured using the embedded sensor immersed in DHS with immersion time as a parameter.
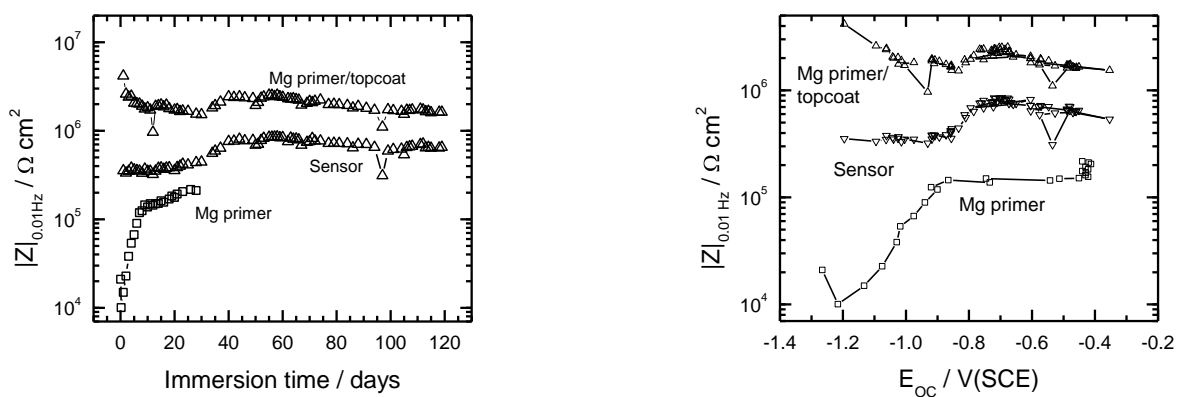

Figure 7. Low frequency modulus value of the EIS data for the Mg-primer and the topcoat/primer systems and the sensor measured topcoat/primer system as functions of immersion time (left) and open circuit potential (right).
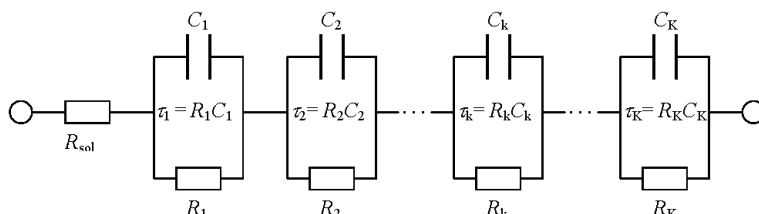

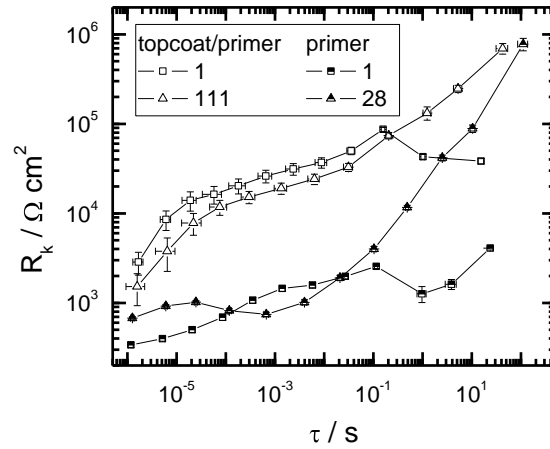**Figure 8**. A schematic representation of a Voigt measurement model.

Figure 9. The resistance parameters R_k as a function of time constant for the EIS data of the primer (and sensor measured topcoat/primer systems. The data for the former system is associated with day 1 and day 28 while the latter is associated with day 1 and day 111. The values were obtained by regressing the EIS data to a 12 element Voigt equivalent circuit.
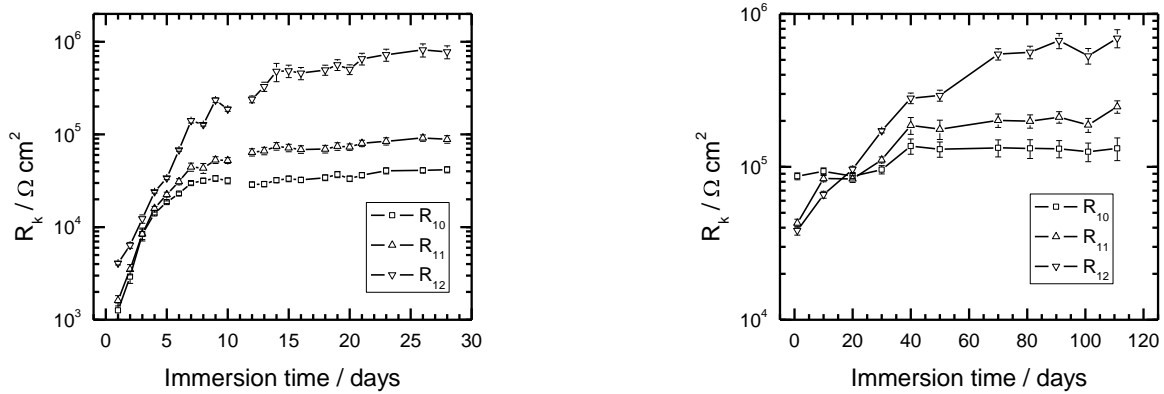

Figure 10. The resistance parameter associated with the largest three time constant R_{10}, R_{11}, and R_{12} as a functions of open circuit potential for the EIS data of the primer (left) and sensor measured topcoat/primer (right) systems. The values were obtained by regressing the EIS data to a 12 element Voigt equivalent circuit.
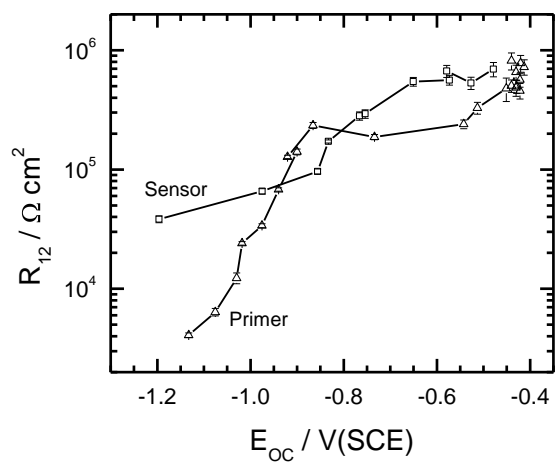
Figure 11. The resistance parameter associated with the largest time constant R_{12} as a function of open circuit potential for the EIS data of the primer and sensor measured topcoat/primer systems. The values were obtained by regressing the EIS data to a 12 element Voigt equivalent circuit.

IN SITU MONITORING OF A MG-RICH PRIMER BENEATH A TOPCOAT EXPOSED TO PROHESION CONDITIONS

Duhua Wang,[1] Dante Battocchi,[1,2] Kerry N. Allahar,[1] Seva Balbyshev[3] and
Gordon P. Bierwagen[1,2]

[1]Department of Coatings and Polymeric Materials

[2]Center for Surface Protection

[3]Center for Nanoscale Science and Engineering

NDSU Dept. 2760, P.O. Box 6050, Fargo, ND 58108-6050, USA

Ph: +1(701)231-6219

Authors e-mail: Duhua.Wang@ndsu.edu, Dante.Battocchi@ndsu.edu, Kerry.Allahar@ndsu.edu, Seva.Balbyshev@ndsu.edu, Gordon.Bierwagen@ndsu.edu,

Abstract:

Mg-rich primers have been proven to be an adequate alternative for chromate-based coatings for the protection of aluminum alloys from corrosion. Their protection behavior was attributed to a combination of cathodic and barrier protection similar to the protection behavior associated with Zn-rich primers on steel substrates.

The performance of a Mg-rich primer on aluminum 2024-T3 under Prohesion® exposure (ASTM G85) has been monitored using an embedded sensor placed at the surface of the primer and below the topcoat. The accelerated weathering cycle simulates outdoor weather exposure by alternating wet and dry steps.

Electrochemical impedance spectroscopy (EIS) and noise measurements (ENM) were conducted to monitor the performance and the electrochemical properties of the system beneath the topcoat. The data analysis demonstrates that the sensor is able to detect change in the barrier properties of the topcoat in response to the exposure conditions and the activation of the pigments in the primer in the presence of electrolyte.

Keywords: Mg-rich primer, embedded electrodes, EIS, ENM

1. Introduction

Corrosion protection by coatings is mainly based on the combination of binders (polymer resins) and pigments. For epoxy esters, drying oils and phenolic epoxy paints, the corrosion protection is mainly attributed to the barrier properties from binders, which can reduce the transport of water, ions, and oxygen from the environment to the substrate [1-3]. On the other hand, in red lead, zinc chromate yellows and zinc-rich primers, the pigments' inhibition, passivation, and cathodic protection are the main causes for reducing corrosion.

Corrosion is a natural process and the accelerated weathering, such as Prohesion® and salt spray exposure, aims to reproduce and accelerate natural corrosion and degradation processes of the coating system and the substrate without changing the corrosion/degradation mechanism as occurs in practice. The most often used accelerated test is the salt spray test, which involves continuous spraying of 5% sodium chloride (NaCl) in distilled water at 35°C [2]. It can be performed in accordance with ASTM B117, ISO 7253, ISO 9227, DIN 53167, or BS 3900. Salt spray was first used for corrosion testing around 1914. In 1939, the neutral salt spray test was standardized in ASTM B117. However, cyclic corrosion test results generally correlate better with natural corrosion than salt spray test results do. This is pointed out in many of the references [4-9]. The first cyclic test, the so-called Prohesion test, was developed in the UK in the 1970s. It is covered since 1994 in an annex of ASTM G85, together with other modifications to the basic salt spray test. A typical Prohesion test includes a fog/wet step of 1 hour salt spray at 25°C and a dry step of 1 hour hot air at 35°C. Dilute Harrison's solution (0.05 wt% NaCl and 0.35 wt%t $(NH_4)_2S0_4$ at pH=5.0-5.4) is used as the salt fog solution in the Prohesion chamber. Accelerated weathering cannot replicate the real natural corrosion process. G. Gardner pointed out that continuous salt spray accentuated blistering and that cyclic salt spray emphasized filiform and undercut corrosion [4]. Because of the problems inherent in exposure testing methods, especially their subjective nature, quantitative electrochemical testing has become a widely used alternative [10]. The major electrochemical test methods used for examining the coatings systems and metal pretreatments are electrochemical impedance spectroscopy (EIS), electrochemical noise methods (ENM), and potentiodynamic scanning (PDS). [10-15].

A technique for in-situ monitoring of coatings involves an embedded electrode sensor within a coating system. The Department of Coatings and Polymeric Materials at NDSU has been at the forefront in the development and application of embedded sensors, which consist of electrodes

2

that act as the counter and reference electrode, but are placed between the layers of a two-layer coating system [16, 17]. The major advantage of this sensor application is that the electro-chemical measurement of the primer/metal interface can be made without being masked by high resistance topcoat. Until now, the embedded sensors approach has been applied for characterization of standard Air Force and Army vehicle coatings that are evaluated by thermal cycling accelerated testing method [18], and accelerated ac-dc-ac testing method. [19] While there have been limited studies published on the use of embedded sensors in the aforementioned coating systems, there has been no application to metal rich primers, e.g. Mg- or Zn-rich primers. By analogy to the formulation of zinc-rich primers for the protection of steel, magnesium–rich, pigmented primers are now being formulated for the protection of aluminum alloys. This work motivated by the need for chromate-free alternatives for protection of high-strength aircraft Al alloys such as 2024-T3 and 7075-T6. G.P. Bierwagen and the corrosion group at NDSU are leading this Mg-rich primers research and a series of articles have been published [20-22] on their application and properties. The coupling of embedded sensors and coating systems with Mg-rich primers is a unique approach that allows in-situ monitoring of the electrochemical behavior of protective Mg-rich primers beneath a topcoat.

2. Experimental

  The protective coating system used in the experimental procedure was composed of a high solids polyurethane clear topcoat (AKZO NOBEL 646-58-7925CLEAR) and a Mg-rich primer developed at NDSU [20]. In this primer, Mg powder with the average particle size of 25 μm (Ecka Granules of America, Louisville, KY) was dispersed in a two-component epoxy-polyamide resin, and the pigment volume concentration (PVC) of the primer was 45%. The primer was applied to standard panels of aluminum alloy 2024-T3. After the application of the primer, a platinum sensor was applied on the surface of the primer, followed by the application of the polyurethane topcoat. The embedded sensor was between the primer and the topcoat for each of the final coated panels. Using the same method, the embedded sensor was placed between the primer and the topcoat of all coated panels.

2.1 Sample Preparation

3

The aluminum alloy 2024-T3 panels were polished by 200 grit followed by 600 grit sanding paper, then washed with hexane and dried with a nitrogen flow. The freshly pretreated metal panels were coated within half an hour after they were polished.

The sensor was made from platinum leaves obtained from Wrights of Lymm Ltd, Manchester, England, and was approximately 130 nm thin. Supported by tissue paper, the platinum leaf was cut into the designed sensor shape with the surface area of the sensor being 2.56 cm^2 and the width of each side 0.4 cm as shown in Figure 1 with the sensor on the surface of the Mg-rich primer and covered by a polyurethane clear topcoat.

The sensor was adhered to the primer by applying a thin layer of a homemade epoxy resin (D.E.R. 331 epoxy resin/Ancamide 2353/methyl ethyl ketone at a 5/3/5 weight ratio) to the surface of the primer. The platinum sensor was then placed on this epoxy resin and adhered onto the primer after 10 minutes of solvent flash-off and cured. A copper core insulated wire was soldered onto the embedded sensor. The same epoxy resin (D.E.R. 331) was used to seal the conducting joint and given one day to harden at room temperature before the polyurethane topcoat was applied. The approximate neat dry film thickness of Mg-rich primer was 50 μm, and 40 μm for the topcoat.

The exposure of the panels in the Prohesion chamber required that the back and the edges of the coated panel be isolated from the environment. This was done by spraying the same coating system, Mg-rich primer and polyurethane clear topcoat, to the back of the panel. The edges of the panels were dip-coated with the same coating system.

2.2 Experimental Configurations

The in-situ monitoring of the Mg-rich primer + polyurethane clear topcoat was carried out under Prohesion exposure condition. A Gamry PCI4-300 was used for the potentiostatic EIS measurements with a frequency range from 100 kHz to 0.05 Hz and a perturbation potential of 15 mV RMS. A data acquisition rate of 10 points per decade was employed. The two-electrode (2E) EIS method (sensor-substrate) was used to obtain the EIS responses in a one-panel setup, where a coated panel was assembled with two sensors placed approximately 8 cm apart. As shown in the schematic diagram in Figure 1, the working electrode was connected to the metal substrate and the reference and counter electrodes were connected to the embedded sensor.

4

Another 2E EIS setup (sensor-sensor) consisted of one sensor connected to the working electrode and the other sensor connected to the counter and reference electrodes, as show in Figure 1.

The fast data acquisition mode was used in both two-electrode EIS measurements, and frequency scans from 100 kHz to 0.05 Hz took about 12-15 minutes. The single frequency impedance measurement was also carried out using the sensor-to-sensor 2E configuration at the frequency of 10 kHz.

The configuration for the ENM measurement is shown in Figure 1. A one-panel/two sensor setup was utilized, where the two sensors acted as working electrodes and the substrate was the reference electrode. Experiments was carried out in zero resistance ammeter (ZRA) mode on a Gamry PCI4/300 potentiostat (Gamry Instruments, Inc. of Warminster, PA) coupled with Gamry ESA400 software (ver. 4.21), with the data acquisition frequency of 5 Hz. This configuration is theoretically the same as the traditional ENM three-electrode configuration [23], involving a reference electrode and two coated panels acting as two separate working electrodes electrically connected via a salt bridge. It has been shown that similar information can obtained from both the traditional and present configurations [23,24].

2.3 Testing Procedure

In order to achieve total curing, tested panels were placed under ambient conditions for at least 10 days before being placed into the Prohesion chamber. The electrical leads for the embedded sensor and the substrate were long enough to connect each panel with the potentiostat and computer located outside the chamber. After a certain period of exposure in the Prohesion chamber, EIS experiments were carried out using the two-electrode configurations during both dry and wet steps of the Prohesion protocol, followed by the ENM testing typically consisting of 3 cycles of dry and wet steps of the Prohesion test.

During the first three weeks in Prohesion chamber, EIS and ENM testing were carried out every day. After three weeks, electrochemical measurements were carried out every other day. The total duration of this experiment was 60 days.

The EIS experiments were conducted in both the dry and wet steps after 30 minutes once the chamber environment has stabilized and the coating surface has reached either dry or wet

5

condition, respectively. Additional experiments were also conducted to characterize the behavior of the Mg-rich primer during the changing environmental conditions. A single frequency experiment was conducted every other week during Prohesion exposure to characterize the capacitance behavior of the primer. This experiment involved measurement of the impedance at an applied frequency of 10 kHz over a period of time, typically 3 cycles. In addition, the temperature of the coating surface was monitored using thermocouple sensors for several early cycles of Prohesion exposure.

3. Results and Discussion

3.1 Chamber Temperature and Coating Capacitance Study

Electrochemical impedance measurements require steady state conditions during the data acquisition process. The environmental conditions in the Prohesion chamber changed rapidly with time. In order to conduct in-situ EIS measurements on the coated panels in the Prohesion chamber, a relatively stable state should be identified first. The changes of temperature and the capacitance associated with the measured panels were investigated, and the influence of Prohesion conditions on coating electrical properties was studied. Based on these findings, a proper time range was identified for the EIS test.

The temperature profile at the surface of a coated panel was measured during an early Prohesion cycle and is shown in Figure 2. The 1-hour exposure of a dry step exhibited a temperature increase from 25°C to 45°C in 20 minutes, followed by a drop to 40°C over the next 40 minutes. The 1-hour exposure of the wet (fog) step included a drop from 40°C to 27°C over the first 55 minutes with a subsequent drop to 25°C over the last 5 minutes.

The relative dielectric permittivity of water at room temperature is approximately 80, while that of an epoxy polymer is in the range of 3 to 5. The ingress of water into a coating is associated with an increase of the dielectric constant of the coating with a concomitant increase of coating's capacitance [25,26]. The evolution of the coating's impedance at high frequency (10 kHz) was measured during the dry and wet steps of the Prohesion cycle. The impedance data were used to calculate the capacitance of the coating, C_c, using:

$$C_c = -1 / (2 \pi f Z")$$

where f is the frequency and $Z"$ is the imaginary component of impedance.

The evolution of the calculated coating capacitance after 16 days of Prohesion exposure is shown in Figure 2. In the dry step, the capacitance value clearly had a profile resembling the temperature fluctuations. The capacitance increased from 0.30 nF to 0.35 nF during the first 35 minutes of the dry step and decreased to the lowest point of ~0.28 nF during the first several minutes of wet cycle. It appears that the temperature factor dominated the changes of capacitance in the dry step. With the temperature increasing, the polyurethane topcoat became more porous and thus more prone to water ingress. Conversely, it provided better barrier to moisture when the temperature decreased. In the wet step, the capacitance was maintained around 0.30 nF, most likely due to the combination of the fog spraying environment and decreasing temperature in the wet step. Overall, the capacitance changes were attributed more to the temperature changes during the dry and wet steps in Prohesion exposure. It was also found that the environmental conditions in Prohesion chamber varied all the time and the electrochemical impedance data were affected by the different chamber conditions. In order to have an effective analysis and comparison of data, we chose to present and plot the EIS data collected during the 40-50 minute range in dry and wet steps.

3.2 Open circuit potential (OCP)

The open circuit potential is a very important parameter for monitoring the behavior of metal-rich coatings. The OCP time records presented in Figure 3 were measured in-situ with the embedded sensors and ex-situ with a conventional 3 electrode setup. In this case, the embedded sensor and the ex-situ recorded values present a difference of ca. 400 mV, the embedded sensors values being more positive of the two.

3.3 EIS Results
3.3.1 Sensor-substrate EIS

Two-electrode EIS method (sensor-substrate) was used to obtain the EIS responses (Figure 1). EIS measurements for the frequency range of 100 kHz to 0.05 Hz were performed after 40 minutes of drying and wetting, respectively. Total duration of testing was 60 days when the coatings failed both by visual inspection and electrochemical testing. The EIS Bode plots during the Prohesion dry and wet steps are shown in Figure 4, as a function of exposure time. It was observed that the |Z| spectra almost superimposed in the 100 Hz to 100 kHz high-frequency

7

range up to 20 days of Prohesion exposure,. This suggested that the capacitance of the coating was approximately the same at the end of 20-day Prohesion chamber exposure. After 20 days, the high frequency value of |Z| decreased with time. The impedance in the mid-frequency range of 1Hz to 100 Hz was scattered for about 10 days, with the scatter becoming negligible as the time elapsed. The |Z| modulus value in the low frequency range of 0.05 Hz to 1 Hz was continuously decreasing until 43 days of chamber exposure. It was found that the |Z| data for days 43 and 60 almost overlapped, in both the dry and wet steps. There were plateau regions in the 0.05 Hz to 100 Hz frequency range during the Prohesion exposure, which are indicative of the barrier properties provided by the surface coating, in this case, by the polyurethane clear topcoat, since the Mg-rich primer usually contributes to cathodic protection and shows a lower impedance, $< 10^6\,\Omega$ [20,21].

Barrier property is a major characteristic of corrosion protective coatings. Barrier property of a coating can be gauged by the resistance of the coating to the passage of electric current. For this reason, the low-frequency modulus value has been widely used as an estimate of coating's barrier properties [27,28]. In this study, the |Z| value associated with the frequency of 0.05 Hz was used as an estimate of the barrier property of the coating. The $|Z|_{0.05\,Hz}$ values for both the Prohesion dry and wet steps as a function of exposure time are shown in Figure 5. It was found that both $|Z|_{0.05\,Hz}$ values for dry and wet steps had similar profiles for the first 10 days, indicative of rapid decrease of the modulus from about $1 \times 10^9\,\Omega$ to $1 \times 10^8\,\Omega$. At the 10-day mark, the wet $|Z|_{0.05\,Hz}$ values dipped to around $1 \times 10^8\,\Omega$, followed by another rapid decrease to $4 \times 10^6\,\Omega$ during the 20–40 day period. After about 40 days, the $|Z|_{0.05\,Hz}$ values stabilized around $3 \times 10^6\,\Omega$ for the duration of the testing. The dry $|Z|_{0.05\,Hz}$ values showed similar changes with about $1 \times 10^7\,\Omega$ during the first 10-20 days, followed by a rapid drop to $1 \times 10^6\,\Omega$ by day 40 and no further change for the remainder the test. It was clearly observed that the barrier properties of the coatings were weakened step by step during the 60 days' Prohesion chamber exposure. Another finding was the wet $|Z|_{0.05\,Hz}$ values being relatively higher than the dry ones, that may due to the higher average temperature in the dry step (Figure 2) and the fact that the polyurethane topcoat is more sensitive to higher temperature due to its porosity.

The capacitance values C_c, calculated from the impedance data at the frequency of 9998.2 Hz, were plotted as a function of time in Prohesion chamber (Figure 6). The trends in the C_c values were similar for the dry and wet conditions, increasing from 0.1 to 0.2 nF for the first 20 days, then quickly increasing from 0.2 to 0.7 nF for another 20 days, reaching over 1 nF after day 50.

8

These results indicated that barrier properties of the coating during the Prohesion exposure decreased slowly in the beginning, then weakened quickly after 20 days. This change pattern was found to be consistent with the EIS Bode plots and $|Z|_{0.05\ Hz}$ values. All the results showed that the coatings started to degrade from the beginning of the Prohesion exposure and failed to provide to barrier properties after about 40 days of Prohesion exposure.

3.2.2. Sensor-sensor EIS

In addition to the two-electrode (2E) sensor-substrate EIS method, sensor-sensor EIS measurement (Figure 1) was used for in-situ monitoring of the coating system changes during the Prohesion exposure. Theoretically, $|Z|$ values from the sensor-sensor EIS measurement should be the complex of the two $|Z|$ values from individual sensors, so the EIS data from the sensor-sensor configuration should be very similar to those acquired with the sensor-substrate EIS setup.

Sensor-sensor EIS measurements for the frequency range of 100 kHz to 0.05 Hz were performed after 40 minutes into the drying and wetting steps,. The first testing day was day 14 of Prohesion exposure and final day of 2E sensor-sensor EIS testing was day 60. The EIS Bode plots for the Prohesion dry steps are shown in Figure 10 as a function of exposure time. It was observed that the impedance response had slight changes from day 14 to day 21, and the low-frequency impedance on day 30 was around $1\times10^7\,\Omega$. The $|Z|$ value for days 43, 52 and 60 were almost superimposed throughout the entire frequency range, and the low frequency modulus values were down to about $1\times10^6\,\Omega$. The phase angles prior to day 30 were close to -80° in the high frequency range, which was indicative of coatings performing like a capacitor. Phase angles after day 43 were about -60° in the 100 Hz to 100 kHz high-frequency range. All the phase angles were around -30° in the 0.05 Hz to 1 Hz range, indicating the barrier properties of coatings were decreasing. The EIS Bode plots during the Prohesion wet steps had the very similar profiles.

Figure 8 shows the changes of low frequency modulus $|Z|_{0.05\ Hz}$ values as the function of Prohesion exposure time. Both $|Z|_{0.05\ Hz}$ values of dry and wet steps had similar change patterns, involving gradual decrease from about 1×10^8 to $8\times10^6\,\Omega$ for the wet step and from 2×10^7 to $1\times10^6\,\Omega$ for the dry step between days 14 and 43, followed by no changes in the modulus values up until the end of testing on day 60. It is apparent that the coatings were failing and losing barrier properties during Prohesion exposure. It was also found that the $|Z|_{0.05\ Hz}$ values of wet steps were higher than those of dry steps. This result is consistent with the findings of the sensor-substrate EIS.

9

The capacitance values C_c were plotted as a function of Prohesion exposure time (Figure 9). C_c values both from dry and wet steps were increasing with time from about 0.2 nF to over 1 nF, indicating that the coatings were more susceptible to absorbing moisture and losing barrier properties.

3.2.3. Single Frequency Capacitance

As mentioned before, the increasing capacitance of a coating means the increasing of the dielectric property and more accessible to water uptaking of a coating. The classic Brasher-Kingsbury equation [29] can be used to quantitatively calculate the volume percentage of absorbed water (< 5%) in a coating film. A large coating capacitance value always represents more chance for water to get into the film. In this study, the evolution of the impedance of the coating at 9998.2 Hz on different Prohesion exposure days was measured during 3 dry and wet cycles, for a total of 6 hours. Capacitance values at 9998.2 Hz, $C_{9998.2Hz}$. were calculated from the impedance data and are shown in Figure 10. The $C_{9998.2Hz}$ evolution pattern varied with the Prohesion chamber conditions: capacitance values fluctuated in the dry step and remained relatively unchanged in the wet step. This was most likely due to the specific polyurethane clear topcoat being very sensitive to the temperature changes in the Prohesion chamber dry step. The dry step temperature increased from 25°C to 45°C for the first 20 minutes, then remained constant for the most part of the test and slightly decreased to about 40°C at the end of the dry step. In the dry step, topcoat was softened and thus more accessible to moisture penetration with the increasing temperature, while providing better barrier to electrolyte when the temperature decreased. In the wet step that follows the dry step, on the one hand, the temperature continues to decrease from 40°C to 25°C, but on the other hand, the fog fills up the entire chamber. This combination of decreasing temperature and the wetting atmosphere in the chamber keep the capacitance of the coating relatively constant. As expected, the capacitance levels were increasing with longer exposure times. The $C_{9998.2Hz}$ values for day 16 were in the 0.25-0.35 nF range, while the $C_{9998.2Hz}$ values from day 51 fluctuated much more, between 1.0 and 1.5 nF. Clearly, the longer the exposure in Prohesion chamber, the higher and more fluctuated the values of $C_{9998.2Hz}$ were, indicating that the coating's barrier properties were deteriorated during Prohesion exposure.

10

3.3. ENM Results

Electrochemical noise measurements were conducted while the coated panels were exposed in the Prohesion chamber. Both the electrochemical potential and current noise records were collected. The ENM monitoring was carried out continuously for more than 6 hours, which covered three dry-wet Prohesion cycles.

The original ENM raw data are not reported here directly, due to the overwhelming amount of date points. Instead, the noise resistance (R_n) value is discussed. R_n was obtained by dividing the standard deviation of the potential noise by the standard deviation of the current noise. In fact, the original potential and current raw noise data were divided into many small blocks, each containing 128 data points, which is equivalent to 25.6 seconds of testing period. Linear detrending was also applied to the original noise data of each block to remove the electrochemical drift, and then noise resistance was calculated [30]. Therefore, the R_n values reported here are, in fact, averages over 128 data points (25.6 seconds).

It has been reported elsewhere that R_n is quantitatively close to the coating polarization resistance R_p and the low frequency impedance modulus, and thus can serve as a good indicator of the barrier properties and lifetime prediction of coating performance [31-32]. The R_n values for three different days of Prohesion exposure are shown in Figure 11. For day 1, the R_n values were constant in the dry step and slightly scattered in the wet step, but all close to $1 \times 10^9 \, \Omega$, showing that the coating film acted as a good barrier at the early stage of Prohesion exposure. After 10 days, much more scattered values from 10^7 to $10^9 \, \Omega$ were observed for both the dry and wet steps, and the averaging R_n value was around $10^8 \, \Omega$, indicating that the coating still provided adequate barrier protection. However, there was no obvious difference in terms of magnitude and dispersibility of the R_n values in dry and wet steps. It means that once the coatings started to degrade, the water and electrolyte absorbed onto the coating surface could not be totally driven out during the dry step or that the coating had been softened in the dry step and rendered more accessible to moisture. The Rn values were only between 10^4 to $10^6 \, \Omega$ after 60 days of Prohesion exposure, indicating fairly low barrier properties afforded by the coating towards the end of the test, at which point the film could be easily wetted allowing the electrolyte to penetrate further into the primer and to the substrate/primer surface.

11

It was observed from Figure 10 that the R_n values varied significantly between the first day and the last days of data acquisition. In order to better illustrate the evolution of the noise resistance of the coating system, R_n values from both dry and wet steps were plotted as a function of Prohesion exposure time, as shown in Figure 12. Here, the R_n values are average noise resistance values from 30 to 45 minutes into either dry or wet steps.

The R_n started from very high values, $1 \times 10^9 \, \Omega$, then quickly dropped to $1 \times 10^7 \, \Omega$ after about 10 days and maintained that value for another two weeks, followed by another quick drop to 1×10^6 Ω after about 6 weeks of Prohesion exposure, and eventually leveled off for the rest of the test. This R_n value profile was highly consistent with the evolution of the low-frequency impedance modulus from EIS, indicating that both EIS and ENM techniques when combined with sensors can detect the coating changes during the entire Prohesion exposure were found in good correlation with each other.

4. Conclusion

The Mg-rich primer and polyurethane clear topcoat system was applied onto AA2024-T3 substrates, and platinum sensors were embedded between the primer and the topcoat. Then the coated substrates were put into the standardized Prohesion chamber to simulate weathering conditions in an aggressive manner to induce accelerated coating failure. The acquisition of EIS and ENM data from embedded sensor in-situ monitoring during the Prohesion dry and wet steps provided insight into the coating behavior evolution. It was found that both EIS and ENM in-situ monitoring could be conducted with embedded sensors under both dry and wet Prohesion steps. Under the dry Prohesion step, the coatings were sensitive to the temperature changes, while in the wet step, the resistance values were more scattered due to the moisture accumulation on the coating surface. The effects of both the temperature and humidity variation on changes in coating propertiess were in-situ monitored by the embedded sensors in Prohesion chamber. It was found that the coating degraded continuously with Prohesion exposure time as evidenced by the gradual decrease of both low frequency impedance $|Z|_{0.05 \, Hz}$ and noise resistance R_n.

12

References:

1. Z. W. Wicks, F. N. Jones and S. P. Pappas. *Organic Coatings Science and Technology*, Second Edition. **1998**, 129-140.

2. G. P. Bierwagen, *Progress in Organic Coatings,* **1996,** 28, 43..

3. Ray Mudd, *Journal of Protective Coatings & Linings,* October **1995,** 51.

4. G. Gardner, "ASTM's New Coating Test Method Addresses Interactive Effects of Weathering and Corrosion," *Journal of Protective Coatings & Linings,* September **1998,** 50.

5. G. Gardner, "Recently Developed ASTM Test Addresses Interactive Effects of Weathering and Corrosion," *Protective Coatings Europe,* February, **1999**, 86.

6. Van Leeuwen, *Protective Coatings Europe*, January, **1996**, 42.

7. C. Simpson and R. C. D. Hicks, "ASTM D5894 and the Development of Corrosion Resistant Coatings," *Paint & Coatings Industry*, May, **1997**, 76.

8. N. D. Cremer, *Polymers Paint Colour Journal*, **1998**, 188, 31.

9. S. L. Chong, *Journal of Protective Coatings & Linings,* March, **1997**, 20.

10. B. S. Skerry and D. A. Eden, *Progress in Organic Coatings*, **1987**, 15, 269.

11. C. H. Tsai and F. Mansfeld, "Determination of Coating Deterioration with EIS. Part II. Development of a Method for Field Testing of Protective Coatings," *Corrosion*, **1993**, 49, 726.

12. F. M. Greenen, J. H. W. DeWit and E. P. M. Van Westing, *Progress in Organic Coatings*, **1990**, 18, 299.

13. D. Loveday, P. Peterson and B. Rogers-Gamry Instruments "Evaluation of organic coatings with Electrochemical Impedance Spectroscopy, part 2: Applications of EIS to coatings" *J. Coat. Technol.*, October, **2004**, 88.

14. D. A. Eden, M. Hoffman and B. S. Skerry, Application of electrochemical noise measurements to coated systems, in: R.A. Dicke, F.L. Floyd (Eds.), Polymeric Materials for Corrosion Control, ACS Symposium Series 322, American Chemical Society, Washington, DC **1986**.

15. M. Selvaraj and S. Guruviah, *Progress in Organic Coatings*, **1996**, 28, 271.

16. G. P. Bierwagen, X. Wang and D. E. Tallman, "In-situ Study of Coatings Using Embedded Electrodes for ENM Measurements", *Progress in Organic Coatings*, **2003**, 46, 163.

13

17. K. Allahar, Quan, Su, G. P.Bierwagen, D. Battocchi, V. J. Gelling and D. Tallman, "Future Studies of Embedded Electrodes for In-situ Measurement of Corrosion Protective Properties of Organic Coatings," NACE Corrosion/2006 Conference, March **2006**, San Diego CA.

18. K. Allahar, Quan, Su, G. P. Bierwagen, D. Battocchi, V. J. Gelling and D. Tallman, "Examination of the Feasibility of the Use of In-situ Corrosion Sensors in Army Vehicles", **2005** Tri-service Corrosion Conference, Orlando, FL.

19. K. Allahar, Quan, Su, G. P. Bierwagen, "Monitoring of the AC-DC-AC Degradation of Organic Coatings by Embedded Sensors", NACE Corrosion **2007** Conference, Nashville, TN.

20. M. Nanna and G. P. Bierwagen. *Journal of Coatings Technology*, April, **2004**, 1, 52.

21. D. Battocchi and G. P. Bierwagen. *Corrosion Science*, **2006**, 48, 1292.

22. D. Battocchi and G. P. Bierwagen. *Corrosion Science*, **2006**, 48, 2226.

23. X. Wang, "Study on novel electrode configurations for in situ corrosion monitoring on coated metal systems", Ph.D. Thesis, Chapter 3, Faculty of Science and Mathematics, North Dakota State University, **2002.**

24. S. Mabbutt, D.J. Mills, Surf. Coat. Int. Part B: *Coat. Trans.*, **2001**, 84, 277

25. R. A. Cottis, *Corrosion*, **2001**, 57, 265

26. H. A .A. Al-Mazeedi and R. A. Cottis, *Electrochim. Acta*, **2004**, 49, 2787

27. H. K. Yasuda, C. M. Reddy, Q. S. Yu, J. E. Deffeyes, G. P. Bierwagen and L. He, *Corrosion*, **2001**, 57, 29

28. J. N. Murray, *Progress in Organic Coatings*, **1997**, 31, 375

29. D. M. Brasher and A. H. Kingsbury, *Journal of Applied Chemistry*, **1954**, 4, 62.

30. R. A. Cottis, *Corrosion*, **2001**, 57, 265.

31. D. J. Mills and S. Mabbutt, *Progress in Organic Coatings*, **2000**, 39, 41.

32. G. P. Bierwagen, C. S. Jeffcoate, J. Li, S. Balbyshev, D. E. Tallman and D.J. Mills, *Progress in Organic Coatings*, **1996**, 29, 21.
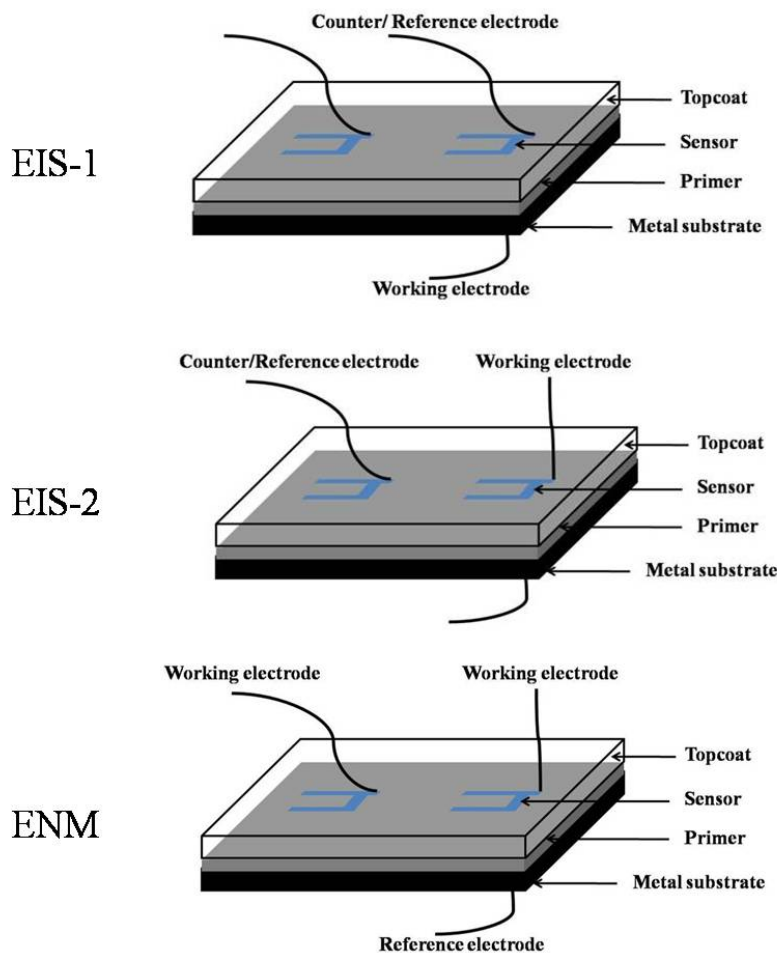
14

Figure 1. Schematic diagram of the electrochemical experimental setup. EIS-1: Sensor-substrate EIS, where the embedded sensor is the reference/counter electrode and the substrate is the working electrode. EIS-2: Sensor-sensor EIS, where one embedded sensor serves as the reference/counter electrode and the other as the working electrode. ENM: where the embedded sensors serve as working electrodes and the substrate is the reference electrode.
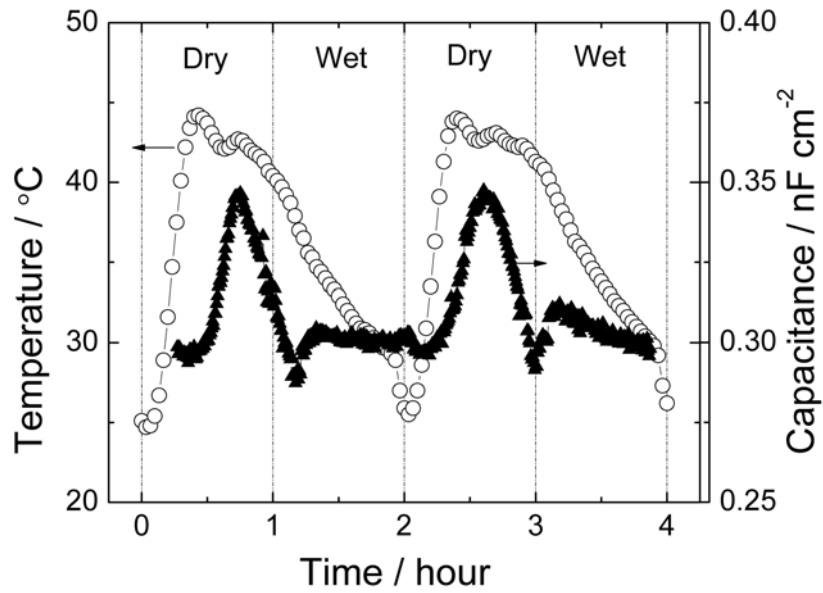
Figure 2. The temperature profile at the surface of the coated panel and the calculated capacitance during the dry and wet steps of Prohesion conditions. Dashed lined are used to identify the steps.
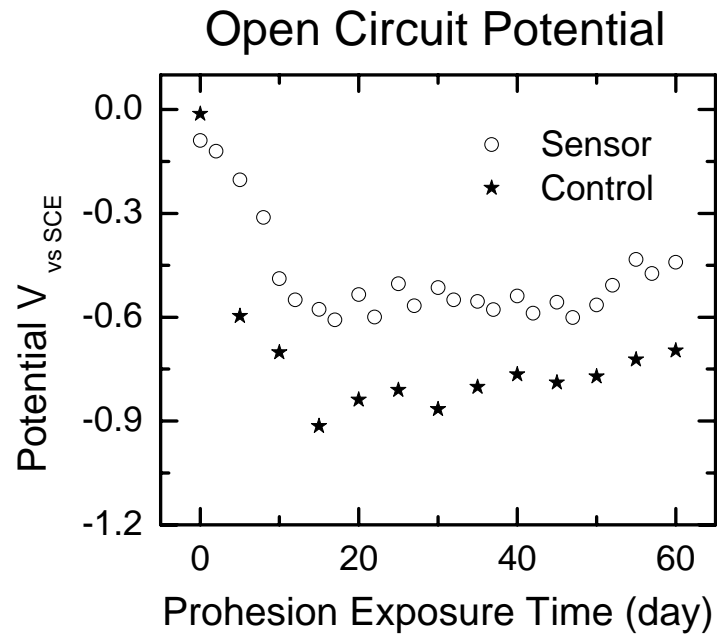
Figure 3. OCP monitoring in-situ (sensor) and ex-situ (control, 3E setup).
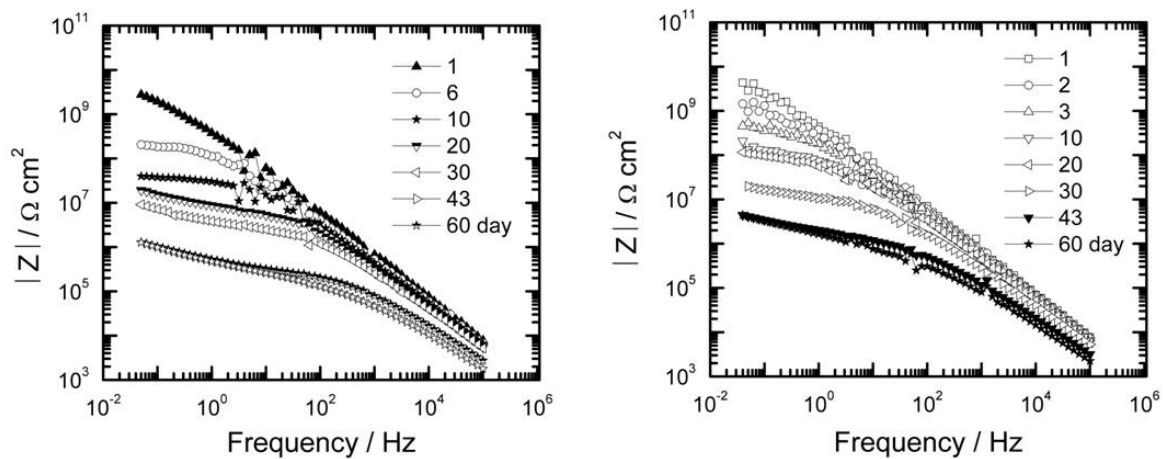
Figure 4. Impedance of sensor-substrate EIS data during the Prohesion dry steps (left) and wet steps (right).
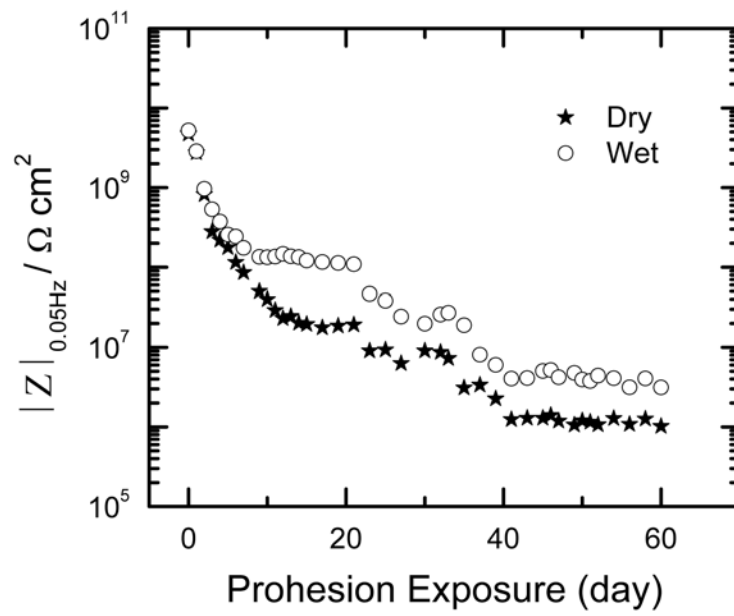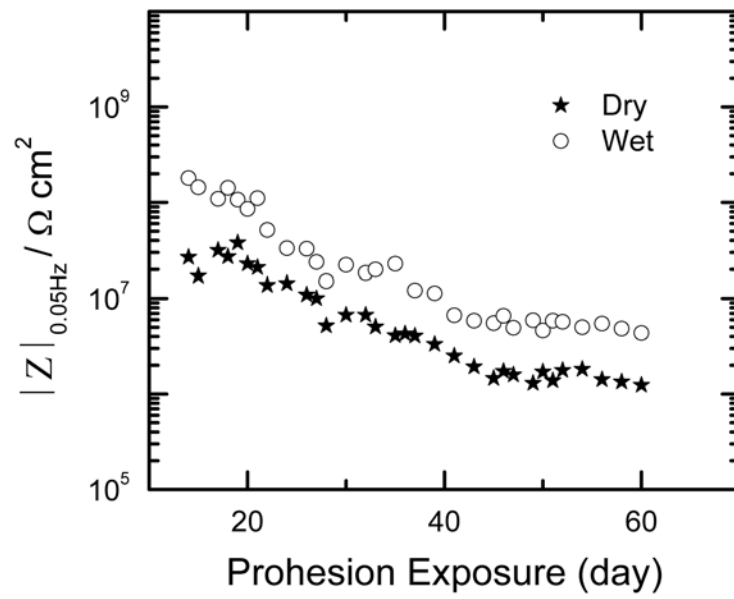
Figure 5. Evolution of the low-frequency impedance $|Z|_{0.05\ Hz}$ values of the 2E sensor-substrate EIS during dry and wet Prohesion steps as a function of time.
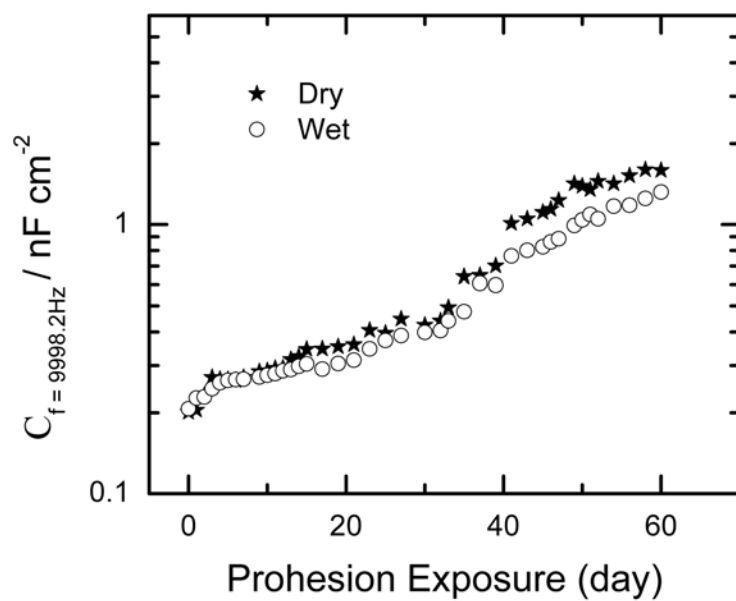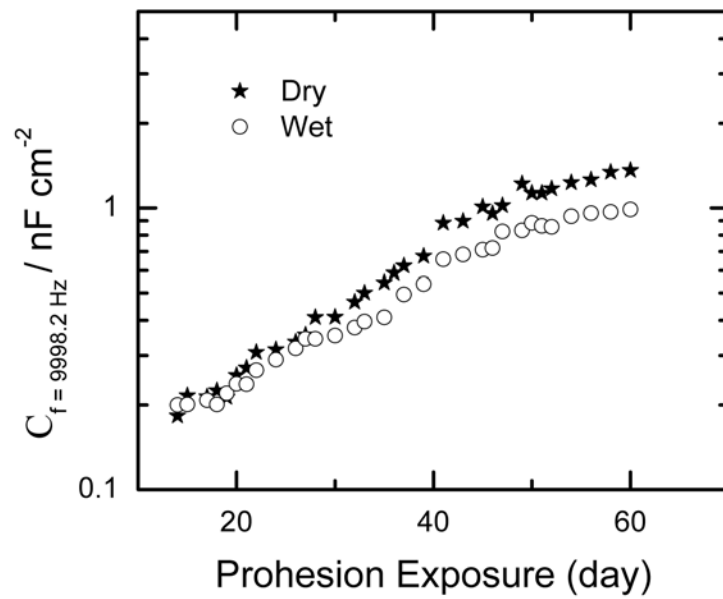
Figure 6. Evolution of the high-frequency capacitance, $C_{9998.2Hz}$, of 2E sensor-substrate EIS during the dry and wet steps of Prohesion as a function of time.
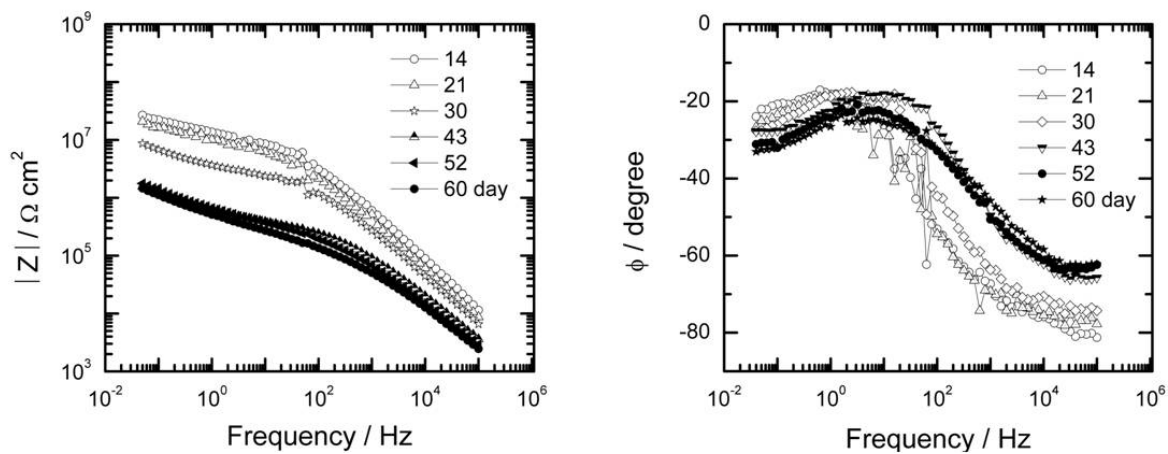
Figure 7. The EIS Bode plots of the coated panel under Prohesion dry step after 40 minutes of drying: (a) impedance modulus, (b) phase angle.

Figure 8. Evolution of the low-frequency impedance $|Z|_{0.05\ Hz}$ values of 2E sensor-sensor EIS during dry and wet Prohesion steps as a function of time.

Figure 9. The evolution of the high-frequency capacitance, $C_{9998.2Hz}$, of 2E sensor-sensor EIS during dry and wet Prohesion steps as a function of time.

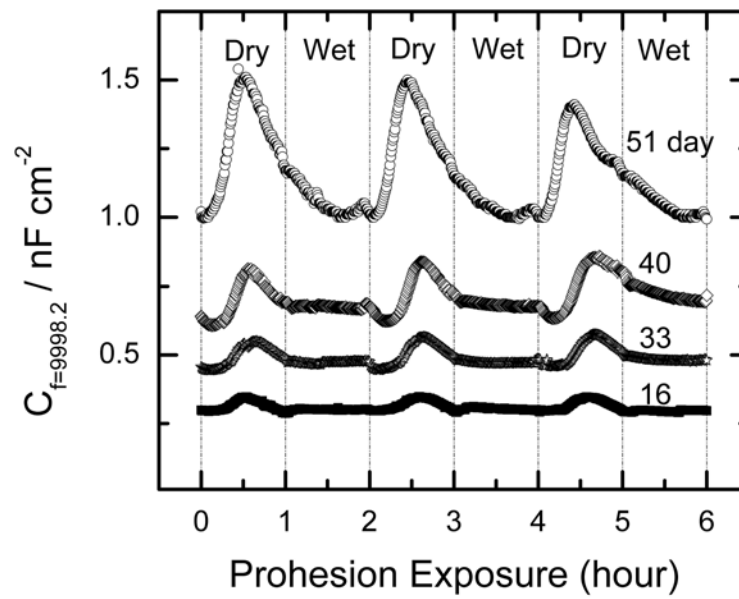Figure 10. The evolution of high-frequency capacitance, $C_{9998.2Hz,}$ during the dry and wet Prohesion steps as a function of time.
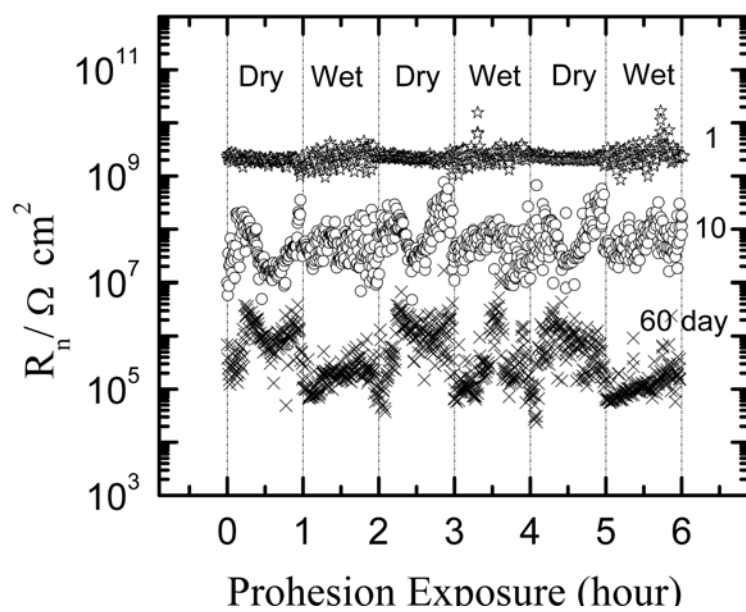
Figure 11. Changes of electrochemical noise (R_n) values during the Prohesion chamber 3 dry and wet cycles at three different exposure times.
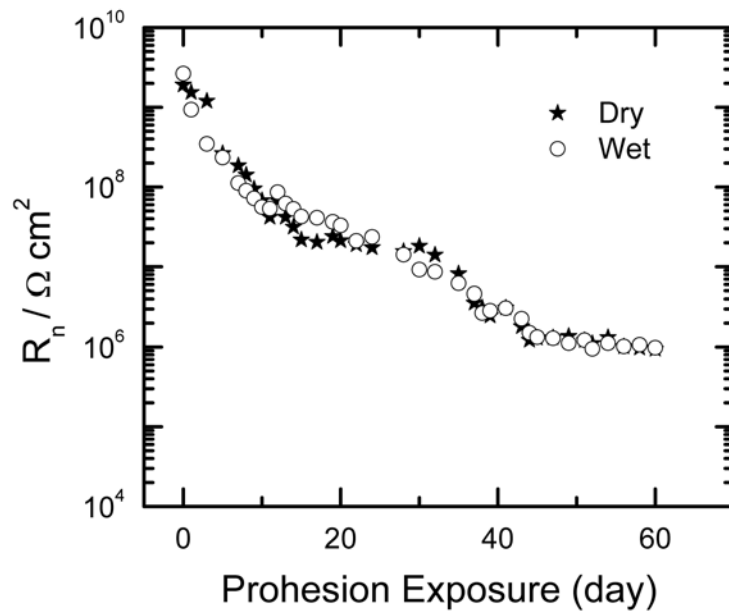
Figure 12. Evolution of the average R_n values obtained from the dry and wet Prohesion steps as a function of time.